Title

Exploring the tectonic and thermal evolution of the northern Snake Range metamorphic core complex, eastern Nevada: Insights from field studies and potassium feldspar 40Ar/39Ar thermochronology

Permalink

https://escholarship.org/uc/item/6t98m86k

Author

Wrobel, Alexander Joseph

Publication Date

2020

Supplemental Material

https://escholarship.org/uc/item/6t98m86k#supplemental

Peer reviewed|Thesis/dissertation

UNIVERSITY OF CALIFORNIA

Santa Barbara

EXPLORING THE TECTONIC AND THERMAL EVOLUTION OF THE

NORTHERN SNAKE RANGE METAMORPHIC CORE COMPLEX:

INSIGHTS FROM FIELD STUDY AND POTASSIUM FELDSPAR ^{40}Ar/^{39}Ar

THERMOCHRONOLOGY

A dissertation submitted in partial satisfaction of the

requirements for the degree

DOCTOR OF PHILOSOPHY

in Earth Science

BY

ALEXANDER JOSEPH WROBEL

Committee in charge:

Professor Phillip Gans, Chair

Professor Bradley Hacker

Professor Kristen Morell

December 2020

The dissertation of Alexander Joseph Wrobel is approved.

_____

Dr. Bradley Hacker

_____

Dr. Kristin Morell

_____

Dr. Phillip Gans, Committee Chair

September 2020

Exploring the tectonic and thermal evolution of the northern Snake Range metamorphic core

complex, eastern Nevada: Insights from field studies and potassium feldspar ^{40}Ar/^{39}Ar

thermochronology

ACKNOWLEDGMENTS

My success as a graduate student is owed to many people: academic mentors, family, friends, lab mates, and those providing financial support. First, I thank my advisor, Phil Gans. Thank you for supporting me in every aspect of my research – from endless hours of revision to encouragement and guidance in the field. Your infectious love of geology and unbound curiosity is truly inspiring, and I hope to maintain that same passion throughout my career.

Thank you to my friends and fellow graduate students. To my lab mates old and new, Mary Kate Fidler, Will Junkin, Jason Womer, Evan Monroe, and Justin Newmann, thank you for the many fruitful discussions and help along the way. To the Ravenscroft geology crew: Elisabeth Steel, Will Junkin, Mary Kate Fidler, Sophie Briggs, and Joshua Garber. You showed me how to tackle graduate school and have fun along the way. Thank you to Andrew Reinhard, Andrew McGrath, Eliel Antilla, Devin Rand, and Paul Allesio for the long sports debates and remarkable surfing adventures.

A very special thank you to Jason Womer. I am so fortunate to have started graduate school with a contemporary that shared my passion for geology and hijinks. Your comradery and spirit kept me sane during months of fieldwork, and I'm proud to call you my friend and colleague.

I also thank the UCSB Earth science faculty and staff. To Yann Ricard, Kate Lima, Jaima Ortega, Shannon Dalton, and Peter Green, thank you for answering all my questions and for putting out every fire I started. An enormous thank you to Tim Cuellar for helping me plan field trips and for the mid-day coffee gab sessions. Thank you to those who served on my committee: Brad Hacker, Kristin Morrell, and Doug Burbank. Your questions, feedback, and

Finally, I thank my family. This would not have been possible without your love, support, and sacrifice. To my sister, thank you for keeping me in check. To my mother, thank you for your patience, understanding, and motivation. To my father – you raised me to be curious about everything. Your lessons have served as the foundation for my academic pursuits. Lastly, to my Fiancé, thank you for making me smile every day.

VITA OF ALEXANDER JOSEPH WROBEL

SEPTEMBER 2020

EDUCATION

Bachelors of Arts with honors in Geology, Colgate University, May 2015 (Magna cum laude)

Doctor of Philosophy in Geologic Sciences, University of California Santa Barbara,

   September 2020 (expected)

PROFESSIONAL EMPLOYMENT

2020-   Adjunct Instructor, Department of Earth and Planetary Science, Santa Barbara City College

2018-2020   Associate Instructor, Department of Earth Science, University of California Santa Barbara

2019   Exploration Geologist, McEwen Mining Inc. (via Geotemps, Inc.)

2018   Adjunct Instructor, Department of Geology, Colgate University

2015-2018   Teaching Assistant, Department of Earth Science, University of California Santa Barbara

2012-2015   Undergraduate Researcher, Department of Geology, Colgate University

PUBLICATIONS

Wrobel, A. J., Gans, P.B., Womer, J. (*in prep*) Late Cretaceous crustal shortening in the

   northern Snake Range metamorphic core complex: Constraints on the structural

   geometry and magnitude of pre-extensional footwall burial.

Gans, P.B., **Wrobel, A.J.**, Wong, M.S. (*in prep)* Argon thermochronology of the Snake

   Range metamorphic core complex: implications for the geometry, timing, and rates of

   extensional exhumation of footwall rocks.

Wrobel, A.J., Gans, P.B., (2017) *Characterizing pre-Miocene structures within the northern*

Snake Range core complex: insights into the role of tectonic heredity in core complex development. GSA Cordilleran Section Abstracts. *Runner-up best graduate student presentation

Wrobel, A.J., Wong, M.S., and Singleton, J.S., 2014 *Evidence for Late Cretaceous–early Tertiary lower platemylonitization and extension in the Harcuvar metamorphic core complex, Arizona: Evidence from U-Pb geochronology.* American Geophysical Union Abstracts

ACADEMIC HONORS

National Science Foundation Graduate Research Fellowship (NSF GRFP)	2017-2020
Geological Society of America Outstanding Graduate Student Poster Runner-up	2017
G.K. Gilbert Award for best oral research presentation at dept. seminar (UCSB)	2019
L. and M. Edwards Field Studies Fellowship	2019
Geological Society of America Graduate Student Research Grant	2016
The Richard and Eleanor Migues Award for field geology	2018
Muckers' Coterie (UCSB undergrad club) TA of the year	2017
Global Field Travel Award-UCSB	2016, 2017
Robert Linsley Award for Excellence in Geology	2014
Undergraduate Summer Research Fellow	2012, 2013, 2014
Dean's Award for Academic Excellence	2011 - 2015
Clark Foundation Scholarship	2011 - 2015

ABSTRACT

Exploring the tectonic and thermal evolution of the northern Snake Range metamorphic core complex, eastern Nevada: Insights from field studies and potassium feldspar ^{40}Ar/^{39}Ar thermochronology

by

Alexander Joseph Wrobel

Metamorphic core complexes of the North American Cordillera record episodes of Mesozoic burial followed by high magnitude crustal extension. This dissertation combines field investigation and potassium feldspar ^{40}Ar/^{39}Ar thermal modeling at a classic cordilleran metamorphic core complex, the northern Snake Range MCC, to understand a) the structures and fabrics associated with Mesozoic shortening, burial, and deep-seated metamorphism of footwall units, and b) the exhumational/cooling history deeply buried footwall rocks.

Chapter 1 presents geologic mapping and cross sections of km-scale late Cretaceous fold and thrust relationships of the Northern Snake Range Fold and Thrust System exposed in the footwall of the northern Snake Range metamorphic core complex. Specifically, we describe the O'Neil Peak Recumbent Syncline and its overlying anticlinal closure, the O'Neill Peak Anticline (OPA), that effectively double the structural thickness of middle-upper Cambrian lower plate strata from ~3.5 km to ~8km. West of the O'Neil Peak Recumbent Syncline,

pervasive isoclinal folding in lower Cambrian schistose units and local thrust duplication of lower and middle Cambrian units of the Eightmile Thrust System reflect significant layer parallel shear and shortening in stratigraphically deeper units. Crosscutting intrusive relationships and synmetamorphic tectonite fabrics indicate the O'Neil Peak Recumbent Syncline and Eightmile Thrust System are broadly coeval with Late Cretaceous prograde metamorphism of footwall units. Detailed cross sections are used to create an interpretive pre-extensional reconstruction of the Northern Snake Range that integrates the Northern Snake Range Fold and Thrust System with associated supracrustal shortening structures now exposed in the Confusion Range to the east. We conclude that the Northern Snake Range Fold and Thrust System and overlying structures accommodated ≥10km of horizontal shortening, resulting in ≥ 7 km of structural burial of the deepest structural levels in the NSR footwall. The structural burial estimate from our reconstruction satisfies the minimum burial depth proposed by thermobarometric studies of lower plate metamorphic units at the northern Snake Range metamorphic core complex.

Chapter 2 employs multiple-diffusion domain (MDD) modeling of a large (n=28) geologically well-constrained K-feldspar ^{40}Ar/^{39}Ar thermochronology dataset from the Northern Snake Range and surrounding environs to provide new insights into MDD parameter space and test the reliability of MDD model cooling histories. Here, we describe the variability of kinematic and domain parameters across the dataset, provide a set of best-practices from optimizing the internal consistency of MDD model cooling histories, and propose a schema for extracting geologically reasonable T-t paths directly from a sample's experimental age spectrum. Diffusion domain size distributions within a single sample typically span 4-5 orders of magnitude, and the distribution of Ar among domains is related

to a sample's original grain-size. All K-feldspar samples require ≥8 diffusion domains to adequately model experimental results. Activation energies (E_a) of Ar diffusion in K-feldspar range from 42-54 kcal/mol with a mean (±1σ) of 48.4 ± 1.6 kcal/mol. The MDD cooling history dataset is more internally consistent if all cooling histories are calculated using an E_a that falls within ±1σ of the mean E_a of the data set, suggesting that much of the observed variation in E_a is likely due to analytical error and not natural variation. We use these results to construct an internally consistent dataset of MDD cooling histories, and use these cooling histories to explore quantitative relationships between the shape of an age spectrum and its MDD cooling history. We find quantifiable correlations between a) the slope of an age spectrum and the MDD model cooling rate, b) the initial slope of an age spectrum and the minimum MDD model cooling temperature recorded by that sample, and c) the cumulative fraction of ^{39}Ar released during a step heating experiment and the effective MDD model geologic cooling temperature of the sample – a curve we term the temperature spectrum. These relationships between the age spectrum and MDD model cooling history are sufficiently systematic and quantifiable that we develop a schema for extracting T-t histories directly from K-Feldspar age spectra.

TABLE OF CONTENTS

LIST OF FIGURES

CHAPTER 2

LIST OF TABLES

INTRODUCTION

The North American Cordillera records episodes of major Mesozoic back-arc crustal shortening and thickening followed by equally impressive crustal extension and thinning during the Cenozoic. Nowhere is this complex polyphase tectonic evolution better expressed than in the metamorphic core complexes (MCC) of the cordillera. The goal of this dissertation is to decipher the late Mesozoic and Cenozoic tectonic and thermal history of a classic cordilleran metamorphic core complex, the northern Snake Range MCC, focusing on both the earlier, previously poorly documented Mesozoic burial and metamorphic history, and the subsequent Cenozoic extensional and cooling history. This dissertation is split into two distinct chapters: the first is largely a field-based study that explores the structures and fabrics associated with Mesozoic shortening, burial, and deep-seated metamorphism in the range, and the second uses a previously acquired extensive $^{40}Ar/^{39}Ar$ database from the northern Snake Range to, a) explore the theory, methodology, application, and limitations of potassium feldspar $^{40}Ar/^{39}Ar$ thermochronology, and b) develop a new schema for interpreting the temperature-time histories directly from potassium feldspar $^{40}Ar/^{39}Ar$ age spectra. This second chapter provides the intellectual framework and strategies for a forthcoming companion paper in collaboration with my advisor Phillip Gans that will reconstruct the thermal and tectonic evolution of east-central Nevada from the Mesozoic to the Cenozoic.

Chapter 1 is the culmination of a three-year mapping project documenting Late Cretaceous fold and thrust relationships in the northern Snake Range, here collectively term the Northern Snake Range fold and thrust system (NSRFTS). Thermobarometric studies from many cordilleran core complexes, including the northern Snake Range, indicate that footwall units

were commonly buried to 20-30 km (2-3x their original stratigraphic depth) within the Sevier Hinterland during the late Cretaceous. However, few studies have identified the necessary structures responsible for such deep burial. My identification and geometric description of the NSRFTS, including map-scale to mesoscopic structural analysis paired with new U/Pb geochronology of intrusive phases that bracket the age of these structures, provide a plausible pre-extensional palinspastic reconstruction of the northern Snake Range – perhaps the best example to date of precisely how the footwall of an MCC was buried to middle to lower crustal levels during the Mesozoic. Mapping and field study was conducted for a total of nine months, spanning 3 field seasons, supplemented by the existing geologic mapping and geochronology of Womer (2017) and Lee et al., (1999; 2017). A critical contribution to the success of this study was my considerable effort towards dividing the well-studied Paleozoic shelf sequence into sub-members to increase the map resolution and allow for detailed geometric descriptions of structures. A fence diagram comprised of 22 cross-sections provides an interactive 3-D model of the modern fold/thrust exposures and emphasizes its highly non-cylindrical nature. New U/Pb geochronology of intrusive phases and descriptions of metamorphic fabrics place relative age constraints on the structures and confirm that the burial structures are broadly coeval with regional metamorphism. I use these observations to create a pre-extensional reconstruction of the NSRFTS to assess the magnitude of Mesozoic shortening and structural burial at the modern northern Snake Range. This reconstruction of the pre-extension NSRFTS is then integrated with potential overlying shortening structures of the Western Utah fold and thrust belt (Greene, 2014) to create a plausible reconstruction of the Sevier Hinterland in eastern Nevada spanning the upper-mid crust.

Chapter 2 delves deeply into the methodology and applications of potassium feldspar ^{40}Ar/^{39}Ar thermochronology and develops new methods for extracting reliable thermal histories from potassium feldspar ^{40}Ar/^{39}Ar age spectra. The ultimate goal of this work, in collaboration with Dr. Phillip Gans, is to use K-feldspar ^{40}Ar/^{39}Ar thermal histories, combined with various other thermochronometers, to unravel the Cenozoic cooling and unroofing history of the northern Snake Range metamorphic core complex. However, to accomplish this requires a robust and reliable methodology for extracting consistent thermal histories from a large K-feldspar ^{40}Ar/^{39}Ar geochronology dataset. My contribution, and the focus of chapter 2, is to explore the theoretical foundation of K-feldspar ^{40}Ar/^{39}Ar thermal modeling, identify limitations of the method, and discuss a set of best practices to optimize the consistency of MDD temperature-time histories across a large dataset. I discuss the leading theory of Argon diffusion/retention in K-feldspar, the multiple diffusion domain (MDD) theory, and how this theory is used to create a continuous geologic cooling history for a sample between ~160 and ~350 C. I then undertake the lengthy process of producing MDD cooling histories from an existing large, high-spatial density data set (n=28) from the northern Snake Range and surrounding environs to test the limitations and reproducibility of MDD model cooling histories. From these results, I present a method for optimizing the consistency of model results across a dataset, thus ensuring that meaningful regional cooling trends and tectonic interpretations can be distilled from the results. With this regionally consistent MDD data set, I then ask: are there quantitative relationships between the shape of the experimental Kspar ^{40}Ar/^{39}Ar age spectrum and its corresponding MDD model cooling history? If yes, is it possible to construct an approximate cooling history directly from the experimental results, bypassing the lengthy process of calculating MDD model cooling

3

history? We test these questions and present a schema for extracting an approximate T-t history directly from an experimental age spectrum without the need for time-consuming MDD modeling. Ultimately, these new MDD results, together with the new analytical tools for interpreting K-feldspar ^{40}Ar/^{39}Ar age spectra, will be employed in a companion paper (Gans et al., in prep) to explore the regional thermal/exhumational history of the northern Snake Range MCC.

Though these chapters employ very different methods to achieve very different ends, they are mutually reinforcing in that they serve to understand the tectonic evolution of the northern Snake Range metamorphic core complex. Together, they explore both the Late Cretaceous burial history and the Cenozoic cooling/exhumational history of a classic cordilleran metamorphic core complex and thus contribute to our evolving knowledge of cordilleran tectonics.

CHAPTER 1

LATE CRETACEOUS CRUSTAL SHORTENING IN THE NORTHERN SNAKE RANGE METAMORPHIC CORE COMPLEX, EASTERN NEVADA: CONSTRAINTS ON THE STRUCTURAL GEOMETRY AND MAGNITUDE OF PRE-EXTENSIONAL FOOTWALL BURIAL

A. J. Wrobel[1], P.B. Gans[1], and J. B. Womer[1]

[1] University of California, Santa Barbara.

ABSTRACT

Detailed geologic mapping and structural investigation of the footwall of the northern Snake Range (NSR) metamorphic core complex, eastern Nevada reveal km-scale Late Cretaceous fold and thrust relationships of the Northern Snake Range Fold and Thrust System (NSRFTS) that are broadly coeval with the deep burial and amphibolite facies metamorphism of Eocambrian strata. The O'Neill Peak Recumbent Syncline (OPRS) – a NNW-trending, non-cylindrical, eastward-opening, inclined to recumbent syncline – and its overlying anticlinal closure, the O'Neill Peak Anticline, affect the entire Middle to Upper Cambrian stratigraphy, effectively doubling its structural thickness from ~3.5 km to ~8km. West of the OPRS, pervasive isoclinal folding in lower Cambrian schistose units and local thrust duplication of lower and middle Cambrian units of the Eightmile Thrust System record layer parallel shear and shortening. Detailed cross sections are used to create an interpretive pre-extensional reconstruction of the NSR that integrates the NSRFTS with associated supracrustal shortening structures now exposed in the Confusion Range to the east. We conclude that the NSRFTS and overlying structures accommodated ≥10km of horizontal

shortening, resulting in ≥ 7 km of structural burial of the deepest structural levels in the NSR footwall, thus explaining the localized kyanite-grade metamorphism and elevated thermobarometric P-T estimates. This burial was apparently quite localized as evidenced by decreasing metamorphism to the north and south. The highest magnitude of subsequent extensional exhumation of the NSR footwall coincides with the area of deepest burial, suggesting that Mesozoic crustal thickening influenced both the magnitudes and geometry of subsequent Cenozoic extensional exhumation.

1. INTRODUCTION

Cordilleran metamorphic core complexes (MCCs) of the Basin and Range Province are locations of high-magnitude extension recognized by the striking juxtaposition of strained mid-crustal metamorphic rocks and highly-faulted supracrustal rocks along a gently-dipping extensional detachment fault (Coney, 1980). Though widely studied as natural laboratories for crustal extension processes, many, if not most, Cordilleran MCCs preserve an earlier history of Mesozoic crustal shortening and thickening that pre-dates extension (Armstrong, 1982; Coney and Harms, 1984; Spencer and Reynolds, 1990; Wells et al., 2012). Metasedimentary rocks exposed in MCC footwalls previously resided at shallow (7-12 km) crustal levels, and, based on P-T estimates underwent localized Mesozoic burial to 2-3 times their original stratigraphic depth (Anderson et al., 1988; Lewis et al., 1999; McGrew et al., 2000; Cooper et al, 2010; Wells et al., 2012), in sharp contrast to neighboring equivalent units that remained in the upper crust. This episode of contraction and burial of MCC footwalls is poorly understood with few constraints on a) the geometry and location of structures responsible for burial, b) the relationship of the local structures to the broader

tectonic framework of Mesozoic contraction, and c) their potential influence on the location and geometry of subsequent extensional unroofing.

Several factors limit the ability to study pre-extensional shortening histories of MCC footwalls. The MCCs of Arizona and the lower Colorado River Extensional Corridor (e.g. Whipple-Buckskin-Harcuvar Mountains MCCs) expose primarily crystalline basement rocks in their footwalls, devoid of stratigraphy, making it difficult to accurately characterize map-scale shortening structures (i.e., folds and thrust faults). Moreover, these crystalline rocks typically lack the mineral assemblages suitable for thermobarometric assessment of burial. Other core complexes (e.g., Albion-Raft River-Grouse Creek and Ruby Mountains MCCs) poorly preserve upper plate rocks and have highly uncertain structural relationships to adjacent mountain ranges, thereby limiting the assessment of shortening histories at shallow crustal levels. Additionally, most MCC footwalls are extensively overprinted by pervasive younger mylonitic fabrics and granitic intrusions that may largely transpose and obscure pre-extensional structures.

These limitations are not as severe in the northern Snake Range (NSR) metamorphic core complex of east-central Nevada (Figure 1), thus offering an opportunity to better characterize the Mesozoic shortening history of an MCC. The footwall is composed predominantly of metasedimentary units of the well-studied Eocambrian to upper-Cambrian miogeoclinal succession (Miller et al, 1983; Gans et al., (1999a,b); Lee et al., (1999a,b,c); Miller et al., (1999a,b). Pelitic units within the metasedimentary stratigraphy host mineral assemblages well-suited for thermobarometry, and P-T results can be directly compared to burial estimates derived from structural observations. The metamorphosed lower plate rocks can be directly correlated with unmetamorphosed/unstrained equivalent units in adjacent ranges,

allowing for assessment of unit thinning/thickening during burial and exhumation and providing an opportunity to more accurately reconstruct the pre-extensional architecture of the region (Hose and Blake, 1976, Gans et al, 1985). Finally, mylonitic fabrics associated with extensional unroofing in the NSR (Miller et al., 1983) die out in the west-northwest portion of the range (Lee et al., 1999a) and the original geometries of pre-extensional shortening structures and fabrics are reasonably well-preserved.

This study presents new detailed mapping (Plate 1) and structural data that characterize footwall structures and stratigraphy where extensional overprinting is weakest. Mapping presented in plate 1 and figure 4 is a compilation of 1:5000-scale mapping by Womer (2017, unpublished MS thesis) and Wrobel (2020, this study) supplemented with existing 1:24,000 maps by Lee et al. (1999a). This new geologic mapping database is used to produce well-constrained cross sections that illustrate the geometry and style of pre-extensional folds and thrust faults associated with crustal shortening and thickening. Specifically, we describe in detail a map-scale east-vergent, inclined-to-recumbent syncline-anticline pair, termed the O'Neill Peak Recumbent Syncline (OPRS) and O'Neill Peak Anticline (OPA), and an east-directed thrust system, termed the Eightmile Thrust System (ETS). Collectively, we term these structures the Northern Snake Range Fold and Thrust System (NSRFTS). Descriptions of synkinematic tectonite fabrics elucidate strain/metamorphic conditions during footwall burial, and footwall intrusive units place age constraints on structures and fabrics. These observations are used to produce a pre-extensional reconstruction of the NSRFTS illustrating a plausible geometry and mechanism by which these metasedimentary rocks were buried. Our pre-extensional NSRFTS reconstruction is then integrated with previously published mapping and balanced cross sections of the Confusion Range to the east (Greene, 2014) to

illustrate the regional style and magnitude of Mesozoic crustal shortening and thickening at

the NSR metamorphic core complex.
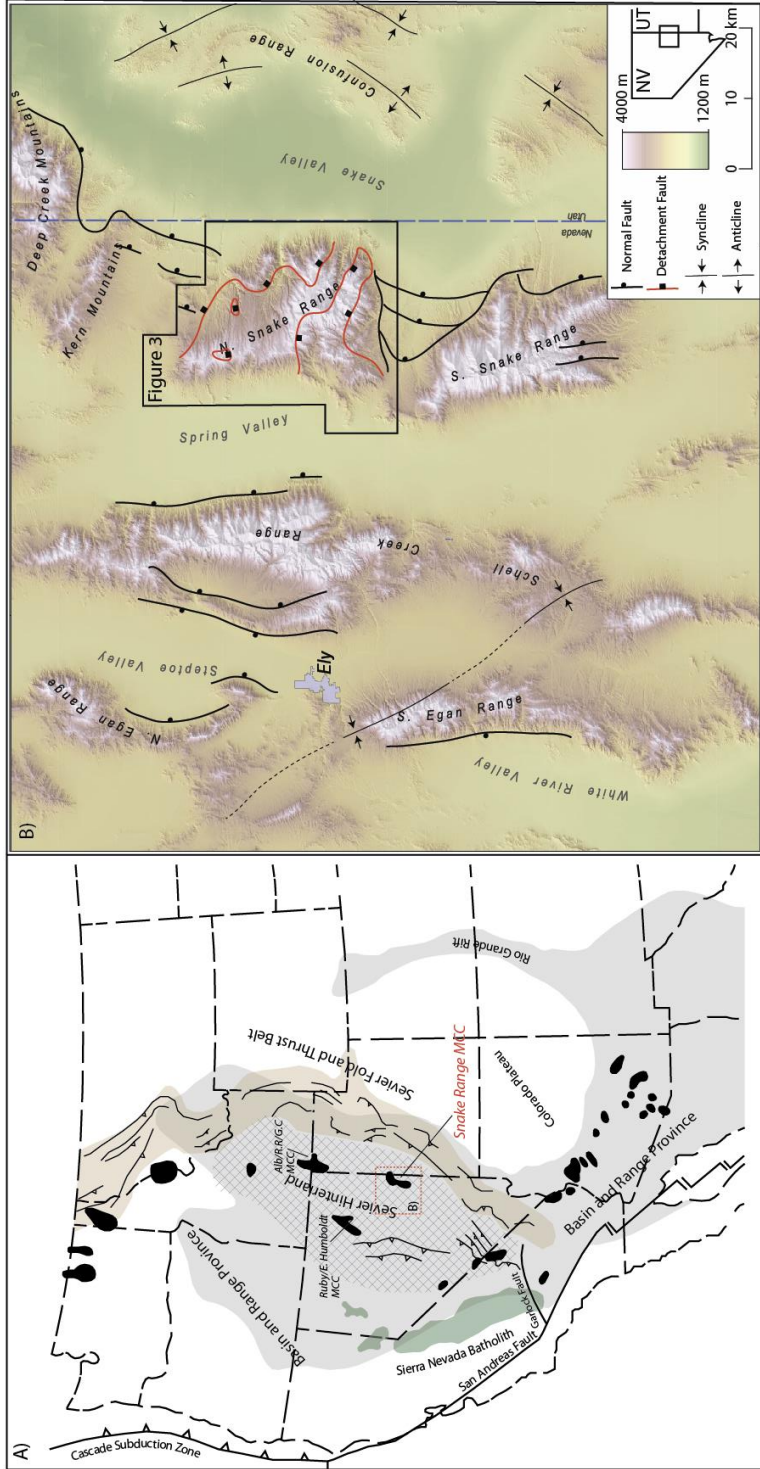
Figure 1: Regional geologic context of the northern Snake Range MCC. A) Map of western North America showing the location of the Basin and Range (gray), cordilleran metamorphic core complexes (black), Mesozoic magmatic arcs (green), the Sevier fold and thrust belt (tan), and the inferred Sevier hinterland (checkered). The Snake Range MCC (red box) is located within the proposed Sevier hinterland west the Sevier fold and thrust belt (Mod. from Coney, 1980 and Decelles and Coogen, 2006). B) Shaded relief map of the northern Snake Range and adjacent ranges. The approximate traces of major normal faults, folds, northern Snake Range decollement (red), and location of figure 3 are shown.

2. MESOZOIC BURIAL OF CORDILLERAN CORE COMPLEXES

Andean-style subduction of the Farallon Plate beneath the North American Plate during the
Andean-style subduction of the Farallon Plate beneath the North American Plate during the
Mesozoic was associated with Sevier Orogeny retroarc shortening and is inferred to have
resulted in the formation of a 50-70 km thick hinterland west of the Sierra Nevada volcanic
arc and east of the frontal portion of the Sevier fold and thrust belt (Decelles, 2004; DeCelles
et al., 2006; Chapman et al., 2015). Decelles (2004) speculates that there was a total ~350 km
of upper crustal shortening at the latitude of central Utah. The deep burial of at least some
supractrustal rocks during this regional shortening event is best recorded by metamorphosed
Paleozoic sediments exposed within the footwalls of cordilleran MCCs. Many studies have
now described the metamorphic and P-T histories of footwall units of MCCs, including the
Albion-Raft River-Grouse Creek MCC (e.g. Hoisch et al., 2002; Wells et al., 2012), Ruby-
East Humboldt MCC (e.g. McGrew et al., 2000; Hallett and Spear., 2014), Funeral
Mountains MCC (Wells et al., 2011; Beyene, 2011), Shuswap MCC (e.g. Norlander et al.,
2002; Cubley and Pattison, 2012), and the Northern Snake Range MCC (Miller et al., 1988;
Lewis et al., 1999; Cooper et al., 2010), to understand the timing and magnitude of Mesozoic
crustal thickening and subsequent cooling and decompression of the Sevier hinterland.
These studies generally suggest that uppercrustal sedimentary rocks experienced pressures of
6 to 8 kbar during metamorphism, suggesting metamorphism at depths of 20 to 30 km. While
such studies have provided broad constraints on mid-crustal metamorphic conditions, far
fewer studies have addressed the exact geometry and kinematics of structures responsible for
this crustal thickening and burial in the Sevier hinterland. An exception is the work by
Howard and others (Howard, 1966; Howard et al., 1979; Howard 1980; Snoke, 1980) and

10

Miller (1980) who recognized key folding and thrust relationships within the Ruby/East Humboldt and Albion-Raft River-Grouse Creek MCCs, respectively, that appear synchronous with regional metamorphism. However, these studies do not provide pre-extensional reconstructions and burial estimates of these structures.

2.1. Controversy regarding the magnitude of burial at the Northern Snake Range

Although most work on the northern Snake Range MCC has focused on its extensional history (e.g., Miller et al., 1983; Gans and Miller 1983; Bartly and Wernicke, 1984; Gans et al., 1985; Lee et al., 1987; Miller et al., 1999; Cooper et al., 2010b, Gébelin et al., 2011; Lee et al., 2017), all recognize that footwall rocks record an earlier history of Mesozoic plutonism and metamorphism (e.g., Miller et al. (1988)). Competing models of NSR evolution invoke different mechanisms and magnitudes of footwall burial and metamorphism, even if the actual burial structures are not explicitly identified. Miller et al. (1983) proposed that footwall amphibolite-grade metamorphism occurred at depths close to the units' original stratigraphic depths (10-12 km) and was driven by an elevated geothermal gradient (Figure 2a). This conclusion was influenced by Young (1960), Armstrong (1972), and Gans and Miller (1983) who noted that early Cenozoic successions in adjacent ranges were deposited exclusively on upper Paleozoic strata with minimal angular discordance, suggesting the Paleozoic succession in Eastern Nevada was relatively unaffected by major Mesozoic shortening structures. Miller et al. (1983, 1988) also noted the abrupt lateral and vertical metamorphic field gradients within structurally continuous units of the lower plate – localized gradients that were difficult to reconcile with regional burial. However, the early Tertiary unconformity is not exposed in the NSR and, thus, does not preclude the possibility of localized burial structures. Bartley and Wernicke (1984) argued that kyanite-grade

11

metamorphism in the Upper McCoy Creek group exposed in the southeastern NSR must have occurred far deeper than stratigraphic depths and proposed a model in which metamorphic units resided in the footwall of an east-vergent Mesozoic thrust plate that was later excised and exhumed by ~60 km of displacement on the NSRD (Figure 2b). However, there is little field evidence for the implied stratigraphic duplication or thrust relationships predicted by this model. Lewis et al. (1999) conducted GARB and GASP thermobarometry on kyanite-bearing schists of the upper McCoy Creek Group at Hampton Creek (southeastern NSR) and reported P-T estimates of 810 ± 70 MPa (8.1 ± 0.7 kbar) and 610 ± 50°C, equating to crustal depths of 30 ± 3 km, greatly exceeding the ~11 km stratigraphic depth. Lewis et al. (1999) proposed that burial of lower plate units was accommodated by west-directed thrusting and recumbent folding (Figure 2c), citing the west-to-east increase in metamorphic grade between the Egan Range, Schell Creek Range, and Snake Range, and the existence of a west-vergent recumbent anticline in the Deep Creek Range to the north (Rodgers, 1988). Subsequent thermobarometry by Cooper et al. (2010a) corroborated P-T results by Lewis et al. (1999) and describes a northward increase in metamorphic P-T from 6.0 ± 0.9 kbar and 507 ± 53°C (Hendry's Creek) to 8.0 ± 0.9 kbar and 573 ± 58°C (Hampton Creek) (Figure 3), equivalent to a burial difference of 0.8 to 13.6 km, over a ~4 km N-S transect. Such an abrupt northward increase in burial depth within the same stratigraphic unit would require that the footwall stratigraphy dipped northward ~60°, which, if true, is a compelling argument for localized thickening and burial. Cooper et al. (2010a) speculated that this localized thickening might be due to an E-W trending recumbent fold related to a lateral ramp in a Sevier fold/thrust system. Again, no such structure was explicitly identified.
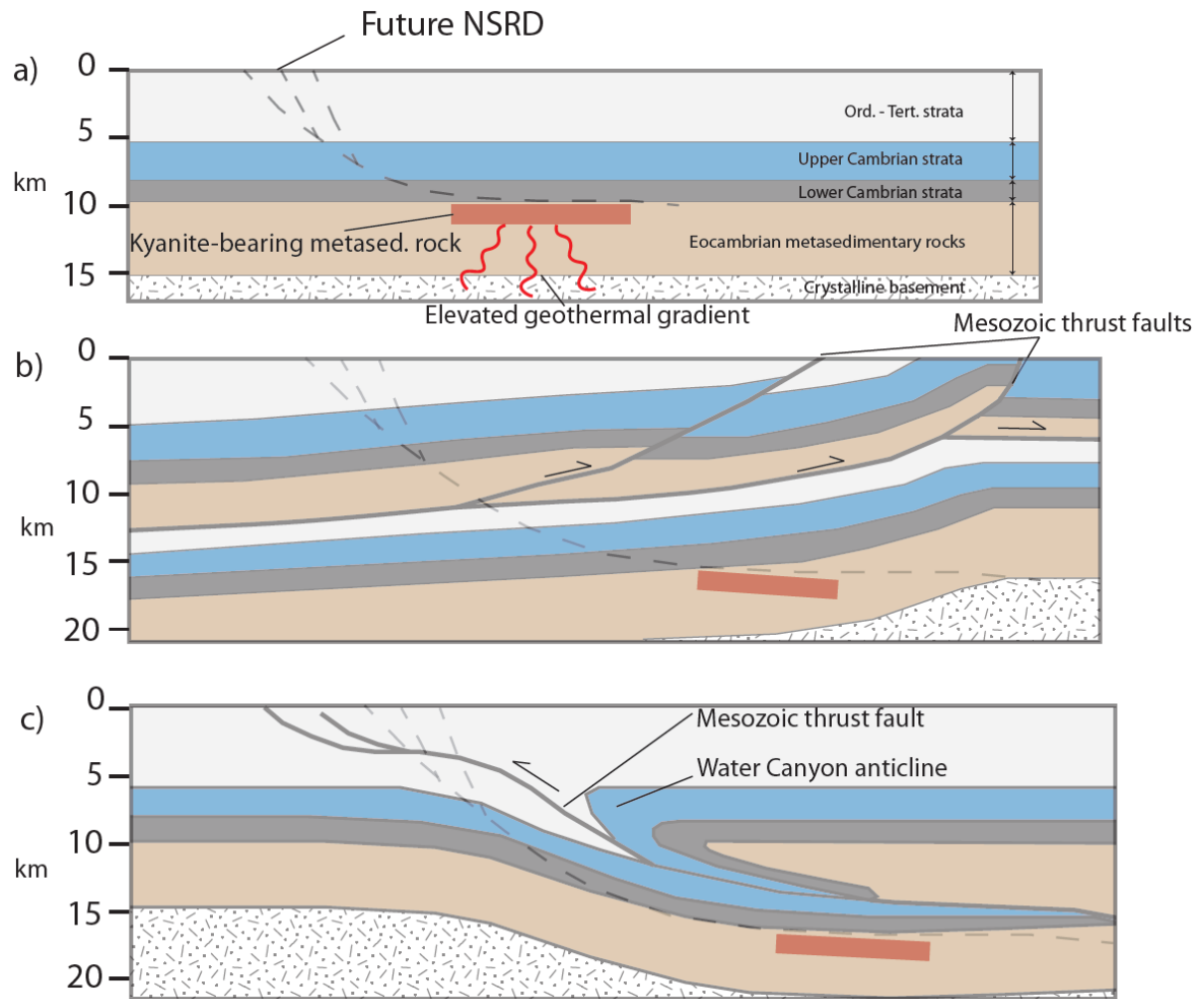
Figure 2: Previous models of metamorphism/burial of the NSR footwall. A) Metamorphism is the result of an increased geothermal gradient at normal stratigraphic depths (Miller et al., 1983). B) Metamorphism/burial in footwall of a major east-directed thrust (e.g. Bartley and Wernicke (1984). C) Metamorphism/burial in footwall of a west-directed fold/thrust (e.g. Lewis et al., 1999). No horizontal/vertical exaggeration.

2.1. Previous work in the northwestern NSR

The northwestern part of the NSR was first mapped by Nelson (1966), who recognized that the strained, marble-dominated stratigraphy is locally overturned by a map-scale fold that is cut by the Northern Snake Range Decollement (NSRD). Subsequent mapping by Hose and Blake (1976) and Gans et al. (1985) correlated the lower plate stratigraphy in this area with

13

lower to middle Cambrian units exposed in adjacent ranges and precisely delineated the trace of the NSRD, noting that in this part of the range NSRD is clearly oblique to footwall stratigraphy and cuts up-section toward the east (Figure 3). Later work by Lee (1990) described a map-scale recumbent fold, part of what we here name the OPRS, that locally overturns and duplicates middle to upper Cambrian units, but initially concluded that folding was related to Cenozoic shear along the NSRD. However, later work by Lee et al. (1999a) recognized that the fold's axial planar fabric is defined by synkinematic metamorphic mica growth, suggesting that the fold formed during Cretaceous prograde metamorphism rather than during Tertiary exhumation. Lee et al. (1999a) also documented localized older-on-younger relationships, part of what we name the Eightmile Thrust system (ETS), west of the O'Neill Peak recumbent syncline (OPRS) that place Lower Cambrian units atop overturned and upright Middle Cambrian strata (Figure 3). In addition to documenting footwall structures, Lee et al. (1999a,b) characterized three broad types of intrusive rocks within the lower plate of the northwestern NSR: Eocene muscovite-bearing rhyolite porphyry dikes (37.5-37.9 Ma, U-Pb Zircon; Lee et al. 2017), Eocene(?) mafic dikes, and Late Cretaceous pegmatitic/aplitic leucogranite bodies (~84 Ma, U-Pb Monazite; Huggins and Wright, 1989).

This study builds on this previous work by greatly increasing the resolution of existing geologic maps and documenting the precise locations, geometry, and character of various fabrics, folds, and faults associated with Late Cretaceous shortening and burial, and providing new constraints on their ages and pre-extensional geometry. Cambrian units are subdivided into members, enabling map-scale structures to be deciphered in greater detail. For the first time, the axial trace and hinge geometry of the OPRS is precisely delineated and characterized, and the scale and geometry of thrust relationships of the ETS are discussed.

14

Variably deformed intrusive phases are documented, and cross-cutting relationships are used to place relative age constraints on structures and fabrics. These new observations allow for the construction of detailed cross sections and an interpretive reconstruction of the NSRFTS that directly addresses the amounts of structural burial that might have occurred during Late Cretaceous shortening and help reconcile the discrepancy between thermobarometric and stratigraphic pressure estimates.
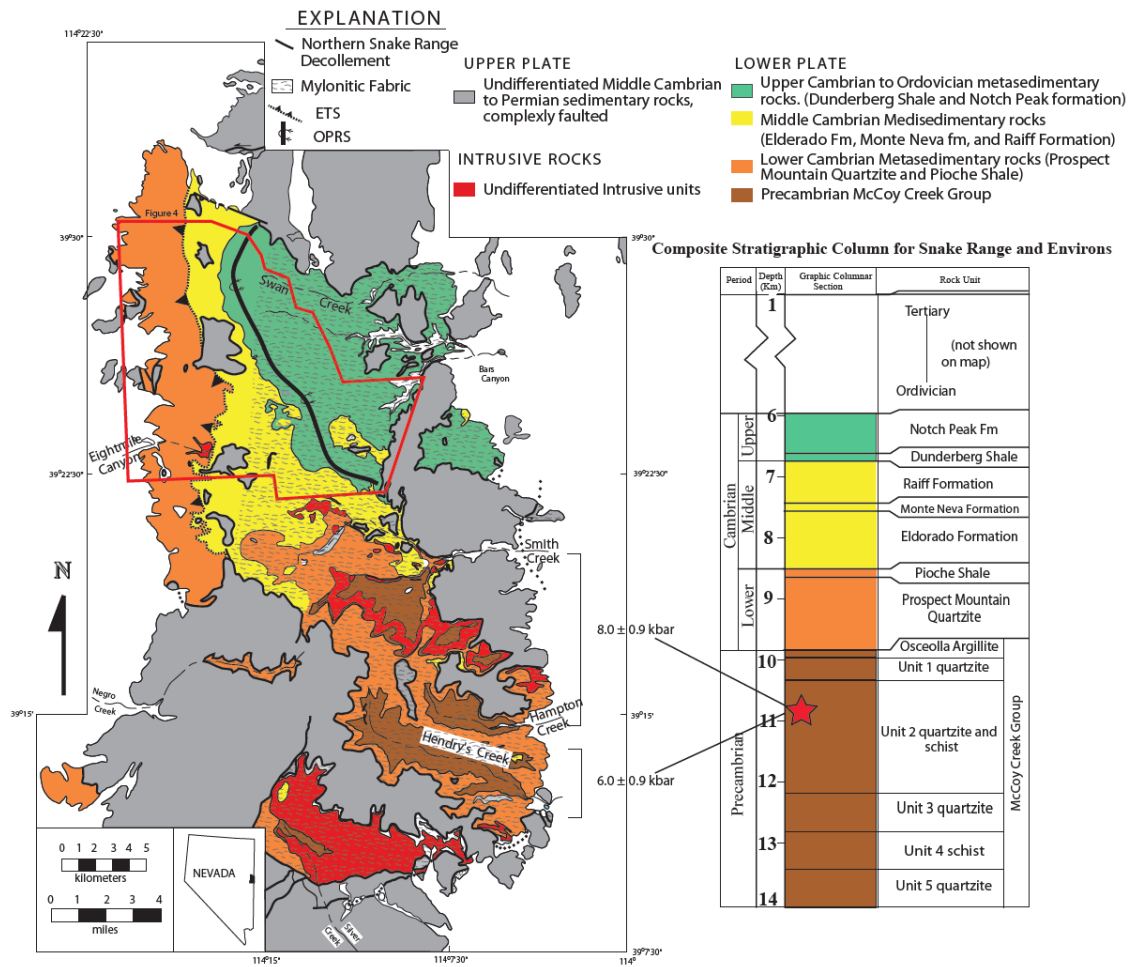
Figure 3: Simplified geologic map of the northern Snake Range compiled from Gans et al., (1999a,b), Lee et al., (1999a,b,c), and Miller et al., (1999a,b). The NSRD separates metamorphosed and variably mylonitized metasedimentary and intrusive rocks (colored) in the lower plate from unmetamorphosed, highly faulted upper plate strata (gray). Study area in the northwestern NSR (red polygon) hosts the trace of the OPRS and the ETS. Footwall mylonitic fabrics (stippled) die out to the west. The red star on stratigraphic column shows the original stratigraphic position of P-T data (Lewis et al., 1999; Cooper et al., 2010a). Location of figure 4 shown.

15

3. UNIT DESCRIPTIONS AND DISTRIBUTION

    3.1. Stratigraphy of lower plate metasedimentary rocks

The lower plate of the NSR MCC is composed of a thick succession of gently-dipping

quartzite, schist, and marble units intruded by a diverse suite of plutons, dikes, and sills of

various ages (Miller et al., 1983, 1988). Although originally interpreted as pre-Cambrian

basement by Misch (1960), the footwall metasedimentary rocks have been confidently

correlated to Eocambrian through upper Cambrian units of the miogeoclinal succession

observed in adjacent ranges (Hose and Blake, 1976; Hose and Whitebread, 1981, Miller et

al., 1983; Miller et al., 1999a,b; Gans et al., 1999a,b,c; Lee et al., 1999a,b) based on the

match of compositions, stratigraphic order, relative thicknesses, and distinguishing

characteristics (i.e. chert and/or dolomite abundance). Throughout much of the range, lower

plate units dip gently eastward and broadly parallel the NSRD (Miller et al., 1983). In the

southern half of the NSR, the NSRD is generally situated near the top of the lower Cambrian

Pioche Shale. However, in the northern NSR, progressively younger units appear in the

footwall as the NSRD cuts up-section towards the northeast, from Lower Cambrian units in

the west to upper Cambrian units in the east. In doing so, the NSRD obliquely cuts a series of

lower plate structures (thrust faults and folds) that are the focus of this study (Figure 3).

Seven Cambrian formations are exposed in the footwall within the study area: Lower

Cambrian Prospect Mountain Quartzite (Cpm), Lower Cambrian Pioche Shale (Cpi), Middle

Cambrian Eldorado Formation(Ce), Middle Cambrian Monte Neva Formation (Cmn),

Middle Cambrian Raiff Formation (Cr), Upper Cambrian Dunderberg Shale (Cd), and Upper

Cambrian Notch Peak Formation (Cn) (Figure 4). Detailed descriptions of each unit are
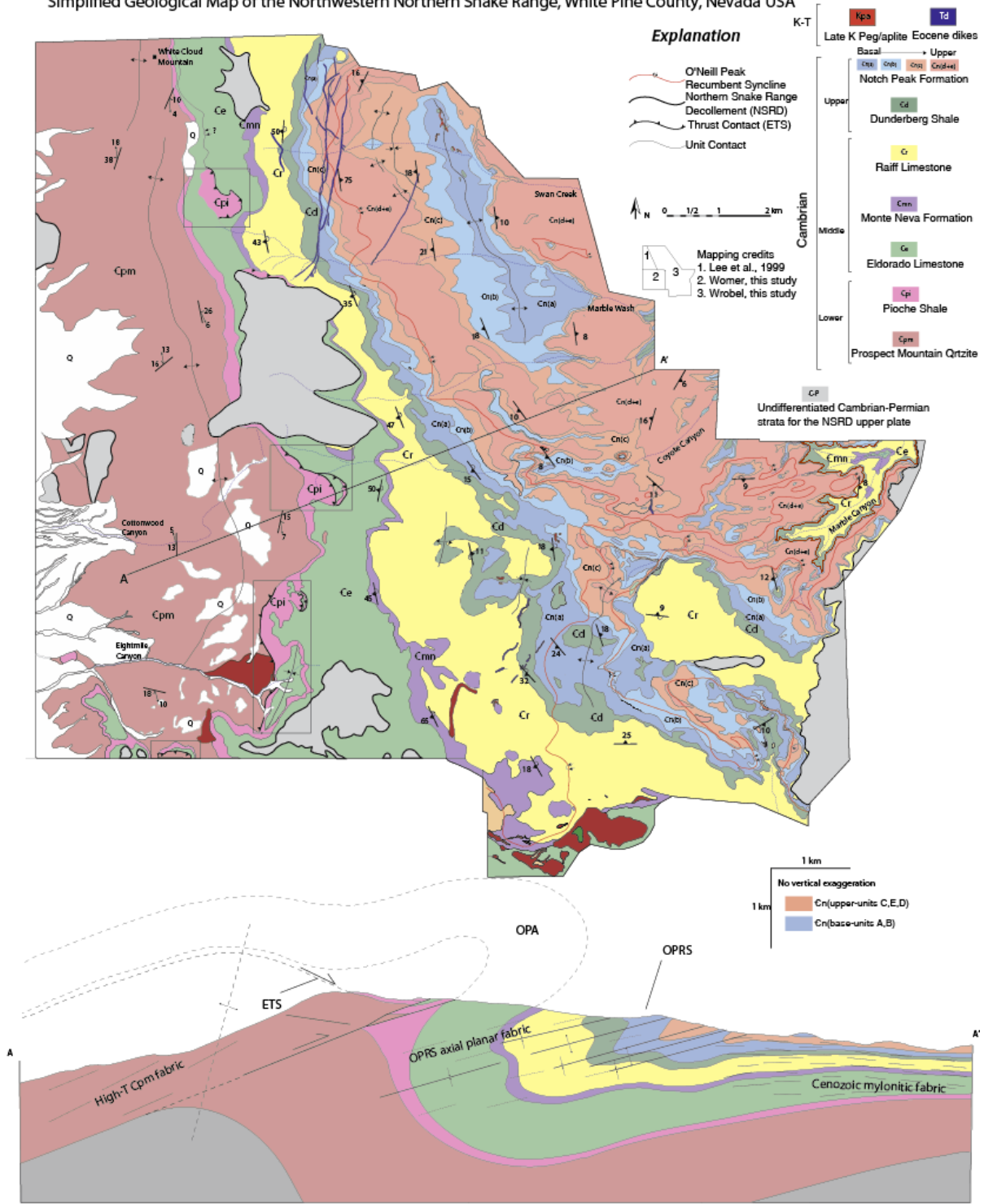
Figure 4: Simplified geologic map and cross section of the study area(compiled from Wrobel et al. (this study), Womer, (2017), and Lee et al. (1999a)). The approximate axial trace of the OPRS (dark red line (*Change Color*)) generally follows the upper members of Cn. Major thrust relationships of the ETS (black boxes) tend to follow the Cpm/Cpi/Ce contact. See Plate 1 for detailed map.

given in Table 1, and the stratigraphic positions and unstrained unit thicknesses are shown in the figure 3 stratigraphic column. The middle Cambrian unit nomenclature used here was originally proposed by Young (1960) and later adopted by Lee et al. (1999a,b) for the lower plate stratigraphy in the northern part of the range. Cn is subdivided into five informal members, Cna (basal member) to Cne (top member), based on color, mica content, and chert abundance (Table 1). The subdivision of Cn into these members was critical to delineating the location and geometry of the OPRS during the geologic mapping phase of the study. Cn members are combined into *lower Cn* (Cnl), comprised of Cna and Cnb, an *upper Cn* (Cnu), comprised of Cnc, Cnd, and Cne for clarity on the simplified cross sections.

The lower plate stratigraphic units crop out in generally NW-SE trending strips, with Cpm exposed on the western flank of the range, Cpi and Ce exposed along the crest of the range, and younger units exposed to the east (Figure 4, Plate 1). However, the distribution and orientations of units are complicated by the OPRS and thrust relationships of the ETS. Cpm in the western map area is generally upright and folded into a broad N-S trending upright anticline, whereas Middle-Upper Cambrian units to the east progressively steepen and fan through vertical to become west-dipping and overturned, part of the upper limb of the OPRS (Figure 4 cross section). East of the OPRS axial trace, the overturned limb has been largely removed by erosion and by displacement on the NSRD, and mainly the upright subhorizontal lower limb strata are preserved (Figure 5).

Unmylonitized units in the overturned limb of the OPRS have thicknesses comparable to unstrained equivalent strata in the upper plate. With increasing younger mylonitization towards the east, units are dramatically thinned – in some instances to as little as 10% of their

original stratigraphic thickness. Within the hinge region of the OPRS, units are ≥30% thicker than their original stratigraphic thickness.

Previous metamorphic studies of the NSR footwall focused primarily on the Eocambrian units exposed in the deep canyons of the southeastern part of the range and not on the assemblages and fabrics in the northwestern part of the range. In this study, metamorphism within Cpm is evidenced by recrystallized amoeboid quartz grains, mica and garnet growth within schistose interbeds, and the development of metamorphic foliation oblique to bedding (discussed in later sections). Cpi is a muscovite-biotite schist with abundant tourmaline and

Figure 5: Map overlay showing the distribution of overturned (red) vs. upright (blue) stratigraphy in the OPRS. Black dots signify upright strata west of the OPRS/OPA/EMT system and green regions are ambiguous.

minor garnet but lacks staurolite, kyanite, and other index minerals observed in the lower stratigraphic units to the southeast. Ce, Cr, and Cn are relatively pure carbonate (both calcite and dolomite) marbles. Impure (originally silty limestone) horizons within this succession locally contain phlogopite/high-Mg biotite and quartz. Calc-schist units Cmn and Cd contain assemblages of cal + qtz + phlog ± bio ± plag ± tremolite ± titanite (Lee et al., 1999) and cal + quartz + phlog + czo + ep (aln) ± titanite, respectively. Epidote (aln) is severely retrogressed and mantled by stable czo. These calc-schist assemblages are broadly

19

representative of upper greenschist to lower amphibolite facies. The conspicuous lack of higher temperature index minerals such as diopside, wollastinite, garnet, and forsterite suggests temperatures did not greatly exceed 500°C (Spear, 1995) although pressures for these units remain largely unconstrained.

Table 1. Unit descriptions and thicknesses

Period	Unit			Thickness		Description
				Max thickness	Mylonite zone	
Upper Cambrian	Notch Peak Formation(Cn)		Cn(e)	40m	5m	Gray and white banded medium-grained marble with locally abundant cm- to dm-scale chert nodules. The unit is micaceous at its base and becomes more pure at the top.
			Cn(d)	50m	5m	Slope- to ledge-forming tan/brown medium-grained marble interbedded with m-scale intervals of pure blue marble. Rare chert nodules present at the top of the interval.
			Cn(c)	~50m	10m	Ledge-forming white/blue/gray banded (cm-scale) pure marble with cm-dm scale chert nodules at base. Meter-kilometer scale unfoliated dolomite pods are common in the southern study area.
			Cn(b)	~60m	3m	Slope- to ledge-forming, gray/brown, well-foliated, micaceous marble with variable chert.
			Cn(a)	~60m	5m	Cliff- to ledge- forming, chert-rich, pure to micaceous blue/grey marble. Chert nodules/stringers range from 1 mm-3cm thick. Base: 1-2m thick recessive white marble (at contact with underlying Dunderburg Shale).
	Dunderburg Shale (Cd)			150m	5-15m	Slope- to ledge- forming medium-grained high-Mg biotite + phlogopite + quartz ± clinozoisite ±epidote ± titanite ± tremolite (Lee et al., 1999) calc-schist with 1-10m thick schistose intervals with coarse high-Mg biotite porphyroblasts
	Raiff Formation (Cr)			400-500m	50-100m	Ledge- to cliff-forming moderately- to weakly-foliated white and blue marble with a laterally discontinuous 10-30m thick tan calc-schist intervals. 100m-scale pods of unfoliated dolomite are common.
Middle Cambrian	Monte Neva Formation (Cmn)			75-100 m	~30 m	Slope-forming brown to tan medium to coarse-grained high Mg bt ± phlog calc-schist with intervals of clinozoisite + quartz ± plag ± titanite (Lee et al., 1999). The upper contact with Cr is grey/black and platy.
	Eldorado Formation (Ce)			>600 m	Not observed	Ledge- to cliff-forming medium-grained white-blue alternating (m-scale) marble and occasional pods of unfoliated dolomite (less abundant than Cr). Basal contact with Cpi is gradational with alternating intervals of impure marble, calc-schist, and schist.

Lower Cambrian	Pioche Shale (Cpi)	<200m	Not observed	Slope-forming greenish-brown to dark-brown slope-forming muscovite-biotite-quartz schist and contains garnet near the basal contact with Cpm.
	Prospect Mtn Quartzite (Cpm)	>600m	Not observed	Cliff- to ledge-forming rust-brown to grey quartzite 5-15% muscovite and biotite with accessory feldspar, zircon, and rutile.

3.2. Intrusive Rocks

The lower plate of the northern Snake Range MCC hosts a diverse suite of plutons, dikes, and sills including, a) Jurassic (~160 Ma) diorites to granites, b) a mid Cretaceous (~100 Ma) orthogneiss, c) abundant, scattered Late Cretaceous two-mica ± grt aplite/pegmatite dikes, d) Eocene granitoid plutons, dikes and sills, and e) rare early Miocene dikes (Miller et al., 1983, 1988; Huggins and Wright, 1989; Lee et al., 2017). In the study area, intrusive units account for a very small fraction of footwall rocks and many are too small to be illustrated on the map (Plate 1), yet they provide key relative age constraints on structures and fabrics that are the focus of this study. Broadly, two different intrusive phases are observed in the study area: Late Cretaceous leucogranite dikes, sills, and small irregular plutons (Kpa), and Eocene felsic and mafic dikes and sills (Td). We subclassify Td intrusive phases into 4 separate rock types based on composition, as shown in Table 2.

Kpa dikes, sills, and small plutons are widely dispersed and occur at all scales, with the most voluminous intrusions exposed in Eightmile canyon and the north fork of Smith Creek (Figure 4). A single dike or sill may consist of alternating bands of coarse-grained pegmatite and aplite with gradational internal contacts. The unit's light color, paucity of mafic minerals, and ubiquitous presence of magmatic muscovite and garnet indicate Kpa intrusions are strongly peraluminous – part of a widespread suite of Cordilleran S-type granites (Miller and

21

Bradfish, 1980) interpreted to have been produced by crustal melting driven by Sevier-Laramide crustal thickening. Only a small fraction of Kpa bodies are dated, but an age of ~84 Ma from Smith Creek (Huggins and Wright, 1987) and preliminary new ages ranging from of 75 Ma to 85 Ma (Womer, 2017) suggest that virtually all of these Kpa bodies are part of the same Late Cretaceous magmatic event.

Td dikes and sills are concentrated in a NS-trending dike swarm in the headwaters of Swan Creek, but also crop out as isolated dikes and sills throughout much of the northern NSR (Figure 4). Dikes range in composition from hbl-rich diorite to porphyritic musc-bearing rhyolite, are typically 5-30m wide, >1km long, and dip steeply (70-80°) eastward. Generally, dikes are poorly exposed but are easily identified in aerial imagery by linear strips of high-density vegetation. In the northwestern study area, Eocene dikes are effectively undeformed, but to the south and east, dikes become progressively more affected by younger mylonitic fabrics. U/Pb geochronology of zircon from three felsic dikes yield ages of 37.806 ± 0.026, 37.531 ± 0.009 Ma, and 37.504 ± 0.014 Ma (Lee et al., 2017).

Our preliminary U-Pb LA-ICPMS results from additional dikes range from 36 to 38.5 Ma (Table 2) and are broadly in agreement with the 37.5-37.8 Ma ages reported by Lee et al. 2017. These results will be presented and discussed in a forthcoming publication. Here, we will use the Lee et al., 2017 to interpret the relative ages of various structures.

Table 2 Geochronology and descriptions of intrusive units

Sample name	Type	Age (Ma)	UTM (east)	UTM (north)	Description
AW-NSR-44	Cretaceous/Tertiary pegmatite/aplite (KTpa)	78.12±0.61	736912	4373602	Fine- to coarse-grained qtz + plag + musc +bio ± grt leucogranite. Forms irregular pods (m-km scale) and discontinuous dikes)
JSR-08		81.82±0.67	733264	7362966	
AW-NSR-01	Eocene quartz monzodiorite (Tqmd)	38.45±0.24	733720	4373134	Med- to coarse-grained. Contains plag (50%) + hbl (35%) + qtz (10%) + bio (5%). Hornblende is euhedral and often psedomorphed by chlorite, giving the unit a distinct green color.
AW-NSR-7	Eocene Hbl microdiorite (Tmd)	37.7±3.1 Ma (youngest concordant age)	734612	4371365	Fine-grained, equigranular plag (50%) + bio (30%) + hbl (15%) + qtz (5%) ± cpx microdiorite.
JSR-03		36.99±0.27	734061	4364964	
AW-NSR-11	Eocene rhyolite muscovite porphyry (Trmp)	38.57±0.42	734493	4373183	White/tan, fine- to medium-grained rhyolite porphyry. Qtz + musc + plag ± biotite phenocrysts within a qtz-feld-musc aplitic groundmass. Phenocrysts range from 1mm-3mm and total phenocryst percentages range from 5-15%.
AW-NSR-16		37.98±0.18	734628	4374470	
AW-NSR-GM	Eocene quartz kspr porphyry (Tqkp)	36.59±0.29	734953	4374445	Rhyo-dacite porphyry containing 2mm-2cm kspar phenocrysts and 2mm-1cm quartz phenocrysts within a fine- to medium-grained plag + bio groundmass.
AW-NSR-13		36.14±0.25	734659	4373754	

4. STRUCTURAL GEOLOGY OF LOWER PLATE UNITS

4.1. O'Neill Peak Recumbent Syncline (OPRS):

The dominant structural feature of the northwestern NSR is the OPRS: a km-scale, NNW-trending, eastward-opening, inclined-to-recumbent syncline that affects the entire middle and upper Cambrian stratigraphic section. The NSRD cuts obliquely across the OPRS, from upright Cpm in the west to overturned strata of the OPRS upper limb at the crest of the range, to upright strata of the OPRS lower limb to the east, and, as a result, removes most of the overturned limb and any overlying structures. Units within the OPRS hinge are steeply east-dipping to vertical and exhibit abundant parasitic folding at the meter- and cm-scale. The

orientation of the axial plane varies from moderately west-dipping to horizontal, and the axial trace in map view is highly sinuous, reflecting the intersection of the gently dipping axial surface with the deeply incised topography (Figure 4).

At the northernmost exposures of the OPRS, younger mylonitic deformation is largely absent such that the original hinge structures and associated hinge fabrics are well preserved. Here, the OPRS has a consistent interlimb angle of ~40°, preserves a moderately (28-34°) west-dipping axial planar fabric (see later section), and unit thicknesses within the hinge increase ~30% (Figure 6a and 7) compared to unstrained equivalent strata in the upper plate. A discontinuous anticlinal 'buckle' locally gives the hinge a syncline-anticline-syncline 'W'-shape (Figure 7). Meter- to cm-scale parasitic folds are common within the hinge zone and have similar apical angles, axial plane orientations, and hinge thickening magnitudes as the greater OPRS (Figure 6c). Planar N-S trending, steeply dipping Eocene dikes in this region consistently cut the OPRS hinge and limbs, demonstrating that the folding must be older than ~37 Ma.

To the south and east, mylonitic fabrics severely deform the OPRS, tightening the fold into an isoclinal geometry, rotating the axial plane to subhorizontal (Figure 7), and completely transposing units within the hinge zone, such that the axial trace/axial surface is only identifiable by the reversal from upright to overturned in the middle-upper Cambrian stratigraphy. This mirroring of the stratigraphy across the axial surface is particularly evident along the cliffs of Marble Canyon and associated tributaries (Figure 6b). Parasitic folds within the hinge and limbs of the mylonitized OPRS mimic the isoclinal geometry and recumbent orientation of the greater OPRS in this region and display significantly more

hinge thickening and limb thinning than in less mylonitized regions to the north and west (Figure 6d).

Figure 6: Field photos/sketches of the OPRS. A) Field photo and annotated sketch of the northern OPRS hinge zone near Swan Creek. B) Field photo and annotated sketch of the southern OPRS hinge zone in Marble Canyon. c) Typical parasitic fold in the northern OPRS hinge zone with an apical angle of ~40˚. D) Typical isoclinal and recumbent parasitic fold in southern OPRS hinge zone.

The OPRS hinge is non-cylindrical at the km-scale. From northern to southern exposures, the hinge line rotates ~70° anticlockwise, from an ~025˚ (205˚) trend in the north to ~137˚ (317˚) in the south (Figure 7). It is unclear how much of this non-cylindricity reflects the original geometry of the OPRS, or if it is due entirely to rotation toward the principal stretch direction associated with the subsequent mylonitic strain.
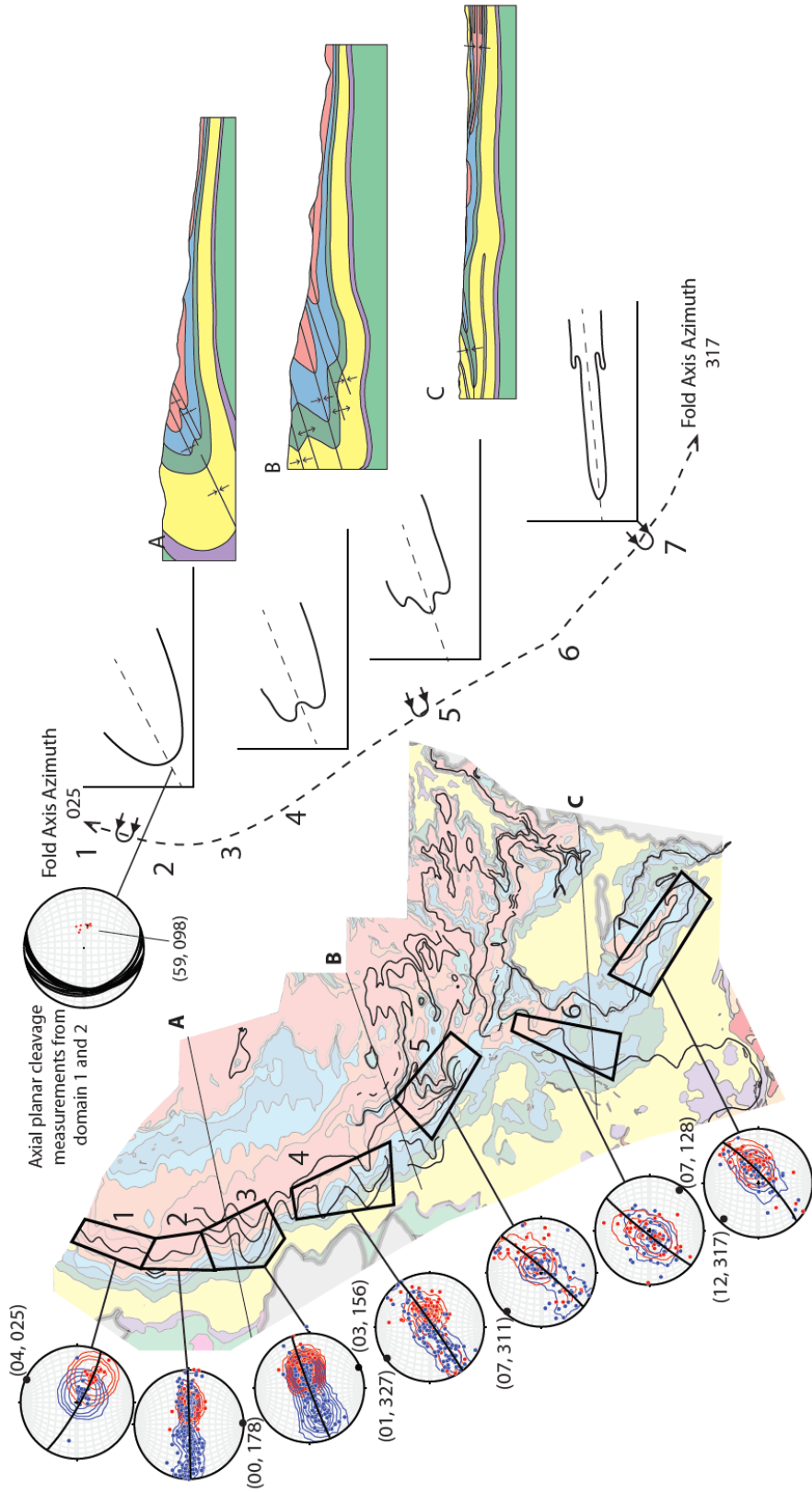
Figure 7: Structural data and cross sections showing variation in OPRS geometry and fold shape. *Left)* Lower hemisphere stereographic projections of poles to upright (blue) and overturned (red) compositional layering for 7 'domains' along the OPRS hinge, from which the fold axis orientation is calculated (cylindrical best fit). *Center)* Sketch showing N-S variations in fold axis orientation, fold/hinge shape, and axial plane orientation. From north to south, the OPRS hinge tightens and the axial plane rotates from moderately west-dipping to horizontal. *Right)* Cross sections of 3 EW transects across the OPRS illustrating changes in fold shape and orientation.

A fence diagram of the OPRS consisting of 13 EW-trending and 8 NS-trending cross sections was compiled using Midland Valley Exploration's MoVE software, and a 3-D model of the axial surface was generated from the intersection of the axial trace with topography and its projection into the subsurface (Figure 8 and supplemental material). The model shows the axial surface of the OPRS has been broadly refolded into an open, asymmetric, N-S trending antiform. We attribute the folding of the axial surface to rotation/shearing of the originally west-dipping axial plane towards parallelism with the east-dipping mylonitic fabric.

4.1. Eightmile Thrust System (ETS) and O'Neill Peak Anticline (OPA)

West of the OPRS hinge zone, compositional layering within Upper to Lower Cambrian units gradually fans from the west-dipping Cn to Ce of the overturned limb through vertical to steeply east-dipping (upright) within Ce, Cpi, and uppermost Cpm, and ultimately through horizontal to gently west-dipping on the western flank of the range (Figure 4; Plate 1). The transition from overturned to upright towards the west indicates the presence of a paired anticline, the O'Neill Peak Anticline (OPA), atop the OPRS whose hinge would approximately coincide with the transition from overturned to upright within Ce, just east of its stratigraphic contact with Cpi (Figure 4 cross section). The axial trace of this fold is not indicated on the map because of difficulties identifying the precise hinge location within the monotonous Ce marbles. Specifically, the lack of well-defined compositional layering in many areas, heterogeneous strain, mesoscopic folding, and difficulty resolving between original bedding, axial planar foliation, and younger mylonitic fabrics results in a chaotic pattern of mapped foliation attitudes in this region and considerable ambiguity as to the precise location of the map-scale hinge (see Womer, 2017).
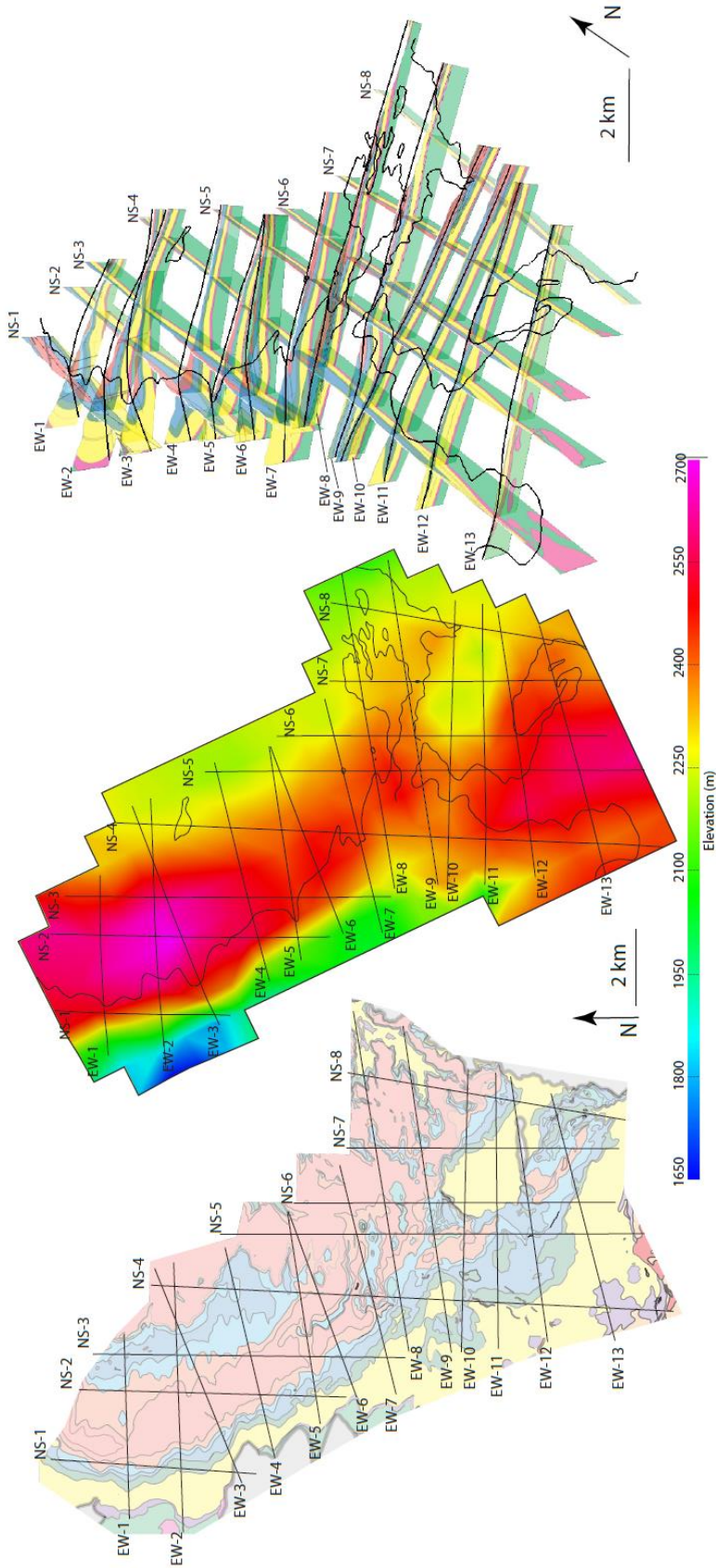
Figure 8: Elevation color map of the modeled OPRS axial surface (*center*) and fence diagram of the OPRS (*right*) derived from EW and NS cross section (*left*). The OPRS axial surface has been folded into an open, NNW-SSE trending anticline. The sinuous black line represents the intersection of the axial surface with topography. Fence-diagram of the OPRS is comprised of 21 cross sections. 3-D PDF version of fence diagram provided in supplemental material.

Just to the west of the inferred location of the OPA are several distinct, generally west-dipping (20-40°), older-on-younger (thrust) relationships of the ETS that duplicated Lower to Middle Cambrian stratigraphy (black boxes, Figure 4). These faults are most obvious where they juxtapose different stratigraphic units (e.g. Cpm on Cpi or Cpi on Ce) and tend to form isolated discontinuous map traces. This is mainly an artifact of the difficulties in tracing these faults along the heavily-forested steep western flank of the range, especially where they occur entirely within a single formation. Our preferred interpretation is that the ETS is a continuous thrust system with numerous imbricate splays that generally follow the map trace of Cpi and the axial surface of the OPA. One exceptionally well-exposed thrust relationship in Eightmile Canyon places Cpm atop Ce and omits Cpi (Figure 9a). Slip estimates for these faults are poorly constrained because of their low angle to bedding in the hanging wall and footwall and the lack of clear hanging wall/footwall cutoffs. However, at the Eightmile Canyon exposure, there is >200m of stratigraphic duplication, and, given the low bedding to fault angle, we conclude that total east-directed slip likely exceeds several kilometers. To the south, both the OPRS and OPA die out or veer off to the east. However, the ETS continues as a simpler and more continuous structure that places upright west-dipping Cpm on a west-dipping upright section of Cpi and Ce.

In the ETS exposure in Eightmile Canyon, the metamorphic fabric (discussed in the next section) appears to pass smoothly across the sharp lithological (thrust) contact between hanging wall quartzite (Cpm) and footwall marble (Ce) with apparent intensification of the foliation in the marble directly beneath the contact. This, and the absence of an obvious metamorphic break across these contacts, suggests the thrusting either predated or was

29

synchronous with metamorphism. In a few areas, undeformed Eocene dikes and sills intrude along and cut across segments of the ETS, clearly demonstrating pre-Eocene slip (Womer, 2017).

The most obvious structural manifestation of the thrust-related deformation (apart from the stratigraphic duplication) is the ubiquitous tight to isoclinal m-scale folding of Cpi in the immediate vicinity of the known or inferred ETS thrust contacts (Figure 9b). Unlike the mesoscopic folds associated with the OPRS, these folds are highly variable in their orientation, morphology, and asymmetry. Overlying Ce and underlying Cpm are relatively undeformed, suggesting that Cpi accommodated significant layer parallel shortening, and likely acted as a detachment horizon between broadly folded Cpm and the overlying middle-upper Cambrian strata involved in the OPRS.

Figure 9: Field images of an ETS thrust relationship and associated folds. A) Well-exposed thrust relationship of the ETS in Eightmile canyon that places Cpm atop Ce. B) Severely folded Cpi proximal to an ETS thrust zone. Not shown: overlying Ce and underlying Cpm do not display comparable folding. Brunton for scale.
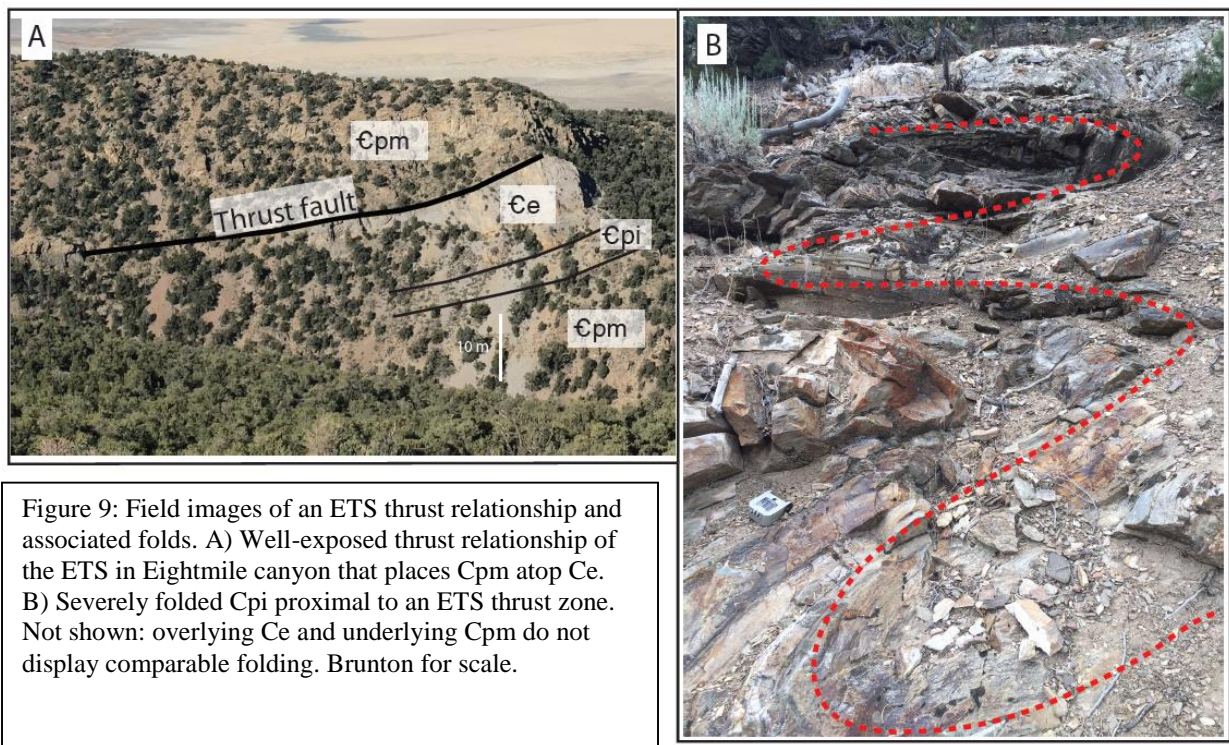
The precise geometric relationship between the ETS, OPA, and OPRS is ambiguous. One possibility is that ETS exposures represent localized thrust splays associated with km-scale layer parallel detachment faulting along Cpi between Cpm and the overlying middle Cambrian carbonate section. Another possibility is that ETS thrusts are relatively small-displacement splays associated with a much larger overriding thrust plate that has since been transported eastward by the NSRD. A final possibility is that ETS exposures represent late-stage (post-Cpi detachment) thrust relationships that accommodated shortening within the hinge of the OPA. Though present field exposures cannot explicitly rule out any of these structural relationships, as discuss further below, the abundance and geometry of mesoscopic folding in Cpi, in contrast to relatively unfolded underlying/overlaying strata, is likely the result of several km of layer parallel slip and shortening, and that this detachment along Cpi was critical to the formation of the OPRS/OPA..

4.2. Metamorphic tectonite fabrics related to crustal shortening

Throughout most of the NSR footwall, the obvious tectonite fabric is a retrograde mylonite fabric associated with Cenozoic unroofing and exhumation. However, in the northwestern footwall older synmetamorphic tectonite fabrics are well preserved.

On the western flank of the range, Cpm and Cpi display a low strain but high temperature fabric associated with synkinematic growth of muscovite, biotite, and locally garnet. This fabric is defined by a micaceous foliation that generally dips westward with respect to bedding and a NNW-trending intersection lineation that is parallel to a weak stretching lineation. The foliation planes are difficult to measure directly in the field because Cpm rarely parts along the foliation surfaces. The fabric is best observed in thin-section, where a continuous foliation is defined by well-aligned metamorphic biotite and muscovite, and a

crude grain shape foliation of large recrystallized quartz grains (Figure 10a). Quartz grains display abundant evidence of high-temperature dynamic recrystallization by grain boundary migration (GBM) including highly ameboid and interlobate grain boundaries and pinning/island structures, as well as a younger, much lower temperature deformation evidenced by abundant deformation lamellae and local bulging recrystallization (BLG). The high-temperature fabric suggests deformation at ~550-650°C (Stipp et al., 2002) during peak (bio-garnet grade) metamorphism. The low-temperature deformation mechanism (BLG) may record the very weak, low-temperature overprint associated with later extension.

Several Kpa intrusions are involved in the high-temperature Cpm fabric at the grain- and outcrop-scale, whereas, other Kpa intrusions and all Eocene intrusive phases clearly crosscut the Cpm fabric. This suggests that the high-temperature fabric is broadly coeval with Kpa emplacement (78-84 Ma) and distinctly older than 36 Ma. We interpret this fabric to be a higher temperature version of a regional fabric observed at deep stratigraphic levels throughout eastern Nevada (e.g. Schell Creek Range, Deep Creek Range, southern Snake Range) that is interpreted to be a consequence of east-directed layer parallel shear and layer parallel shortening during Late Cretaceous shortening (Miller et al., 1989).

Ce, Cmn, Cr, Cd, and Cn in the northwestern NSR also preserve a west-dipping tectonite foliation. In these units the foliation is clearly axial planar to the OPRS and associated parasitic folds. In the field, this fabric is easily measured along micaceous parting surfaces and cleavages within the hinges of parasitic folds and is oblique to the younger horizontal to gently east-dipping mylonitic fabric that becomes more strongly developed toward the east (Figure 10b, d). In thin section, the older west-dipping (axial planar) fabric is defined by the alignment of synmetamorphic phlogopite/high-Mg biotite (Figure 10e), a weak grain shape

foliation in calcite, consistent alignment of calcite twinning planes, and a well-defined grain-

shape foliation in recrystallized quartz (Figure 10c). Recrystallized calcite grains have

straight to irregular grain boundaries and exhibit serrated patchy twins and tapered lensoid

Figure 10: Field images and photomicrographs of synmetamorphic (pre-extensional) fabrics. A) Photomicrograph of Cpm showing grain boundary migration of quartz in the high-temperature Cpm fabric (image width=6mm). B) Annotated outcrop image of a folded chert layer in the OPRS hinge zone. C) Photomicrograph of the axial planar fabric in the hinge of parasitic fold (see B). Fabric is defined by a grain shape foliation in recrystallized quartz (width=6mm). D) Outcrop photo of the OPRS axial planar cleavage orthogonal to compositional layering. E) Photomicrograph of the OPRS axial planar fabric in the Dunderberg Shale (calc-schist). Fabric is defined by the alignment of synmetamorphic phlogopite/High-Mg biotite (width=6mm).

twins subparallel to the axial planar fabric, indicating deformation temperatures >250°C

(Ferrill, 1991; Burkhard, 1993; Ferrill et al., 2004). Quartz grains exhibit bulging

recrystallization and undulatory extinction, suggesting deformation temperatures of 300-

400°C (Stipp et al., 2002). The growth of synkinematic phlogopite/high-Mg biotite indicates

the axial planar fabric, and, therefore, the formation of the OPRS, is broadly coeval with Late

Cretaceous prograde metamorphism.

5. A PLAUSIBLE RECONSTRUCTION OF THE LATE CRETACEOUS ARCHITECTURE OF THE NORTHERN SNAKE RANGE

We attempt a reconstruction of the Late Cretaceous architecture of the northern Snake Range and environs from the paleo surface to the structural depths represented by the lower plate metamorphic rocks, including the OPRS, OPA, and ETS (collectively, the NSRFTS). Using the previously described structures and relations, some reasonable geometric assumptions, and structural relationships exposed in the Confusion Range to the east (e.g. Greene, 2014), our reconstruction shows what an E-W cross section across the northern Snake Range region likely looked like immediately after Late Cretaceous crustal shortening and thickening. This section goes a long way towards reconciling the discrepancies between P-T estimates for NSR footwall rocks derived from thermobarometry and their original stratigraphic depth. Our reconstruction honors all available geologic constraints presently exposed at the surface but is admittedly speculative given how much of the original structural section has either been lost to erosion or now lies buried beneath the adjacent valleys and ranges. In addition, the reconstruction makes several explicit assumptions:

i. The original (Cretaceous) OPRS and OPA fold geometries are best preserved in the northern part of the NSR – where they have an apical angle of ~40°, a moderately west-dipping axial surface (~28-34°) and show evidence for substantial synmetamorphic passive amplification and hinge thickening. To the south and east, the rotation/warping of the OPRS axial surface and transformation into a recumbent and isoclinal fold is a consequence of superimposed extensional mylonitic shearing and strain – strain that we retrodeform in our reconstruction.

ii. We assume that the axial surface of the OPRS and OPA originally dipped ~45° to the west and that the Cpm now on the western flank of the range was approximately horizontal at the beginning of shortening. As the OPRS and OPA grew, tightened, and additional shortening structures developed in overlying strata, the axial surfaces gradually rotated eastward to subhorizontal, partly due to the tightening and eastward shear of the folds but also due to the downward bowing of the entire section as a consequence of the increased load associated with localized crustal thickening.

iii. By the end of shortening, the entire Paleozoic shelf strata between the Schell Creek Range and the western flank of the Snake Range must have had a significant eastward dip (~5-10°). Evidence for this comes directly from the much higher metamorphic grade of the Eocambrian units in the Snake Range as compared to the Schell Creek Range and from the observation that that the basal Eocene unconformity climbs eastward over this distance from Mississipian rocks in the Schell Creek Range to rocks as young as Triassic in the strata that were atop the Snake Range at the time – a stratigraphic relief of > 3 km.

iv. The NW part of the NSR is assumed to have been tilted 15° westward since the Eocene, based on the average orientation of Eocene dikes. We recognize that different parts of the NSR footwall may have complex rotation histories and record different magnitudes of rotation at different times, but we assume that the axial surface of the OPRS and OPA dipped ≤20° to the west in the Late Cretaceous.

v. The OPRS and OPA are an asymmetric anticline-syncline pair associated with a major ductile fault propagation fold/trishear system resulting from top-to-the-east

shear and layer parallel shortening. Much of the upper portion of this fault-fold system has been displaced eastward by slip along the NSRD and earlier shearing.

vi.   We assume ~30 km of top-east displacement occurred along the NSRD and/or older east-directed extensional shear zones. Displacement along the NSRD must be >20km based on the lack of hanging wall and footwall matches (piercing points) across the width of the range. In the Kern Mountains to the north, Gans (1986) estimated ~28km of slip along the NSRD based on the offset of Tertiary volcanic units. For our reconstruction, we assume 30km of total top-to-the-east slip/mylonitic shear and/or E-W extension between the western flank of the NSR and the Confusion Range to the east. This amount of deformation restores the Confusion Range approximately above the northern Snake Range footwall. This estimate of displacement has large uncertainties, but is reasonably consistent with the estimated slip from thermochronological cooling data (Miller et al., 1999).

Figure 11 shows a plausible tectonic model of the NSRFTS given the above assumptions. In this model, layer parallel thrusting along the Cpi-Cpm contact leads to a buckling instability in overlying units to the east. Units below the asymmetrical anticline-syncline pair and overlying structures are deflected downward due to the increased thickening of the overlying section. During progressive shortening, the detachment fold tightens to an apical angle of 40° and the axial plane rotates eastward towards a final subhorizontal westward dip of ~20°. In the late stages of folding, localized thrust faults parallel to the axial plane of the OPA form within Cpm and underlying Eocambrian strata that place Cpm atop Cpi/Ce. This final geometry of the NSRFTS system requires >7km of horizontal shortening and increases the effective structural thickness of the Lower-Upper Cambrian section by ≥ 3.5 km.
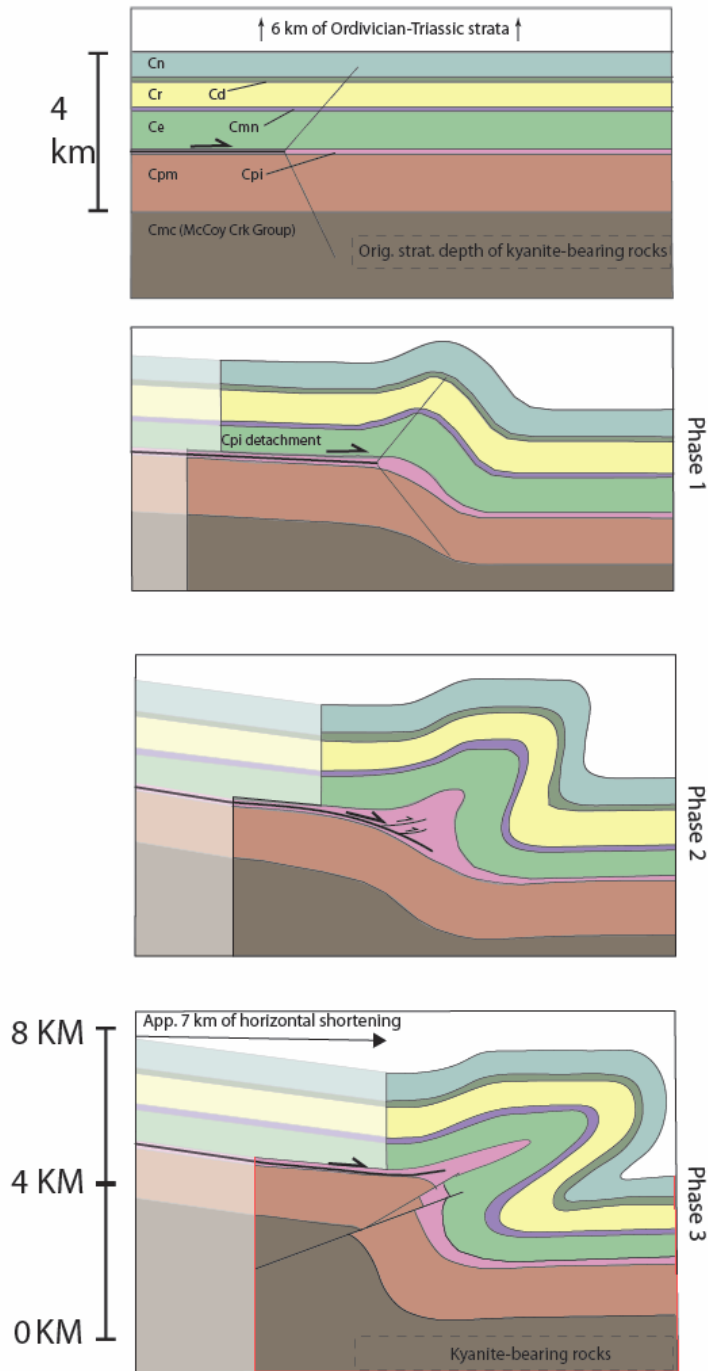
Figure 11: Plausible tectonic model of the Northern Snake Range Fold and Thrust System (NSRFTS). Layer-parallel thrusting along the Cpi detachment results in a buckling instability that evolves into an east-vergent anticline/syncline pair during progressive slip. Late stage thrust faulting of the ETS occurs within the hinge zone of OPA.

5.1. Potential Overlying Structures – The Western Utah fold and thrust belt (WUFTB)

Approximately 6 km of Ordovician-Triassic strata would have resided atop the Eocambrian-Upper Cambrian strata involved in the NSRFTS. Given the extent of shortening

accommodated by the NSRFTS, the overlying stratigraphy would have undergone

commensurate and/or greater shortening, resulting in additional burial. This shortening and

thickening at higher stratigraphic levels is well-exposed in the Confusion Range to the east.

The Confusion Range is a relatively low relief range in Western Utah that exposes

unmetamorphosed Ordivician-Triassic strata that have been folded into a series of NS-

trending upright to inclined anticlines/synclines and cut by small-displacement, east-directed

thrust faults (Hose, 1977; Hintze and Davis, 2003). Recent work (Yezerski and Greene,

2009; Matteri, 2010; Greene and Herring, 2013; Greene, 2014) has demonstrated that the

Confusion Range is part of an ~130 km long, NS-trending Mesozoic fold and thrust belt, they

named the Western Utah Fold and Thrust Belt (WUFTB), that accommodated ~10 km of

horizontal shortening within the Sevier hinterland. Greene (2014) presented a series of E-W

balanced cross sections of the Confusion Range that interpret the subsurface architecture and

style of crustal shortening. Specifically, these sections speculate that upper crustal shortening

is rooted in two subhorizontal detachment horizons along the Ordovician Eureka Quartzite

and the Upper Cambrian Orr formation (equivalent to the Dunderburg Shale). Above these

detachments, ~10 km of horizontal shortening is accommodated by ramp-flat thrust

relationships and east-vergent folding, whereas Eocambrian-Upper Cambrian strata directly

below these detachment horizons are assumed to be undeformed and subhorizontal (Figure

12). These sections illustrate localized thickening of the Ordovician-Triassic stratigraphy by

~75% (3.5-4.5km), but do not address how or where this shortening is accommodated at

deeper stratigraphic levels.

The NSRD projects eastward beneath the Confusion Range (Allmendinger et al., 1983) and must truncate and displace the proposed frontal ramp/flat of the WUFTB from its deeper root in the NSR footwall to the west. We suggest that the shortening structures of the Confusion Range root in part into the NSRFTS because, 1) The NSRFTS and the WUFTB both accommodated comparable amounts of shortening (7-10 km), 2) both are east-vergent with similar fold geometries, and 3) they appear to be broadly synchronous (Middle-Late Cretaceous) and distinctly pre-date Tertiary extension. Shortening in the deeper NSRFTS occurred during prograde dynamothermal metamorphism, such that there is far more distributed strain in the deeper part of the section. Because of this, we do not attempt to perfectly balance these sections because of the distributed nature of the strain.

Figure 12 is a plausible reconstruction of the Late Cretaceous northern Snake Range that integrates the NSRFTS and the WUFTB. By restoring ~30 km of top-east shear and brittle slip along the NSRD, the WUFTB would reside above and to the east of the NSRFTS. We suggest that ~7km of shortening was rooted in the Cpi detachment (rather than along the Dunderberg (Orr) detachment (Green, 2014)) and an additional 2-3 km of shortening was rooted in the stratigrphically higher Eureka Quartzite detachment. In our reconstruction, the frontal ramp and lateral flat structure of Greene (2014) is replaced by the OPA, essentially changing the frontal ramp-flat into a continuous thrust knappe. Shortening within the core of the OPRS likely resulted in tight folding, thrusting, and/or ductile thickening of overlying Upper Cambrian and Ordovician strata. The hinge zone of the OPRS/OPA gradually become more open at higher structural levels, resulting in the broad anticline-syncline pair preserved in the Upper Paleozoic strata of the Confusion Range. This section illustrates how the footwall units of the northern Snake Range were situated at the bottom of a major structural

trough at the end of late Cretaceous shortening, and were significantly deeper than correlative units to the east and west.

This reconstruction implies a minimum of 7 km of structural thickening to the local Cambrian-Triassic section. There are considerable uncertainties in this reconstruction and burial estimates, but the overall section is approximately balanced and satisfies the available surface geologic constraints. One major uncertainty is the original orientation of the OPRS axial plane. If it was significantly steeper at the end of Late Cretaceous shortening, e.g. 50° rather than the assumed 20°, the lower limb of the OPRS would have been buried several kilometers deeper. Perhaps the largest uncertainty in this reconstruction is our assumption that paleozoic strata were (sub)horizontal at the onset of shortening. If the stratigraphy at the northern Snake Range was significantly tilted/deformed prior to NSRFTS and WUFTB deformation, units in our reconstruction may have resided deeper than their original stratigraphic depths prior to Cretaceous shortening, and, therefore, our final burial estimate would increase.
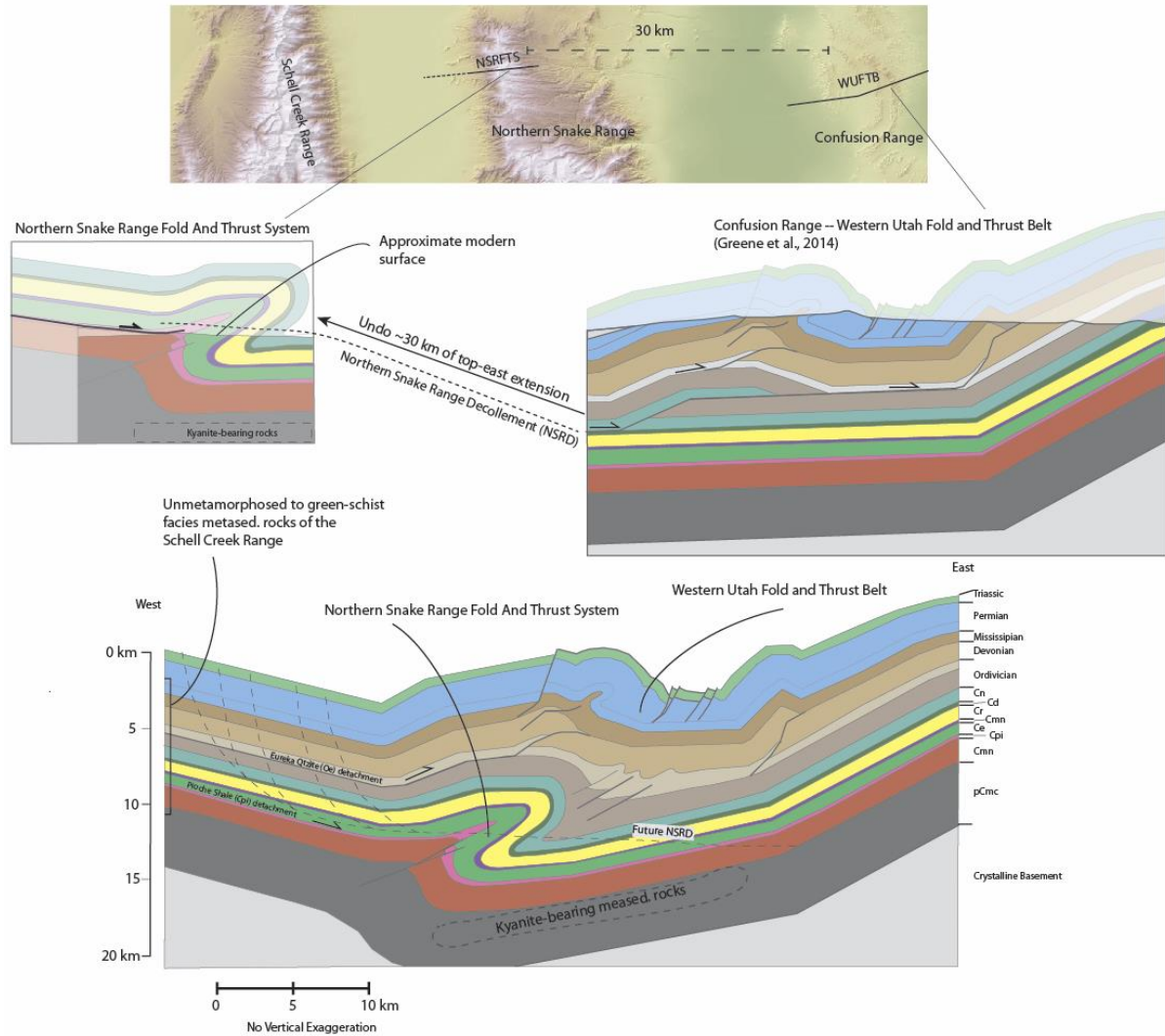
Figure 12: Late Cretaceous tectonic reconstruction of the northern Snake Range. Restoring ~30 km of slip along the NSRD returns shortening structures of the WUFTB exposed in the Confusion Range (Greene, 2014) above and east of the NSRFTS, resulting ~7km of structural thickening at the northern Snake Range.

6. DISCUSSION

This is the first study to describe in detail Mesozoic shortening structures in the northern

Snake Range and assign burial estimates to these structures, thereby providing a minimum

depth of footwall burial prior to Cenozoic extension. Moreover, this work provides the first

reasonably balanced reconstruction of the northern Snake Range metamorphic core complex that connects Mesozoic supracrustal deformation in the Confusion Range to its mid-crustal root in the northern Snake Range. Several aspects of this reconstruction and proposed shortening history merit further discussion.

6.1. Regional burial history of the Sevier Hinterland in Eastern Nevada

The $\geq$ 7 km of additional structural burial determined from our reconstruction indicate that Eocambrian McCoy Creek strata exposed in Hampton and Smith Creek with an original stratigraphic depth of 11-12 km reached burial depths of $\geq$ 18-19 km, well within the kyanite stability field. This burial estimate does not reach the 30±3 km depths postulated from thermobarometric analysis of the metamorphic assemblage (Lewis et al., 1999; Cooper et al., 2010a); however, both approaches have considerable and hard to quantify uncertainties. The peak P-T estimates from thermobarometry assume equilibrium conditions for all analyzed phases which is difficult to demonstrate in these polymetamorphic rocks – especially ones that have subsequently experienced pervasive high magnitude strain and considerable hydration and retrogression (e.g. Miller et al., 1983; Gébelin et al., 2011). Similarly, our reconstruction likely represents a minimum burial estimate and would increase if we have underestimated the original dip of the axial surface of the folds, the amount of thrust duplication, or the magnitude of subsequent extensional attenuation/thinning of units. Moreover, it is likely that additional unrecognized folds and thrust faults are present at stratigraphic/structural levels between what is now preserved at the Snake Range and the surface exposures of the Confusion Range, and these structures would further thicken the Paleozoic section. However, we are skeptical that the amount of excess thickening and burial

42

ever reached the 20+ kilometers implied from thermobarometric estimates because it is difficult to hide the structures that would be required to produce this extra localized burial.

The Deep Creek Range (DCR) and southern Snake Range (SSR) lie to the north and south, respectively, of the NSR and expose the same Eocambrian stratigraphy in the along-strike continuation of the footwall of the same major east-dipping detachment fault system, the Snake Range-Deep Creek detachment system (Miller et al., 1999). In contrast to the northern part of the NSR, the strata in these ranges are lower metamorphic grade (greenschist facies) and are locally upgraded to amphibolite facies (andalusite ± staurolite bearing assemblages), especially around Mesozoic plutons (Miller et al. 1988; Miller and Gans, 1989). These observations, in concert with the P-T estimates from within the NSR footwall itself (e.g. Miller et al., 1983; Lewis et al., 1999; Copper et al., 2010a), suggest that the locus of maximum burial was centered on the northern part of the NSR. The logical implication of this observation is that the amount of Late Cretaceous crustal shortening in this portion of Eastern Nevada must also have diminished to the north and south and that the structures responsible for burial must have been rather non-cylindrical. The exposed OPRS/OPA system is clearly non-cylindrical and, therefore, may be responsible for localized burial at the NSR; however, it is unclear how much of the non-cylindricity of the OPRS/OPA is due to rotation by younger mylonitic shearing. The non-cylindricity of the WUFTB is harder to definitively demonstrate, but it is certainly implied by the comparison of sections of the Confusion Range (Greene, 2014) with the section of the Burbank Hills to the south (e.g. McGrew, 1993). Just like Cenozoic extension is very heterogeneous across the Basin and Range (e.g. Gans and Miller, 1983; Wernicke, 1981), apparently the local magnitudes of crustal shortening and thickening in the Sevier hinterland were similarly heterogeneous.

6.2. Relationship of Mesozoic burial and subsequent extension/exhumation

The Eocambrian stratigraphy that was deeply buried in the northern Snake Range presently resides at the same crustal levels as equivalent strata to the north and south. This suggests that the greatest amount of post-Cretaceous exhumation is coincident with the area of greatest shortening and thickening. This observation supports the previous hypothesis of Coney and Harms (1984) and Spencer and Reynolds (1990) amongst others that the greatest amount of Cenozoic extension and exhumation may be in areas of greatest previous crustal thickening, wherein the gravitational potential energy associated with an over thickened crustal welt or root may be a primary driver for later extension. The northern Snake Range offers an exceptional opportunity to assess both the scale and timing of this potential feedback between localized crustal shortening and subsequent extension.

The present crustal thickness across the northern Basin and Range Province is a uniform ~30 km (Klemperer et al., 1986) indicating that any pre-existing crustal welts have been entirely eliminated by some combination of localized extension, lower crustal flow, or magmatic addition (e.g. Gans, 1987). In the northern Snake Range, much of the exhumation of the most deeply buried footwall rocks occurred in the Paleocene-Eocene, as evidenced by mica and K-feldspar ^{40}Ar/^{39}Ar and K/Ar ages of cooling through ~300-350°C (Lee and Sutter, 1991; Lee, 1995, Gans and Wong, 2014). Less clear is the mechanism of this earlier exhumation – was it buoyancy-driven mid-crustal diapirism combined with erosion, or extensional exhumation perhaps associated with the pre-Miocene extensional shearing and mylonitization recorded in footwall fabrics of the NSR? In any case, it appears that much of the removal of the lower crustal root occurred before Miocene brittle slip on the NSRD, as the footwall rocks on the

eastern flanks of the SSR, NSR, and DCR all resided at similar temperatures by the early Miocene (Gans and Wong, 2014).

These observations make a very compelling case for the importance of tectonic heredity in MMC evolution, where earlier (Mesozoic) crustal thickening magnitudes and architectures influenced both the magnitudes and geometry of subsequent Cenozoic extensional exhumation. An important corollary is that MMCs do not so much provide a window into what all of the middle crust of the Basin and Range province looked like, but instead provide a window into the root zones of earlier localized crustal thickening and lend insights into the processes responsible for their ultimate return to upper crustal levels.

7. CONCLUSIONS

New geologic mapping and structural investigation focused on Late Cretaceous shortening/burial structures in the northwestern footwall of the northern Snake Range MCC provide new insights into the style of deformation and magnitude of crustal thickening within the Sevier hinterland prior to Cenozoic extensional exhumation. From our field observations, we draw the following conclusions:

1. The OPRS and OPA are a km-scale east-vergent, non-cylindrical anticline/syncline pair that deform and regionally overturn middle-upper Cambrian strata.
2. East of the OPRS/OPA, older-on-younger relationships of the ETS require ≥1km of top-east slip, with significantly more layer parallel slip on the Cpi detachment.
3. The OPRS and ETA involve synmetamorphic fabrics/intrusions and are cross-cut by Eocene dikes.

4. The exposed portions of the NSRFTS accommodated ≥ 7km of horizontal shortening, and resulted in >3.5 km of crustal thickening.

5. The NSRFTS likely represents the mid-crustal root zone of the WUFTB exposed in the Confusion Range. Integration of the NSRFTS and WUFTB reconstructions result in 7-10 km of horizontal shortening and ≥ 7km of total crustal thickening.

6. The >7 km of structural burial from our reconstruction indicates that McCoy Creek Group strata were buried to a depth of >18-20 km, significantly deeper than their original stratigraphic depth and well within the kyanite field but well short of the 30±3 km depths determined from P-T studies.

7. The NSRFTS and WUFTB are non-cylindrical, with the deepest burial focused in the northern part of NSR and shallower burial to the north (Deep Creek Range) and south (southern Snake Range).

8. The area of highest magnitude extensional exhumation along the Snake Range-Deep Creek Range detachment coincides with the area of deepest Late Cretaceous burial, emphasizing the role of tectonic heredity in NSR MCC formation.

8. ACKNOWLEDGEMENTS

9. REFERENCES CITED

Allmendinger, R.W., Sharp, J.W., Von Tish, D., Serpa, L., Brown, L., Kaufman, S., Oliver, J. & Smith, R.B. (1983). Cenozoic and Mesozoic structure of the eastern Basin and Range province, Utah, from COCORP seismic-reflection data. *Geology*, *11*(9), 532-536.

Armstrong, R.L. (1972). Low-angle (denudation) faults, hinterland of the Sevier orogenic belt, eastern Nevada and western Utah. *Geological Society of America Bulletin*, *83*(6), 1729-1754.

Armstrong, R. L. (1982). Cordilleran metamorphic core complexes--From Arizona to southern Canada. *Annual review of earth and planetary sciences*, 10(1), 129-154.

Bartley, J.M. & Wernicke, B.P. (1984). The Snake Range decollement interpreted as a major extensional shear zone. *Tectonics*, *3*(6), 647-657.

Beyene, M.A. (2011). *Mesozoic burial, Mesozoic and Cenozoic exhumation of the Funeral Mountains core complex, Death Valley, southern California* (Doctoral Dissertation). Retrieved from *UNLV Theses, Dissertations, Professional Papers, and Capstones. Las Vegas, NV: UNLV.*

Burkhard, M. A. (1993). Calcite twins, their geometry, appearance and significance as stress-strain markers and indicators of tectonic regime: a review. *Journal of structural geology*, *15*(3-5), 351-368.

Chapman, J.B., Ducea, M.N., DeCelles, P.G. & Profeta, L. (2015). Tracking changes in crustal thickness during orogenic evolution with Sr/Y: An example from the North American Cordillera. *Geology*, *43*(10), 919-922.

Coney, P. J. (1980). Cordilleran metamorphic core complexes: An overview: Cordilleran metamorphic core complexes. *Geological Society of America Memoir*, 153, 7-31.

Coney, P.J. & Harms, T.A. (1984). Cordilleran metamorphic core complexes: Cenozoic extensional relics of Mesozoic compression. *Geology*, *12*(9), 550-554.

Cooper, F., Platt, J., Anczkiewicz, R., & Whitehouse, M. (2010a). Footwall dip of a core complex detachment fault: Thermobarometric constraints from the northern Snake Range (Basin and Range, USA). *Journal of Metamorphic Geology*, 28(9), 997-1020.

Cooper, F.J., Platt, J.P., Platzman, E.S., Grove, M.J. & Seward, G. (2010b). Opposing shear senses in a subdetachment mylonite zone: Implications for core complex mechanics. *Tectonics*, *29*(4).

Cubley, J.F. & Pattison, D.R. (2012). Metamorphism and deformation of the Grand Forks complex: implications for the exhumation history of the Shuswap core complex, southern British Columbia. *Canadian Journal of Earth Sciences*, *49*(11), 1329-1363.

DeCelles, P.G. (2004). Late Jurassic to Eocene evolution of the Cordilleran thrust belt and foreland basin system, western USA. *American Journal of Science*, *304*(2), 105-168.

DeCelles, P.G. & Coogan, J.C. (2006). Regional structure and kinematic history of the Sevier fold-and-thrust belt, central Utah. *Geological Society of America Bulletin*, *118*(7-8), 841-864.

Ferrill, D.A. (1991). Calcite twin widths and intensities as metamorphic indicators in natural low-temperature deformation of limestone. *Journal of Structural Geology*, *13*(6), 667-675.

Ferrill, D.A., Morris, A.P., Evans, M.A., Burkhard, M., Groshong Jr, R.H. & Onasch, C.M. (2004). Calcite twin morphology: a low-temperature deformation geothermometer. *Journal of structural Geology*, *26*(8), 1521-1529.

Gans, P. B. (1987). An open-system, two-layer crustal stretching model for the eastern Great Basin. *Tectonics*, *6*(1), 1-12.

Gans, P.B., Clark, D.H., Miller, E.L., Wright, J.E. & Sutter, J.F. (1986). Structural development of the Kern Mountains and northern Snake Range. In *Geol. Soc. Am. Abstr. Programs*, *18*(2), 108.

Gans, P. B. & Miller, E. L. (1983). Style of mid-Tertiary extension in east-central Nevada: Geological excursions in the overthrust belt and metamorphic core complexes of the Intermountain region. *Utah Geological and Mineral Survey Special Studies*, 59, 107-139.

Gans, P. B., Miller, E. L., Huggins, C. C., & Lee, J. (1999a). *Geologic map of the little horse canyon quadrangle, Nevada and Utah* (Field Studies Map 20). Reno, NV: Nevada Bureau of Mines and Geology

Gans, P. B., Miller, E. L., & Lee, J. (1999b). *Geologic Map of the Spring Mountain Quadrangle, Nevada and Utah* (Field Studies Map 18). Reno, NV: Nevada Bureau of Mines and Geology

Gans, P.B., Miller, E.L., McCarthy, J. & Ouldcott, M.L. (1985). Tertiary extensional faulting and evolving ductile-brittle transition zones in the northern Snake Range and vicinity: New insights from seismic data. *Geology*, *13*(3), 189-193.

Gans, P. B., & Wong, M. (2014). *Late Cretaceous Localized Crustal Thickening as a Primary Control on the 3-D Architecture and Exhumation Histories of Cordilleran Metamorphic Core Complexes*. In AGU Fall Meeting Abstracts.

Gébelin, A., Mulch, A., Teyssier, C., Heizler, M., Vennemann, T., & Seaton, N. C. (2011). Oligo-Miocene extensional tectonics and fluid flow across the Northern Snake Range detachment system, Nevada. *Tectonics*, *30*(5).

Greene, D.C. (2014). The Confusion Range, west-central Utah: Fold-thrust deformation and a western Utah thrust belt in the Sevier hinterland. *Geosphere*, *10*(1), 148-169.

Green, D.C. & Herring, D.M. (2013). *Structural architecture of the Confusion Range, west-central Utah: a sevier fold-thrust belt and frontier petroleum province*. Utah Geological Survey Open File Report (613).

Hallett, B.W. & Spear, F.S. (2013). The P–T history of anatectic pelites of the Northern East Humboldt Range, Nevada: Evidence for tectonic loading, decompression, and anatexis. *Journal of Petrology*, *55*(1), 3-36.

Hintze, L. F., & Davis, F. D. (2003). *Geology of Millard County, Utah.* (Vol. 133). Salt Lake City, UT: Utah Geological Survey.

Hodges, K. V., Snoke, A. W., & Hurlow, H. A. (1992). Thermal evolution of a portion of the Sevier hinterland: the northern Ruby Mountains-East Humboldt Range and Wood Hills, northeastern Nevada. *Tectonics*, *11*(1), 154-164.

Hoisch, T. D., Wells, M. L., & Hanson, L. M. (2002). Pressure-temperature paths from garnet-zoning: Evidence for multiple episodes of thrust burial in the hinterland of the Sevier orogenic belt. *American Mineralogist*, *87*(1), 115-131.

Hose, R.K. (1977). Structural geology of the Confusion Range, west-central Utah. *USGS professional paper* (971).

Hose, R. K., & Blake, M.C. (1976). Geology and mineral resources of White Pine County, Nevada, Part 1. *Nevada Bureau of Mines and Geology Bulletin* 85, 1-35.

Hose, R.K. & Whitebread, D.H. (1981). Structural evolution of the central Snake Range, Eastern Nevada during the mid-to-late Tertiary. In *Geol. Soc. Am. Abstr. Programs* (113), 62.

Howard, K. A. (1966). *Structure of the metamorphic rocks of the northern Ruby Mountains* (Doctoral dissertation). New Haven, CT: Yale University).

Howard, K.A. (1980). Metamorphic infrastructure in the northern Ruby Mountains, Nevada. *Geological Society of America Memoir*, 153, 335-347.

Howard, K., Kistler, R., Snoke, A., & Willden, R. (1979). *Geologic map of the Ruby Mountains, Nevada* (Map I-1136). Denver, Co: USGS

Huggins, C., & Wright, J. (1989). Superimposed Cretaceous and Tertiary metamorphism in the northern Snake Range. *Geological Society of America Abstracts with Programs1989*, 21, 95-96.

Klemperer, S. L., Hauge, T. A., Hauser, E. C., Oliver, J. E., & Potter, C. J. (1986). The Moho in the northern Basin and Range province, Nevada, along the COCORP 40 N seismic-reflection transect. *Geological Society of America Bulletin*, *97*(5), 603-618.

Lee, J. (1990). *Structural geology and 40Ar/39Ar thermochronology in the northern Snake Range metamorphic core complex, Nevada* (Doctoral dissertation). Palo Alto, Ca: Stanford University.

Lee, J. (1995). Rapid uplift and rotation of mylonitic rocks from beneath a detachment fault: Insights from potassium feldspar 40Ar/39Ar thermochronology, northern Snake Range, Nevada. *Tectonics*, *14*(1), 54-77.

Lee, J., Blackburn, T., & Johnston, S. (2017). Timing of mid-crustal ductile extension in the northern Snake Range metamorphic core complex, Nevada: Evidence from U/Pb zircon ages: *Geosphere*, 13(2).

Lee, J., Gans, P. B., & Miller, E. L. (1999a). *Geologic map of the Third Butte East Quadrangle, Nevada* (Field Map 16). Reno, NV: Nevada Bureau of Mines and Geology.

Lee, J., Gans, P. B., & Miller, E. L. (1999b). *Geologic map of the Mormon Jack Pass Quadrangle, Nevada* (Field Studies Map, 19). Reno, NV: Nevada Bureau of Mines and Geology.

Lee, J., Miller, E. L., Gans, P. B., & Huggins, C. C. (1999c). *Geologic map of the Mount Moriah quadrangle, Nevada* (Field Studies Map, 19). Reno, NV: Nevada Bureau of Mines and Geology.

Lee, J., Miller, E. L., & Sutter, J. F. (1987). Ductile strain and metamorphism in an extensional tectonic setting: A case study from the northern Snake Range, Nevada, USA. *Geological Society, London, Special Publications*, *28*(1), 267-298.

Lee, J., & Sutter, J. F. (1991). Incremental 40Ar/39Ar thermochronology of mylonitic rocks from the northern Snake Range, Nevada. *Tectonics*, *10*(1), 77-100.

Lewis, C. J., Wernicke, B. P., Selverstone, J., & Bartley, J. M. (1999). Deep burial of the footwall of the northern Snake Range decollement, Nevada. *Geological Society of America Bulletin*, 111(1), 39-51.

Matteri, M. (2010). New balanced and retrodeformable cross section of the northern Confusion Range, west-central Utah indicates an east-vergent fold-and-thrust belt of Sevier age. In *2010 GSA Denver Annual Meeting*.

McGrew, A. J. (1993). The origin and evolution of the southern Snake Range décollement, east central Nevada. *Tectonics*, *12*(1), 21-34.

McGrew, A. J., Peters, M. T., & Wright, J. E. (2000). Thermobarometric constraints on the tectonothermal evolution of the East Humboldt Range metamorphic core complex, Nevada. *Geological Society of America Bulletin*, 112(1), 45-60.

Miller, C. F., & Bradfish, L. J. (1980). An inner Cordilleran belt of muscovite-bearing plutons. *Geology*, *8*(9), 412-416.

Miller, D. M. (1980). Structural geology of the northern Albion Mountains. *Geol Soc Am Mem*, 153, 399-423.

Miller, D. M. (1983). Allochthonous quartzite sequence in the Albion Mountains, Idaho, and proposed Proterozoic Z and Cambrian correlatives in the Pilot Range, Utah and Nevada. In Miller, D.A., Todd, V.R., and Howard, K.A. (Eds.), *Tectonic and stratigraphic studies in the eastern Great Basin* (Vol. 157, pp. 191-213). Denver, Co: Geological Society of America.

Miller, E. L., Gans, P. B., & Garing, J. (1983). The Snake Range decollement: An exhumed mid-Tertiary ductile-brittle transition. *Tectonics, 2*(3), 239-263.

Miller, E.L. & Gans, P.B. (1989). Cretaceous crustal structure and metamorphism in the hinterland of the Sevier thrust belt, western US Cordillera. *Geology*, *17*(1), 59-62.

Miller, E. L., & Gans, P. B. (1999a). *Geologic map of the Cove Quadrangle, Nevada* (Field Studies Map 22). Reno, NV: Nevada Bureau of Mines and Geology

Miller, E. L., Gans, P. B., Grier, S. P., Huggins, C. C., & Lee, J. (1999b). Geologic map of the Old Mans Canyon quadrangle, *Nevada* (Field Studies Map 21). Reno, NV: Nevada Bureau of Mines and Geology

Miller, E.L., Dumitru, T.A., Brown, R.W. & Gans, P.B. (1999). Rapid Miocene slip on the Snake Range–Deep Creek range fault system, east-central Nevada. *Geological Society of America Bulletin*, *111*(6), 886-905.

Misch, P. (1960). Regional structural reconnaissance in central-northeast Nevada and some adjacent areas: Observations and interpretations. In *Guidebook to the geology of east-central Nevada* (17-42). Intermtn. Assoc. Petroleum Geologists and Utah Geol. Soc.

Nelson, R.B. (1966). Structural development of northernmost Snake Range, Kern Mountains, and Deep Creek Range, Nevada and Utah. *AAPG Bulletin*, *50*(5), 921-951.

Norlander, B.H., Whitney, D.L., Teyssier, C. & Vanderhaeghe, O. (2002). Partial melting and decompression of the Thor-Odin dome, Shuswap metamorphic core complex, Canadian Cordillera. *Lithos*, *61*(3-4), 103-125.

Rodgers, D.W. (1987). *Thermal and structural evolution of the southern Deep Creek Range, west-central Utah* (Doctoral Dissertation). Palo Alto, Ca: Stanford University.

Snoke, A. W. (1980). Transition from infrastructure to suprastructure in the northern Ruby Mountains, Nevada: Cordilleran metamorphic core complexes. *Geological Society of America Memoir*, 153, 287-333.

Stipp, M., Stünitz, H., Heilbronner, R. & Schmid, S.M. (2002). Dynamic recrystallization of quartz: correlation between natural and experimental conditions. *Geological Society, London, Special Publications*, *200*(1), 171-190.

Wells, M.L., Hoisch, T.D., Beyene, M. & Vervoort, J.D. (2011). Jurassic thrust burial in the Funeral Mountains of the Sevier retroarc: Linking PT paths and Lu-Hf garnet geochronology. In *AGU Fall Meeting Abstracts*.

Wells, M.L., Hoisch, T.D., Cruz-Uribe, A.M. & Vervoort, J.D. (2012). Geodynamics of synconvergent extension and tectonic mode switching: Constraints from the Sevier-Laramide orogen. *Tectonics*, *31*(1).

Womer, J.B. 2017. *Late Mesozoic Shortening Structures in the Western Portion of the Northern Snake Range Metamorphic Core Complex, White Pine County, NV* (Doctoral dissertation, UC Santa Barbara).

Yezerski, D., & Greene, D. C. (2009). *New Structural Interpretation of the Central Confusion Range, Western Utah, Based On Balanced Cross Sections*. In AGU Fall Meeting Abstracts.

Young, J.C. (1960). Structure and stratigraphy in the north central Schell Creek Range. In *Guidebook to the geology of east-central Nevada* (158-173). Intermtn. Assoc. Petroleum Geologists and Utah Geol. Soc.

CHAPTER 2

USING MULTIPLE DIFFUSION DOMAIN TEMPERATURE-TIME

MODELING TO INTERPRET POTASSIUM FELDSPAR ^{40}Ar/^{39}Ar AGE

SPECTRA: A CASE STUDY AT THE NORTHERN SNAKE RANGE AND

SURROUNDING ENVIRONS

A.J. WROBEL[1]

1. ABSTRACT

Multiple-diffusion domain (MDD) modeling of a large (n=28) geologically well-constrained

K-feldspar ^{40}Ar/^{39}Ar thermochronology dataset from the Northern Snake Range, NV and

surrounding environs provide new insights into MDD parameter space and the consistency of

MDD cooling histories. We find that diffusion domain size distributions (i.e. domain size and

volume fraction of total Ar) vary considerably throughout the dataset, with domain sizes

spanning 4-5 orders of magnitude within a single sample (from $\rho \sim 0.02$ to $\rho \sim 200$) and that

the distribution of Ar among domains is dependent on grain-size – with fine grained samples

(<300μm) holding ~45% of the total Ar within small domains ($\rho < 2$) and coarser grained

samples (>300 μm) holding ~20% of the total Ar within small domains. Regardless of the

domain size/volume distribution, all K-feldspar samples require ≥8 diffusion domains to

adequately model the experimental results. The activation energies (E_a) of Ar diffusion in K-

feldspar range from 42-54 kcal/mol with a mean (±σ) of 48.4 ± 1.6 kcal/mol. The MDD

cooling history dataset is more internally consistent if all cooling histories are calculated

using an E_a that falls within 1 sigma of the mean E_a of the data set, suggesting that much of

the observed variation in E_a is likely due to analytical error and not natural variation. We use

these results to construct an internally consistent dataset of MDD cooling histories, and use

this data set to explore quantitative relationships between the shape of an age spectrum and

its MDD cooling history. We find quantifiable correlations between a) the slope of an age

spectrum and the MDD cooling rate, b) the initial slope of an age spectrum and the minimum

cooling temperature recorded by that sample, and c) the cumulative fraction of ^{39}Ar released

during a step heating experiment and the effective geologic cooling temperature of the

sample – a curve we term the temperature spectrum. These relationships between the age

spectrum and MDD derived cooling history are sufficiently systematic and quantifiable that

we develop a schema for extracting T-t histories directly from K-Feldspar age spectra. This

method, named the spectrum-derived method, essentially eliminates cooling history error due

to poor MDD model fit, and thus may be a more reliable method for constructing T-t cooling

histories for geologic datasets.

2. INTRODUCTION

^{40}Ar/^{39}Ar thermochronology of potassium feldspar (K-feldspar) via multiple diffusion

domain (MDD) modeling is a powerful tool for describing the cooling history of igneous and

metamorphic rocks. MDD theory states that radiogenic argon in K-feldspar is retained in, and

ultimately diffused from, a distribution of different sized domains, each with a unique closure

temperature. If specific kinematic and domain parameters are satisfied, Ar diffusion data

from a step heating experiment in concert with the associated age spectrum can be inverted to

reconstruct a continuous geologic cooling history from ~350°C to ~150°C. Thus, MDD

modeling has the capability of determining the timing and rate of cooling through a critical

temperature range associated with plutonism, contact/regional metamorphism, uplift, and/or exhumation (McDougall and Harrison, 1988). Specifically, K-feldspar offers the opportunity to assess thermal histories of rocks as they moved from mid- to upper-crustal levels and bridges a critical thermochronology gap between higher closure temperature systems (e.g., U-Pb titanite, monazite, zircon; Ar^{40}/Ar^{39} –mica, hornblende) and low closure temperature systems (e.g., fission track-zircon and apatite; U/Th-He- apatite, zircon, titanite) (McDougall and Harrison, 1988; Lovera et al., 1989,1991; McDannell et al., 2019).

K-feldspar MDD theory has been debated since its introduction in the late 1980s-early 1990s, with attention focused on a) the physical characteristics and/or existence of K-feldspar Ar diffusion domains, and b) the assumption that laboratory step-heating experiments sufficiently mimic Ar diffusion/retention in nature. The physical nature of Ar diffusion domains remain poorly understood. It has been proposed that the domains are controlled primarily by microfractures, fast-diffusion pathways, subgrains, or perthite boundaries within K-feldspar grains (i.e. Parsons et al., 1988; Lee, 1995; Burgess et al., 1992), rather than complex structural domains dominated by volume diffusion (i.e., Lovera et al., 1989, 1991; Reddy et al., 2001; Cassata and Renne, 2013). Others contend that laboratory step-heating experiments do not accurately mimic K-feldspar Ar diffusion in nature, citing the important role of microtextures and fluid-controlled isotope transport during geologic cooling (Parsons et al., 1999; Villa, 2014) – factors that can't be replicated during step-heating experiments and are not considered by MDD models. However, despite these contentious assumptions and uncertainties, K-feldspar MDD thermal models repeatedly yield regionally-consistent temperature-time histories that agree with other thermochronometers collected from the same sample and/or region (Batt et al., 2004; Benowitz et al., 2011; McDannell et al., 2019). While

the continued study of MDD and competing theories will undoubtedly refine the *absolute* temperatures obtained by K-feldspar ^{40}Ar/^{39}Ar thermochronology, we contend that MDD modeling is a robust method for creating well-constrained, geologically reasonable *differential* cooling histories that allow for the comparison of cooling histories from neighboring samples.

MDD modeling is a time-consuming analytical process, and, as a result, most studies only present a handful (<5) of K-feldspar MDD cooling histories for a given study and apply these cooling histories across large geologic terranes (10s-100s of km). With such widely spaced samples, few studies can critically assess the internal consistency of a dataset, thus leading to large uncertainties in geologic interpretations. Here, we calculate MDD cooling histories from a large, high spatial density dataset of 28 samples from the northern Snake Range (NSR) metamorphic core complex and environs – samples that experienced a wide range of cooling histories, including a) rapid cooling through most of the K-feldspar closure temperature range, b) episodic rapid cooling, and c) prolonged slow cooling. From this dataset, we present new insights into MDD parameter space, introduce methodologies for optimizing the internal consistency of differential MDD cooling histories, and provide a new schema for producing approximate K-feldspar MDD cooling histories directly from the experimental age spectrum.

We divide this paper into two parts. Part 1 assesses the natural variability in domain and diffusion parameters in the modeled dataset and discusses the best-practices to obtain internally consistent differential MDD cooling histories. Part 2 uses this large dataset of well-constrained differential cooling histories to develop quantitative relationships between geometric attributes of an age spectrum (e.g., the local slope in the age gradient, inflection

57

points, the cumulative fraction of the gas released, low and high-temperature intercepts) and

its corresponding MDD model temperatures and cooling rates. We then show how these

systematic relationships between an experimental age spectrum and its model cooling history

can be used to generate semi-quantitative cooling histories directly from the age spectrum,

bypassing the time consuming process of MDD modeling

This study sets the stage for a forthcoming

companion paper with Phillip Gans that uses the

approaches discussed here applied to an even

larger $^{40}Ar/^{39}Ar$ K-feldspar and mica dataset to

unravel in unprecedented detail the thermal

architecture, geometric evolution, and

exhumation and cooling history of the Snake

Range MCC and environs.

3. MDD MODELING: THEORY AND

  PARAMETERS

Since the advent of K-Ar geochronology,

researchers noted that K-feldspar ages are often

younger than coexisting mica and ampbibole, and that

argon diffusion from K-feldspar grains yielded

Arrhenius plots that significantly differ from those of

other argon-bearing mineral phases (e.g., Dalrymple

Figure 1:Example Arrhenius plots of Ar diffusion from Hornblende (A; modified from Harrison, 1985) and from K-feldspar (B; this study). The linear Arrhenius array shown in A indicates diffusion from a single diffusion domain. The K-feldspar Arrhenius plot shown in B breaks from linearity after the first few temperature steps.

and Lanphere, 1979; McDougall and Harrison, 1988) (Fig.1). Argon diffusion experiments

from muscovite, biotite, and amphibole often produces linear Arrhenius plots over a
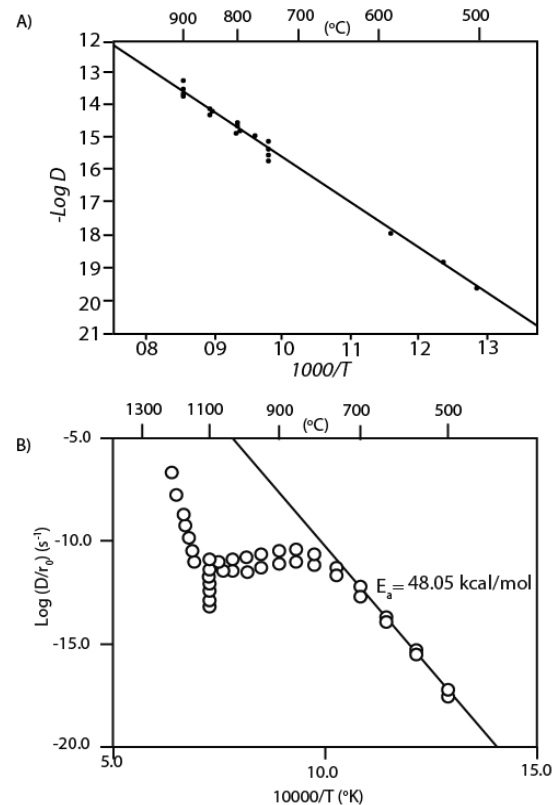
significant portion of the heating experiment, implying that radiogenic argon is retained in fairly homogenous diffusion domains (figure 1a). Argon diffusion from K-feldspar grains, however, produces Arrhenius plots that break from linearity after the first few temperature steps (Figure 1b), implying that diffusion kinematics/mechanics in K-feldspar are fundamentally different than other argon-bearing minerals.

A major advance in K-feldspar $^{40}Ar/^{39}Ar$ thermochronology came with a better understanding of volume diffusion and application of Dodson's (1973) closure theory to interpreting $^{40}Ar/^{39}Ar$ incremental heating age spectra. Harrison (1983) and Harrison and Be (1983) showed that variations in radiogenic Ar released during the initial low-temperatures steps of a step-heating experiment (corresponding to the linear portion of the Kspar Arrhenius plot) could be effectively modeled by volume diffusion, and that the different $^{40}Ar/^{39}Ar$ ages calculated for successive temperature steps could be used to assess the geologic cooling history of a sample. However, this modeling approach could only be applied to the linear low-T portion of the K-feldspar Arrhenius plot (Harrison et al., 1986; Heizler et al., 1988), with the non-linear high-temperature portion of the age spectrum inferred to represent structural breakdown or incongruent melting of the sample.

Zeitler (1987) proposed that the non-linearity of Arrhenius plots from K-feldspar step-heating experiments could be qualitatively explained by volume diffusion from a distribution of diffusion domain sizes within a single sample. In this theory, the break in slope of the K-feldspar Arrhenius plot represents simultaneous degassing of diffusion domains of different size and volume fractions (Fig.2). This theory was subsequently quantified by Lovera et al. (1989; 1991), who showed that carefully constructed cyclic step heating experiments that adequately constrain the diffusion parameters of a sample produce Arrhenius plot that can be

59

modeled by volume diffusion from a finite number of different sized diffusion domains (i.e., multiple diffusion domains (MDD)). Here, we briefly discuss the MDD theory equations to model K-feldspar Arrhenius plots and age spectra. For a full derivation of the MDD equations, see Lovera et al. (1989).
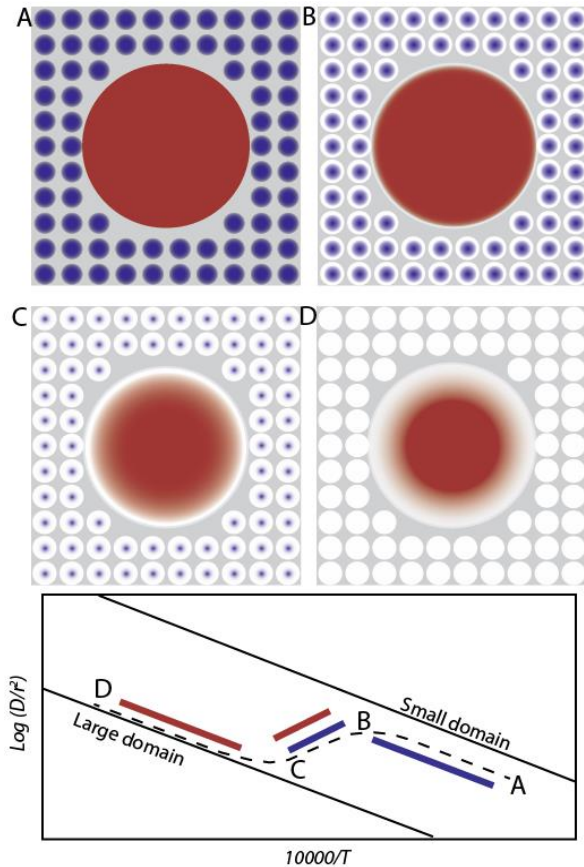

Figure 2: Illustration of simultaneous argon diffusion from 2 domains of different size and volume and the resulting shape of the Arrhenius plot (modified from Harrison et al., 2014). From diagram A to B, argon is primarily diffusing from small homogenous diffusion domains, yielding a linear Arrhenius plot. From B to C, argon is diffusing equally from small and large domains, resulting in a break in slope in the Arrhenius plot. Between C and D, argon diffusion is dominated by the large domain, resulting in another linear segment of the Arrhenius plot.

3.1. Equations for Ar diffusion from a single domain

MDD theory (Lovera et al., 1989) is derived from Dodson's (1973, 1979) closure theory that assumes Ar degassing in a step-heating experiment and Ar retention in nature is governed by thermally-activated volume diffusion and is accurately modeled by the Arrhenius equation

$$D = D_o e^{(-\frac{E_a}{RT})} \ (1)$$

60

where D is the diffusion coefficient, D_0 is the diffusion coefficient of the initial gas release, E_a is the activation energy of diffusion, R is the gas constant, and T is temperature (K). Expansion of Equation 1 to include the effective diffusion length scale (r) and the rearranging the variables yields

$$\frac{lnD}{r^2} = \frac{lnD_0}{r^2} + \frac{E_a}{R}\left(\frac{1}{T}\right) \quad (2)$$

and can be graphically represented as a line with a slope proportional to E_a and a y-intercept related to D_o (Figure 3a, curve 1). Dodson (1973, 1979) further showed that the closure temperature T_c of a single domain is expressed by

$$T_c = \frac{E_a}{Rln(\frac{A\tau D_0}{r^2})} \quad (3)$$

where T_c is the closure temperature of a domain, A is a constant for a given domain shape (slab, sphere, or cylinder), and τ is a function of the assumed cooling rate expressed by

$$\tau = \frac{RT_c}{E(\frac{dT}{dt})} \quad (4)$$

with units of time. Equation 3 is solved iteratively by inputting an estimate of T_c and letting the solution converge over several iterations.

A cooling rate-normalized age spectrum, with axes of Δage/ τ vs. cum% ^{39}Ar release ($^{39}f_m$), for Ar diffusion from a single domain is modeled by

$$\frac{\Delta age}{\tau} = \frac{-2\sum_{n=1}^{\infty} ln(a_n/a_1)e^{-\alpha_n^2\zeta_m}}{\sum_{n=1}^{\infty} e^{-\alpha_n^2\varphi_m}} \quad (5)$$

and

$$^{39}f_m = 1 - \beta \sum_{n=1}^{\infty} \alpha_n^{-2} e^{-\alpha_n^2\zeta_m} \quad (6)$$

61

where $\frac{\Delta age}{\tau}$ is the age difference relative to the age of the last argon extracted in units of τ,

a_n depends on the geometry of the grain ($a_n = \pi n$ for spheres and $a_n = (n-1)(\frac{\pi}{2})$ for slabs),

β is a constant dependent on the assumed domain geometry ($\beta = 6$ for spheres, $\beta = 2$ for slabs), and ζ_m is found by integrating the expression

$$\zeta_{(t)} = \int_0^t \frac{D(t')}{r^2}\, dt' \quad (7)$$

From t = 0 to t_m.

3.2. Expansion of Dodson's closure theory to account for multiple diffusion domains:

Lovera et al. (1989) expanded the Dodson closure theory to account for a distribution of diffusion domains of different sizes and volume fraction of total [39]Ar released. The Arrhenius plot for multiple diffusion domains is modeled by

$$\Delta\zeta_m = (D_o/\bar{R}^2)e^{(-\frac{E_a}{RT})}\Delta t_m \quad (8)$$

where $\Delta\zeta_m$ is related to the diffusivity at a given incremental temperature step, and

Diffusion Domain Distribution

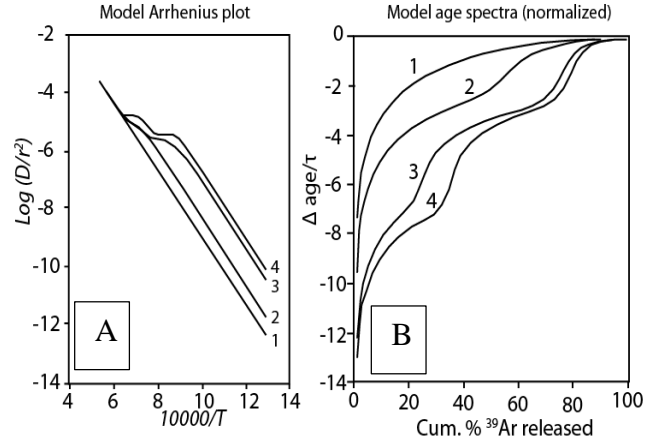| Curve	Domain 1 Size(1)	Volume(1)	Domain 2 Size(2)	Volume(2)	Domain 3 Size(3)	Volume(3)
1	1.00	1.00	—	—	—	—
2	0.2	0.32	1.00	0.68	—	—
3	0.02	0.154	0.2	0.46	1.00	0.386
4	0.02	0.267	0.2	0.40	1.00	0.333

Figure 3: Model Arrhenius plots (A) and model cooling rate-normalized age spectra (B; $\tau = 7$ Ma) of argon diffusion from different domain distributions shown in the table (Mod. from Lovera et al., 1989). Curve(s) 1 represents model Arrhenius and age spectrum solutions for a single diffusion domain. Curves 2-4 represent model Arrhenius and age spectra for a distribution of 2-3 domains of different size and volume fraction shown in the table. Note that diffusion from a single domain results in a linear Arrhenius plot and a concave-down model age spectrum, while diffusion from a distribution of domains of different sizes and volume fractions yield Arrhenius plots that break from linearity and produce model age spectra with multiple inflection points.

$\bar{R}$ is the effective domain size that incorporates both domain size (ρ) and volume fraction (φ), expressed by

$$\bar{R}(\rho_j, \phi_j) = \left\{ \sum_{j=1}^{S} \frac{\phi_j}{\rho_j} \right\}^{-1}. \quad (9)$$

If we accept that a K-feldspar sample with multiple diffusion domains behaves, for the first gas released, like a uniform diffusion domain, the effective diffusion length of the of the initial gas released, r_o, can be expressed by

$$r_o = r(\rho_j, \phi_j) = \left\{ \sum_{j=1}^{S} \frac{\phi_j}{\rho_j} \right\}^{-1} \quad (10)$$

And the diffusion length scale subsequent domains can be expressed by,

$$r = \left\{ \sum_{j=2}^{S} \frac{\phi_j}{\rho_j} \right\}^{-1} \quad (11).$$

The cooling rate normalized age spectrum for multiple diffusion domains is modeled by

$$\frac{\Delta age}{\tau} = 2 \sum_{j=1}^{S} \phi_j \rho_j^{-2} \sum_{n=1}^{\infty} \ln(a_n \rho_s / a_1 \rho_j) e^{\left(-\frac{a_n^2 \zeta m}{\rho_j^2}\right)} \cdot \left\{ \sum_{j=1}^{S} e^{\left(-\frac{a_n^2 \zeta m}{\rho_j^2}\right)} \right\}^{-1} \quad (12)$$

and

$$^{39}f_m = \sum_{j=1}^{S} \phi_j \left\{ 1 - \beta \sum_{n=1}^{\infty} \alpha_n^{-2} e^{-\frac{a_n^2 \zeta m}{\rho_j^2}} \right\} \quad (13)$$

where S is the number total number of domains.

Model Arrhenius plots for multiple diffusion domains modeled by Equation 7 break from linearity (Fig. 3a, curve 2-4), and the model normalized age spectra from Equation 12 and 13 have multiple inflection points (Fig. 3b, curve 2-4). The shape of these curves more closely

resemble the form of experimental K-feldspar Arrhenius plots and age spectra and, in theory, if the correct (or acceptable) distribution of domain sizes and volume fractions are assigned (see the following section), a model age spectrum and Arrhenius plot can be produced that replicates experimental results.

3.3. Kinematic and domain parameters required for MDD modeling

Equation 7, 12, and 13 – defining the shape of a model MDD Arrhenius plot and age spectrum – are a function of the diffusion kinematic parameters E_a and D_o and the domain distribution parameters of domain shape (α), number of domains (S), relative domain size (ρ), and volume fraction of each domain (φ). These parameters are assigned by the user to invert the experimental results and calculate a model Arrhenius plot, age spectrum, and cooling history. The test of the plausibility of the chosen domain distribution parameters is how well the model Arrhenius plot and age spectrum match that obtained experimentally from the sample.

The kinematic parameters E_a and D_0 are determined by fitting a least-squares regression to the first several steps of the experimental Arrhenius data. The slope of the regression is a function of E_a, and the y-intercept is a function of D_o/r^2 (Figure 4b). Arrhenius data from the initial temperature step is commonly omitted from this regression if it does not fit the trend of the subsequent data. With E_a and D_o determined, domain distribution parameters S, ρ, and φ (Fig 4a) are assigned to create a synthetic Arrhenius plot that best fits the experimental Arrhenius data (Fig 4b). The assignment of these parameters is an iterative process, with considerable trial and error required to choose a set of domain parameters that reproduce the observed experimental results (Figure 7).

64

To streamline the assignment of domain parameter, diffusion data is often shown in a log(r/r_o) v. cumulative fraction [39]Ar release plot, referred to hereafter as a log(r/r_o), rather than an Arrhenius plot (Lovera et al., 1991; Richter et al., 1991), where

$$log(r/r_o) \ = \ \tfrac{1}{2} \, (log D/r_o^2 - log \, D/r^2) \ (14)$$

in which r_0 is the diffusion length scale of the first gas released, and r is the apparent diffusion length scale at a given temperature step. For the first ~10% of Ar release, the ratio $r/r_0 = $ ~1, therefore $log(r/ro) \ = $ ~0. With continued gas extraction, the smallest diffusion domains are exhausted and diffusion is dominated by larger domains, thus the r/r_0 and log(r/r_o) values increase as cumulative Ar release increases (Fig 4c). A log(r/r_o) plot provides a more intuitive graphical space for assigning domain parameters, with the number of inflection points of the log(r/r_o) curve representing an estimate of the number of diffusion domains (S), the x-axis for each inflection being a function of relative domain size (ρ), and the x-axis value relating to volume fraction (φ) (Fig. 4c).The variables S, ρ, and ϕ are tweaked in an iterative process until the synthetic log(r/r_o)plot closely matches the experimental log(r/r_o) plot (Fig 4c). With diffusion and domain parameters that satisfactorily fit the experimental Arrhenius plot and/or log(r/r_o) plot, results from a step heating experiment are inverted by iterating equations 3, 12, and 13 to produce a model age spectrum and a continuous geologic cooling history that spans the closure temperatures of the assigned domains (~350-150°C).

The relative domain size (ρ), is derived from the ratio r/r_0, and is thus dimensionless (See Lovera et al., 1991 – Appendix A). Though the physical nature of diffusion domains are poorly understood, several studies have explored the apparent size range of diffusion

domains (Lovera et al., 1993; Fitzgerald and Harrison., 1992; Harrison et al., 1991). By conducting step-heating experiments on progressively finer aggregates, Lovera et al. (1993) found that the largest domains were unrecognizable for aggregates <100 μm, suggesting that the largest domains have effective radii of ~100 μm. Harrison et al. (1991) found that the smallest diffusion domains are ~450 times smaller than the largest domains, suggesting that the scale of the smallest domains is ~0.1 μm. The assigned dimensionless relative domain size (ρ) required for MDD modeling does not represent a physical distance/size of a theorized domain within a sample, however the range of ρ values, often over three orders-of-magnitude, does provide information regarding the relative proportions of small domains (~<1 μm), moderate-sized domains (~1-10 μm), and large domains (~10-100 μm).

3.4. Special considerations for diffusion and domain parameters

MDD parameter solutions that satisfy experimental results are non-unique. This raises the question: do different parameter solutions for the same experiment yield consistent cooling histories? Lovera et al., 1991 showed that variations in S, ρ, and φ for the same sample yield indistinguishable model age spectra and cooling histories. However, Lovera et al. (1997) showed that variation in the assigned activation energy (E_a) and diffusion coefficient (D_o) shift the calculated closure temperature of a sample by as much as 10˚C/kcal/mol, thus altering the calculated cooling history. Therefore, the confident comparison of multiple cooling histories from various geologic locales requires a careful examination of each sample's model parameters to ensure that similarities or differences in model cooling histories are geologically meaningful and not solely the result of the assigned parameters.
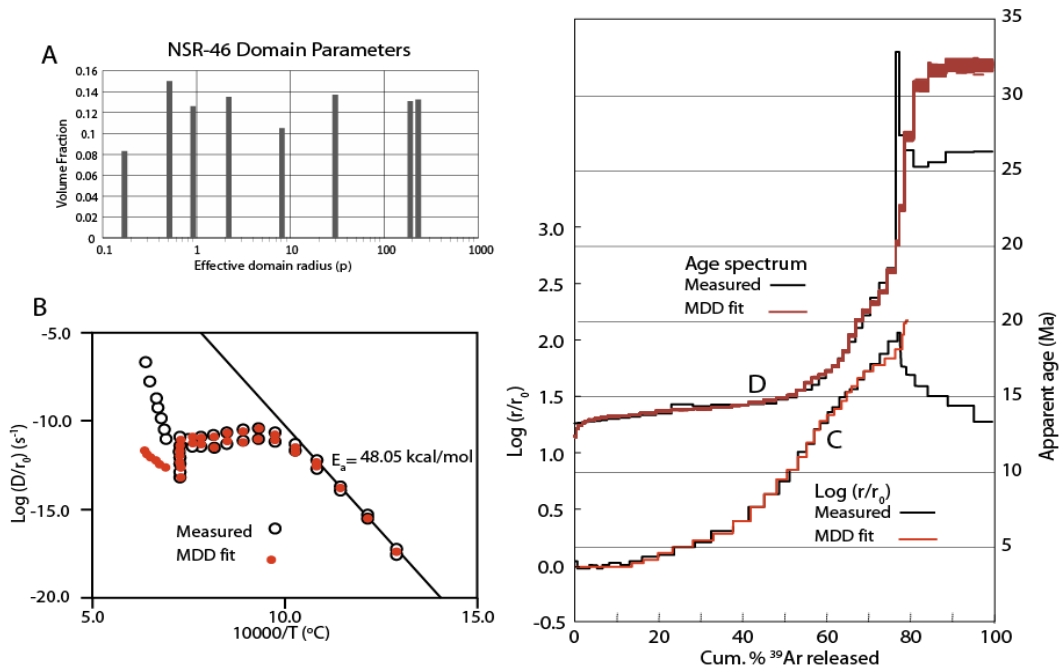
Figure 4: Example of MDD fits to the experimental Arrhenius and log(r/r_o) plot or sample NSR-46. The assigned domain parameters (A) result in synthetic Arrhenius (B) and log(r/r_o) (C) plots that satisfactorily match the measured plots. These parameters yield a MDD model age spectrum that closely matches the experimental age spectrum (D). Note, however, that portions of the synthetic MDD log(r/r_o) curve deviate from the measured log(r/r_o) curve between ~50 and 80% cumulative [39]Ar released, and, as a result, the synthetic MDD age spectrum similarly deviates from the measured age spectrum between the same % cumulative [39]Ar released.

4.   A CRITICAL ASSESSMENT OF MDD THEORY AND PRACTICE AT THE

NORTHERN SNAKE RANGE METAMORPHIC CORE COMPLEX

Prior to this investigation, Gans completed a detailed [40]Ar/[39]Ar thermochronological

investigation of metamorphic rocks in the northern Snake Range MMC and adjacent ranges

(Gans and Wong, 2014, Gans et al., in prep). This work included more than 50 detailed

incremental heating experiments on K-feldspar and mica separates from a dense array of

samples spanning the E-W and N-S extent of the footwall, along with a few complementary

samples from similar stratigraphic levels in adjacent ranges. This work shows that following

Late Cretaceous burial and greenschist- to amphibolite-facies metamorphism (e.g., Miller et

al., 1988), the metamorphic rocks in these ranges were partially exhumed and cooled during the Paleogene by normal faulting and ESE-directed mylonitic shearing, and after ~15 Ma of quiescence, were brought to near-surface levels beginning at ~18-20 Ma by rapid E-directed slip along the Miocene Snake Range detachment and other range bounding faults. This argon thermochronology data set from the Northern Snake Range consists of ages that increase monotonically westward despite close spacing, age differences of only hundreds of ka, and spectra shapes that vary systematically according to stratigraphic and structural position. The full tectonic implications of this dataset, including the constraints it places on the thermal architecture of the footwall, magnitude and timing of slip, and amount of footwall rotation, for the northern Snake Range MMC are explored in the companion paper (Gans et al., in prep.). Here, we analyze a subset of this dense and internally consistent sample array to derive quantitative temperature-time histories, and, in the process, explore the limitations and best practices of MDD modeling and develop new methods for determining T-t histories directly from K-feldspar spectra.

In this study, we analyzed and MDD modeled 28 K-feldspar samples from the northern Snake Range (NSR) and surrounding ranges (Fig. 5). Except for one sample extracted from a Jurassic pluton, all K-feldspar samples are from the Lower Cambrian Prospect Mountain quartzite (Cpm), an arkosic sandstone with abundant detrital K-feldspar derived from Proterozoic basement. The vast majority of the samples were collected from the same stratigraphic interval – a feldspathic interval near the middle of the Prospect Mountain Quartzite – to minimize variations that might be attributed to differences in rock type. Across eastern Nevada, Cpm underwent regional greenschist to amphibolite facies metamorphism in the late Cretaceous (e.g., Miller et al., 1988) such that all K-feldspar samples we analyzed

were heated above the K-feldspar closure temperature window (>350 C). Following peak metamorphism, eastern Nevada experienced episodic and heterogeneously distributed extension and exhumation throughout the Cenozoic (e.g., Hose and Blake,1976; Lee et al., 1995, Miller et al. 1999) such that cooling histories derived from Cpm K-feldspar vary considerably across our dataset. Moreover, this unit experienced variable amounts of ductile strain during extension and exhumation, from unstrained to ultramylonite (e.g., Miller et al., 1983; Lee et al., 1987). Unstrained samples are clean, coarse-grained quartzites with pristine detrital textures of well-rounded quartz sand grains and up to 15% detrital microcline and orthoclase, with minor tourmaline, zircon, and mica. Depending on the precise stratigraphic interval, the unit varies from coarse-grained (0.5 to 2.0 mm) to fine-grained (150-350μm). As the unit becomes mylonitized, quartz is deformed into ribbons with variable subgrain formation and undulatory extinction and the original detrital feldspar grains form porphyroclasts that show extensive evidence for fracturing and comminution.

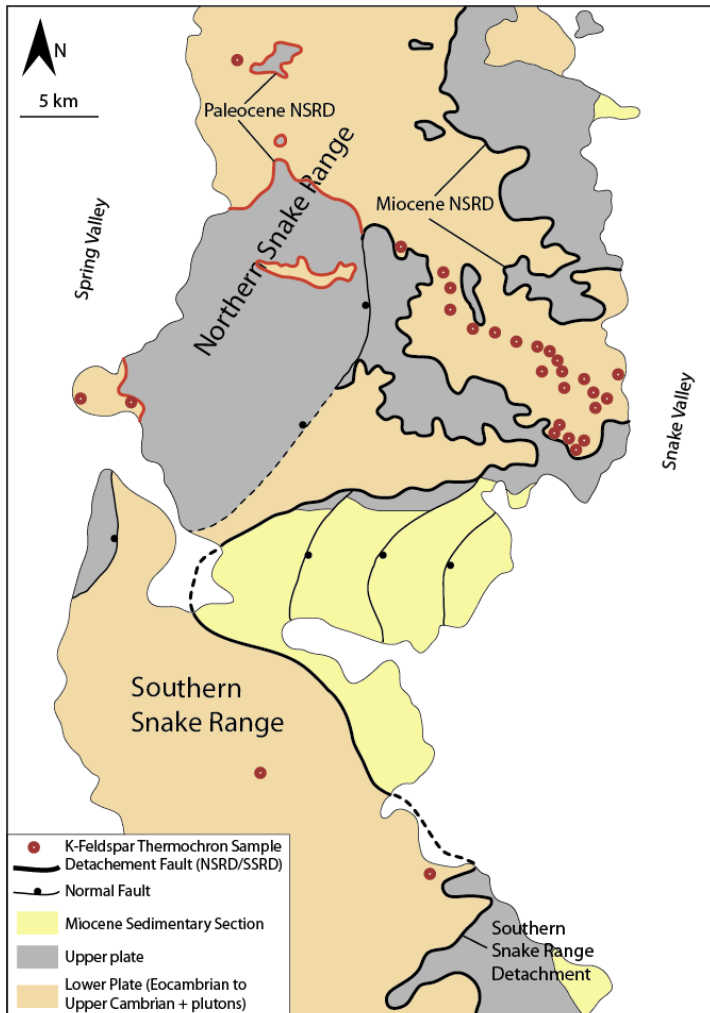## K-Feldspar Thermochronology of the Snake Range MCC

Figure 5: Simplified geologic map of the northern and southern Snake Range showing sample locations, upper/lower plate rocks, and the trace of the NSRD.

Our samples form 3 geographically distinct groups – (a) eastern/central NSR footwall, (b) western NSR footwall, and c) surrounding ranges – with each group recording distinct Cenozoic cooling histories. Samples from the eastern/central NSR remained above ~300-350 C until the mid-Miocene, then rapidly cooled through the entire K-feldspar cooling range by the late Miocene. Samples from the western NSR experienced slow Eocene–Oligocene cooling through ~350 to 250°C followed by rapid cooling in the early-mid Miocene, and samples from surrounding ranges generally experienced slow Paleocene–Eocene–Oligocene cooling through the entire K-feldspar closure window (Gans et al., 2013). We purposely

chose a dataset with variable cooling histories to explore the natural variation in MDD

parameters and test the regional consistency of MDD cooling histories.

5. METHODS

5.1. Step heating experiments and $^{40}Ar_{excess}$ –corrections

All samples were processed following identical mineral separation, analytical, and data

reduction procedures. Samples were crushed, sieved to 120-250µ, and processed using

standard magnetic and density separations techniques to produce high purity K-feldspar

separates. Samples were irradiated at the Triga reactor at Oregon State University and

analyzed in the $^{40}Ar/^{39}Ar$ geochronology laboratory at UC Santa Barbara by incremental

heating in a Staudacher-type resistance furnace. Isotopic analyses were obtained on a MAP

216 mass spectrometer, using the general procedures and system described by Gans (1997).

The flux monitor used for all irradiations was Taylor Creek Rhyolite, with an assigned age of

27.92 Ma (Dalrymple and Duffield, 1988). All errors given for $^{40}Ar/^{39}Ar$ ages reported

throughout the text and in Table 1 are ± 2σ (95% confidence).

A fundamental assumption of MDD modeling is that the diffusion characteristics and the age

spectrum of the sample being modeled have been adequately characterized during the

laboratory incremental heating experiment, so we describe in some detail how each sample

was analyzed in the laboratory. Temperatures during analysis were closely monitored using a

W-Re thermocouple, and we estimate our uncertainty in the sample temperature for each

heating step to be less than ±10°C. Each sample was subjected to nearly identical incremental

heating experiments, with heating step durations from 15 minutes to 10 hours. Temperatures

were increased monotonically, starting at 500°C and continuing until all of the argon from

the sample was depleted (generally around 1300°C). At lower temperatures, replicate

isothermal steps of increasing duration were performed as an effective way of scrubbing the

sample of "excess argon" ($^{40}Ar_{excess}$) – i.e., a trapped ^{40}Ar-rich argon component not

produced by the decay of potassium in the sample which results in anomalously old ages.

Performing these isothermal replicate steps causes ages to step down toward the real (i.e., not

influenced by $^{40}Ar_{excess}$) age (Harrison et al., 1994). We continued these isothermal steps until

the apparent ages flatten out or start to rise (Fig. 6). Thus, a typical incremental heating

schedule might begin with 3 or 4 steps each at 500, 550, 600, 650, and 700°C steps, with

each successive isothermal step of increased duration (e.g.,15, 25, 40, 60 minutes). Above the

replicate isothermal steps at 700°C, excess argon appears to disappear in most samples, and

at that point temperatures were increased monotonically by 30-50°C increments (with

occasional duplicate isothermal steps) until reaching 1100°C. At 1100°C, replicate

isothermal heating steps of increasing duration (e.g., 15, 25, 40, 70, 120, 200, 300 and in

some cases up to 600 minutes) were conducted to extract as much of the radiogenic argon as

practical before incongruent melting. In total, each of the K-feldspar incremental heating

experiments consisted of 45-50 individual heating steps and required 40 to 48 hours of

analytical time. The result is a set of exquisitely detailed age spectra and well constrained

diffusion parameters. All data were initially reduced using the EyeSoreCron program

developed by Brad Hacker, and modified using software developed in house.

One of the issues for MDD modeling many of the samples in this study is the ubiquitous

presence of anomalously old ages in some of the low-temperature steps due to $^{40}Ar_{excess}$

contamination. To remove the influence of $^{40}Ar_{excess}$, we correct our data and age spectra by

fitting a line to the youngest of the replicate low-temperature step ages starting at the point

where these steps begin to increase in age and project this line back to the y-axis. We then

use this line to assign revised $^{40}Ar_{excess}$-corrected ages to anomalously old ages believed to reflect a trapped excess argon component (Fig. 6). We recognize that this is somewhat ad hoc, as there is no reason to believe that the "true" age gradient over this portion of the spectrum has to be linear, but typically this correction affects a small fraction of the ^{39}Ar released. Furthermore, $^{40}Ar_{excess}$-corrected ages at initial temperature steps do not severely limit the models because we assign generous uncertainties to these corrected ages.
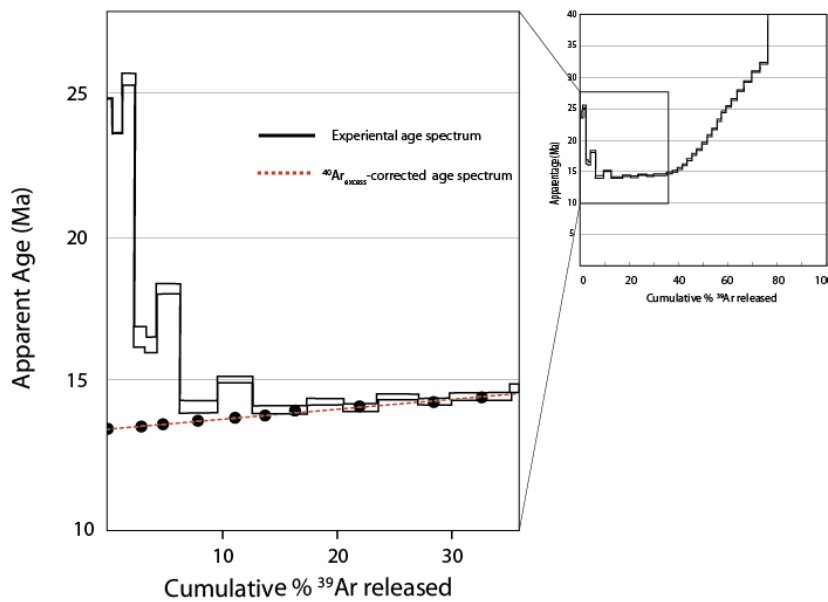

Figure 6: Example age spectrum showing how we corrected for $^{40}Ar_{excess}$. The experimental age spectrum (black) exhibits anomalously high apparent ages for the first ~15% cumulative ^{39}Ar released, a hallmark of $^{40}Ar_{excess}$ contamination. We fit a linear regression to the most reliable (i.e. youngest) ages and project this line back towards 0% cumulative ^{39}Ar released. Along this regression we assign revised $^{40}Ar_{excess}$-corrected ages to the anomalously old ages, and interpret the y-intercept as the $^{40}Ar_{excess}$-corrected minimum age.

5.2. MDD modeling

We assign MDD parameters using the *Size Extractor 4.0.0* program (Zeitler, 2004). Kinematic parameters E_a and D_0 were determined by fitting a least-squares regression to the first several temperature steps of the Arrhenius plot, and domain parameters S, ρ, and φ were assigned by fitting a synthetic $\log(r/r_o)$ curve to the measured $\log(r/r_o)$ curve. After a satisfactory $\log(r/r_o)$ fit was achieved, the experimental results were inverted using the *Arvert*

software (Zeitler, 2004; Harrison et al., 2005) to produce a model age spectrum and a model cooling history. The *Arvert* algorithm combines an initial random Monte Carlo search with a controlled random search (CRS) algorithm to assign T-t information that drives model convergence and lowers the misfit between the observed and model age spectrum. Our models were run with between 10,000 and 13,000 iterations to achieve satisfactory model convergence. Model parameters for each sample are given in Appendix A.

We assess the reliability of model results by comparing the fit of the model age spectrum to the experimental age spectrum. We deem a model fit acceptable if it, a) closely matches the inflection points of the experimental spectrum, b) doesn't have extra inflection points, and c) doesn't deviate from the experimental spectrum by >3 Ma. For example, the synthetic MDD model age spectrum of NSR-46 (shown in Figure 4d) is a close but not perfect fit because it displays several inflection points between 50-75% cumulative ^{39}Ar release that are not observed in the experimental age spectrum. For such model/experiment deviations, we remodel the sample with different domain parameters to achieve a closer fit. Because most samples display evidence for ^{40}Ar$_{excess}$, especially at the lowest temperature steps, model age spectra and ^{40}Ar$_{excess}$-corrected experimental age spectra often deviate at low cumulative fractions of ^{39}Ar released. We attribute the occasional poor model fit to this portion of the spectrum to incomplete or inaccurate correction for ^{40}Ar$_{excess}$.

In the following sections, we utilize this theoretical background of MDD theory and employ available analytical software to explore in detail the best practices and limitations of MDD modeling of K-feldspar ^{40}Ar/^{39}Ar data from a large and geologically well-constrained sample set from the northern Snake Range and environs. Specifically, we explore the natural variability of diffusion and domain parameters E$_a$, *S*, ρ, and φ, discuss how careful treatment

74

of these parameters can optimize the consistency of model results, and then use this large, internally consistent data set to demonstrate how semi-quantitative cooling histories can be extracted directly from K-feldspar incremental heating $^{40}Ar/^{39}Ar$ age spectra, absent any MDD modeling.

6. **PART I**: MDD MODEL RESULTS, PARAMETER SOLUTIONS, AND CONSISTENCY OF COOLING HISTORIES

6.1. Age spectra and model cooling histories

Experimental $^{40}Ar_{excess}$ –corrected age spectra in this dataset take two general forms. Samples from the eastern and central regions of the NSR exhibit low spectrum slopes (i.e., nearly flat spectra) for the first 40-50% cumulative ^{39}Ar released, followed by a steep spectrum slope as ages rise rapidly during the higher temperature steps to the final 1100°C temperature step at ~80% cumulative ^{39}Ar released (Fig. 6a). Age spectra from the western flank of the NSR and surrounding ranges exhibit moderate- to high-spectrum slopes over the majority of the age spectrum prior to the final 1100°C step (Fig. 6b). A few samples exhibit moderate to steep slopes over the first 50-60% of the gas released and then flatten over the highest T steps. Following the final 1100°C steps, the behavior of all spectra varies, some rise sharply and then descend, others continue to increase monotonically. The Ar released during these highest temperature steps is not thought to be a diffusional process as the feldspar commences to incongruently melt (McDougall and Harrison, 1983) and no attempt was made to characterize or model this last 10-20% of the ^{39}Ar released.

Our MDD model age spectra (modeled with parameters discussed in the following section) closely fit the shape of the experimental $^{40}Ar_{excess}$ –corrected age spectra (Fig. 6a,b).

However, model age spectra commonly yield younger ages for the first ~5-15% cumulative ^{39}Ar released than the experimental ^{40}Ar$_{excess}$ –corrected age spectra (figure 6a). This deviation between model ages and ^{40}Ar$_{excess}$ –corrected ages implies that either, a) our ^{40}Ar$_{(excess)}$ correction overestimates the ^{40}Ar/^{39}Ar ages of the initial fractions of the ^{39}Ar released (i.e., we are under correcting the amount of excess argon), or b) the assumptions inherent in our MDD modeling/parameter approach are inappropriate for the lowest temperature gas fractions released and thus are unable to replicate a linear age spectrum for the first ~5-10% cumulative ^{39}Ar release.

Model cooling histories derived from the model age spectrum and the effective closure temperatures of the assigned domains take two general forms, with the form of the cooling history related to the shape of the sample's experimental/model age spectrum. Age spectra with low slopes for the first 40-50% cumulative ^{39}Ar released followed by steeper slopes from ~50% to ~80% cumulative ^{39}Ar released yield model cooling histories with slow cooling/isothermal residence between 350 and 300°C followed by rapid cooling between ~300 and ~150°C (Fig. 7a). Age spectra with moderate to steep slopes for the majority of the cumulative % ^{39}Ar released correspond to cooling histories with slow to moderate cooling throughout the ~350 and ~150°C closure window (Fig. 7b).
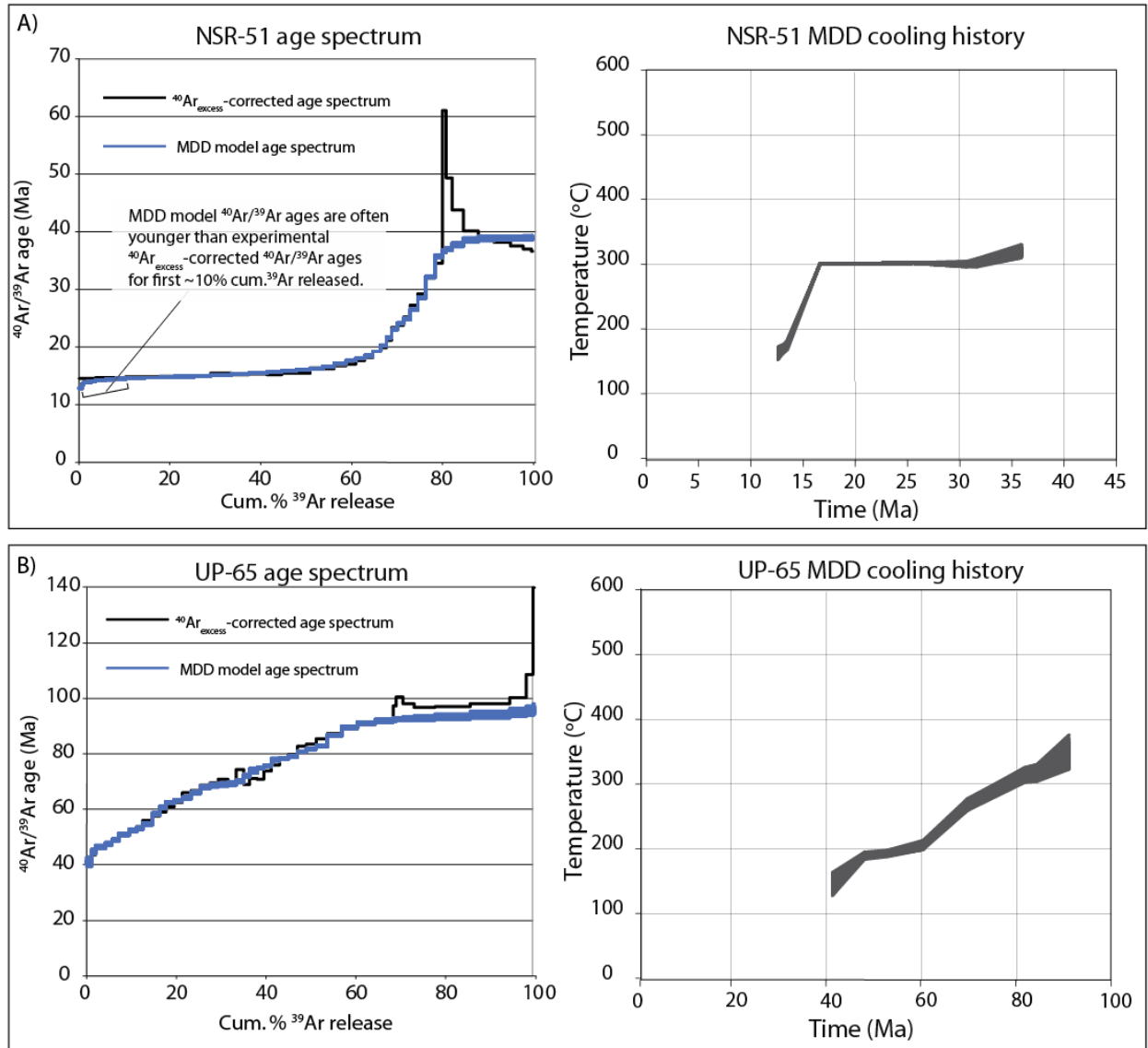
Figure 7: Experimental/MDD model age spectra and MDD model cooling histories for NSR-51 (A) and UP-65 (B). A) The age spectrum for NSR-51 remains relatively flat for the first ~50% Ar release, then steepens until the 1100°C step at ~80% cumulative Ar release. There is a close match between the experimental and model age spectrum, however the model vs. experimental spectra deviate for the first ~10% cumulative Ar release. The cooling history for NSR-51 shows rapid cooling between ~14 and 17 Ma, corresponding to the flat section of the age spectrum, and isothermal residence between 17 and 35 Ma, corresponding to the steep portion of the age spectrum. B) The age spectrum for UP-65 maintains an approximately uniform slope from the initial ^{39}Ar released to the last 1100°C step at ~70% Ar release. The resulting model cooling history shows continuous slow cooling between 41 and 90 Ma.

6.2. Domain parameters (S, ρ, and φ):

All samples in our data set require 8-10 diffusion domain sizes to fit the measured log (r/r_o) plot, with typically 2-3 domains of effective domains size $\rho < 1$, 3-4 domains with ρ of 1-10, and 2-3 domains of $\rho > 50$. Domain sizes span 4-5 orders of magnitude within each sample, from $\rho \sim 0.02$ to $\rho \sim 200$. Domain distribution parameters for each sample are provided in appendix A.

One way to illustrate the size distribution and volume fraction of each domain size is in a domain distribution "histogram," plotting volume fraction (vertical scale) vs. domain size (logarithmic horizontal scale) for each domain
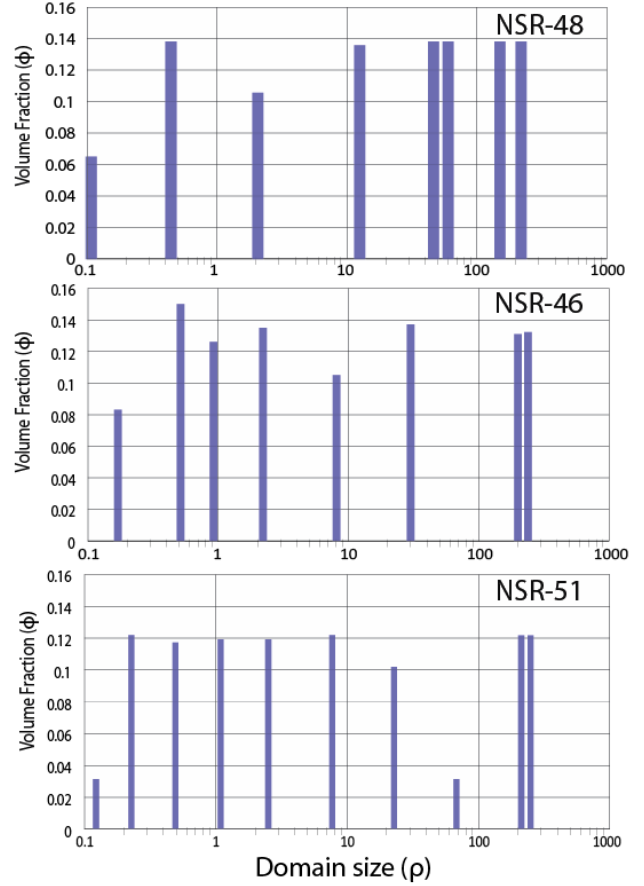

Figure 8: Domain distribution histograms for 3 selected samples showing the volume fraction of total Argon retained in different domain sizes.

size (Fig. 8). The height of each bar is proportional to the [39]Ar held in each domain size. A single domain size may account for 3-15% of the total [39]Ar within a sample.

While a domain distribution histogram clearly illustrates the domain parameters for a single sample, a better way to compare domain distributions for several samples is to plot domain size (either on a logarithmic or linear scale) vs. the cumulative fraction of [39]Ar held in the domain. Each sample's domain distribution is represented by a curve, and the general shape, slope, and inflections in this curve are a reflection of a specific domain size distribution within that sample (Fig. 9). This domain-size spectrum is analogous to an age spectrum, but

78

illustrates instead how the domain size varies with cumulative ^{39}Ar released during step heating. This type of plot assumes that the different sized domains release their gas sequentially, starting with the smallest domains, but we recognize that in reality, different domain sizes will overlap in their argon release. The main point of this type of plot is to illustrate differences in the domain size distribution among different samples.

There is a considerable range in domain size spectra within our dataset. Though each sample can be effectively modeled with 8-10 domains whose sizes range over 4-5 orders of magnitude, how the gas is distributed among smaller and larger domains varies significantly. For example, the proportion of ^{39}Ar held in smaller domains ($\rho<2$) ranges from ~16% (e.g., NSR-91) to ~47% (e.g., NSR-44), and conversely the proportion of ^{39}Ar held in large domains ($\rho>100$) ranges from as low as ~10% (e.g., NSR-56) to 65% (e.g., NSR-91). For clarity, we identify three types of domain size spectra (figure 9a inset). Type 1 domain size spectra represent the most retentive samples, as they have the lowest volume fraction in small domains and highest volume fraction in large domains. On the logarithmic domain spectral plot, these have a steep linear array up to domain sizes of $\rho>100$ for the first ~40-50% of cumulative ^{39}Ar released and then flatten abruptly for the remainder of the ^{39}Ar released before the 1100°C step (Fig. 9a). Type 1 samples typically yield the largest domain sizes (up to $\rho\sim350$) and commonly only release ~60-70% of their total ^{39}Ar before the last 1100°C step. On a linear scale plot, these samples start with a low slope but inflect upwards sharply at 20-40% of the cumulative ^{39}Ar released (Fig. 9b).

Type III domain size spectra are representative of the least retentive samples. These have the highest volume fraction of ^{39}Ar (e.g., 40-48%) held in small domains ($\rho<2$) and the lowest volume fraction (10-20%) held in large domains ($\rho>100$). On a logarithmic vertical axis (Fig.

79

9a), Type III samples produce a low-slope linear array through the entire domain spectrum. These types of samples have smaller maximum domain sizes (ρ ~80-150) and tend to release 85-90% of their total ^{39}Ar prior to the onset of incongruent melting at 1100°C. On a domain size spectrum with a linear vertical axis, Type III samples generate curves with conspicuous inflections that are displaced far to the right (60-70% of the cumulative ^{39}Ar released) and only climb to domain sizes of ρ ~100 (Fig. 9b).

Type II samples by default are intermediate between I and III and represent the majority of the samples analyzed. These spectra have intermediate slopes in logarithmic domain size spectrum space (Fig. 9a), and, in linear domain spectrum space, inflect upwards at 40-60% of the cumulative ^{39}Ar released (Fig. 9b). The maximum domain size for Type II samples is ρ~200-250.
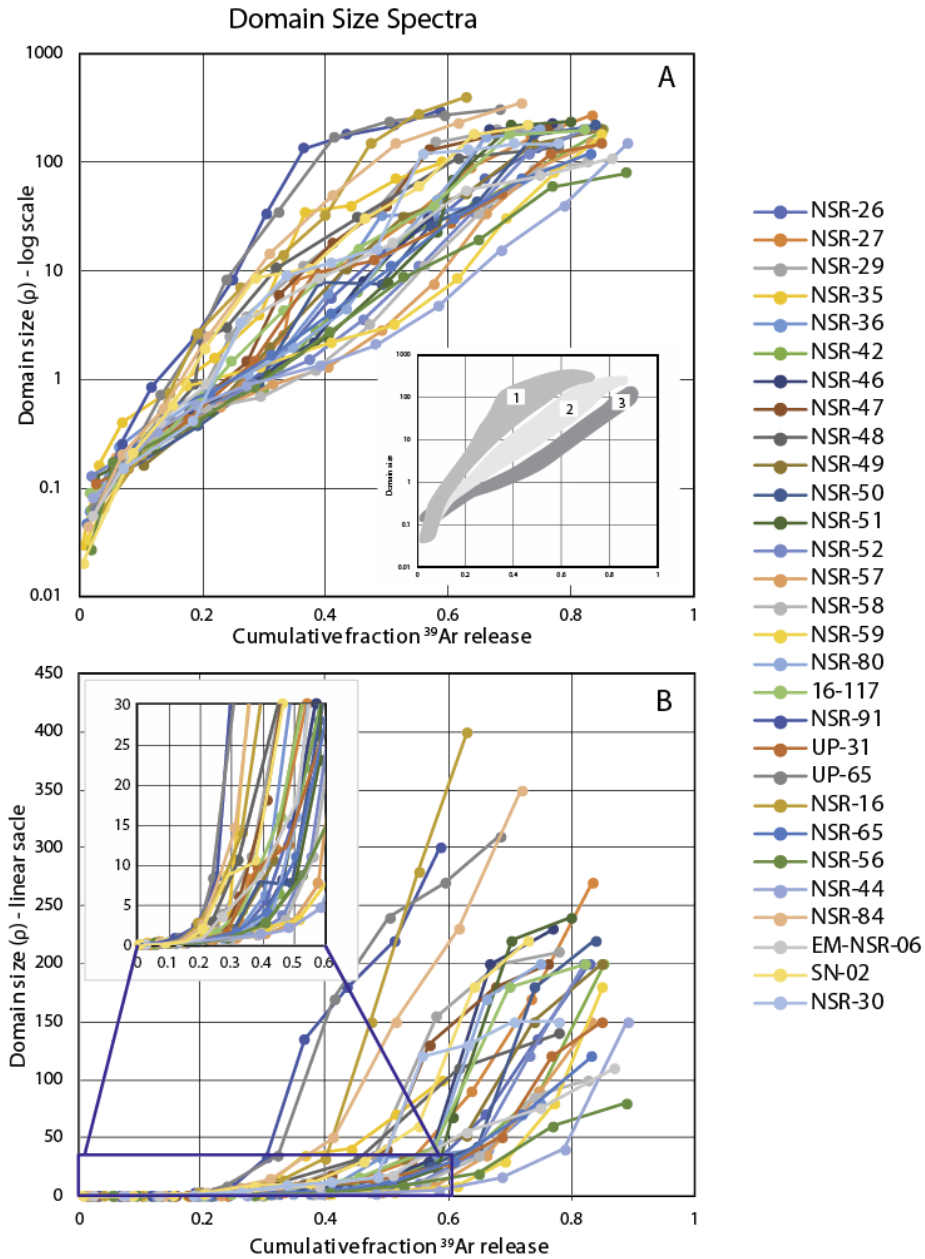
Figure 9: Domain size spectra for all samples modeled in this study. Each curve illustrates the general domain size/volume fraction distribution by plotting domain size (ρ) vs. cumulative percent ^{39}Ar released. A) Domain size spectra plotted on a logarithmic vertical scale yield nearly linear arrays but with varying slopes. The form of Type I, II, and III domain size spectra are shown in the inset (see text for discussion). B) Domain size spectra plotted on a linear vertical scale yield concave-up curves with a prominent inflection point at a size range of 1-5. This inflection point varies from ~20-55% cumulative ^{39}Ar released.

These differences in domain size distributions in different samples correlate reasonably well with the petrographic characteristics and grain size (Figure 10). Specifically, Type I domain size distributions (i.e., the most retentive samples) are K-feldspar separates from relatively unstrained, coarse-grained feldspathic quartzite, and are composed of large, clear microcline and orthoclase detrital grains that are typically 300-800 μm (Fig. 10a). In contrast, Type III domain size spectra correspond to samples where the K-feldspar grains are predominantly ~50-150 μm. Type III samples range from ultramylonites, where the small grain size is a result of deformation, to relatively unstrained fine-grained quartzite, where the grain size reflects the original detrital grain size (Fig. 10c). Type II domain spectra correspond to samples with intermediate grain size (~150-250 μm) and/or samples with a mix of sparse large K-feldspar porphyroclasts that have been partially fractured and/or pulled apart during deformation and many smaller K-feldspar fragments (Fig. 10b). These observations illustrate the important control that the grain size of the K-feldspar exerts on the domain size distribution and suggests that the largest modeled diffusion domains may be broadly proportional to the size of the individual detrital grains.
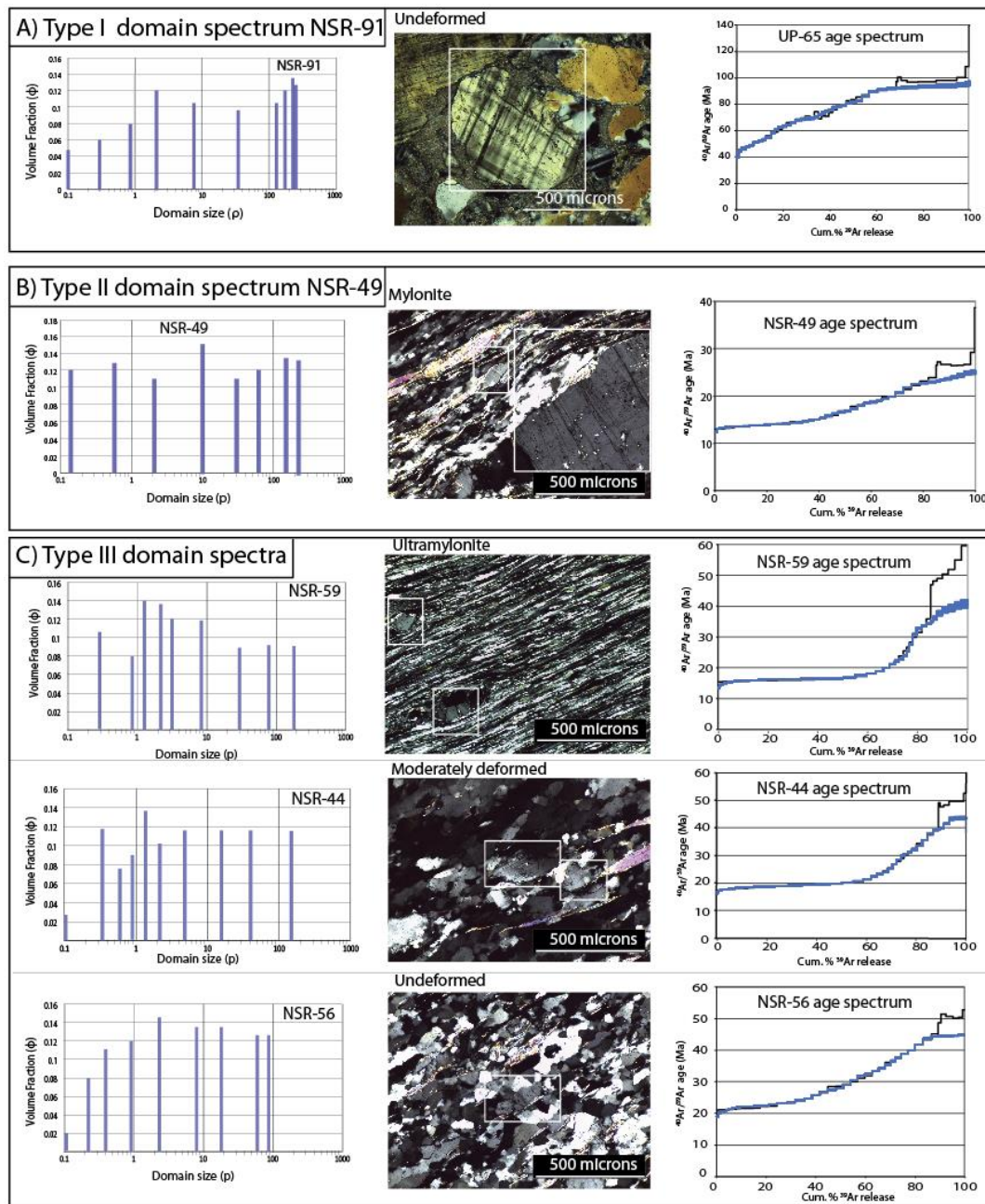
Figure 10: Domain distribution histograms, photomicrographs, and experimental/model age spectra for samples corresponding to Type I, II, and III domain size spectra (figure 7). A) Type 1 domain size spectra correspond to samples with a large volume fraction of the cumulative fraction of ^{39}Ar released held in large domains ($\rho > 100$), and have large, relatively undeformed K-feldspar grains. B) Type II domain distribution spectra correspond to samples with a relatively equal volume fraction of Ar held within large and small domain. Type II K-feldspar grains are generally fine- to medium-grained K-feldspar, with occasional large >500μm grains. However, large grains tend to be significantly fractured by distributed stain. C) Samples with Type III domain size spectra retain a large volume fraction of Ar within small domains ($\rho < 2$), are fine-grained, and show variable amounts of strain. The age spectra for Type II and Type III domains are similar, suggesting that the cooling history does not control the domain size distribution of a sample.

There appears to be little correlation between the magnitude of strain, or the calculated thermal history, and the domain size distribution – other than the mylonitic strain's role in mechanically reducing the grain size of the original detrital K-feldspar. Type II and III domain size spectra consist of both highly mylonitized K-feldspars that cooled rapidly in the Miocene and relatively unstrained K-feldspars that cooled much more slowly in the Paleocene to Oligocene (Fig. 10b,c). Similarly, we find adjacent samples that have different Type II and Type III domain size spectra but yield indistinguishable age spectra and cooling histories. Indeed, it is the systematic progression of ages and model cooling histories across the study area, despite significant variations in the domain size distribution, which give us confidence in the validity of our MDD models.

6.3. Effect of domain size, volume fraction, and the number of domains on cooling histories:

Lovera et al., (1991) showed that domain parameter solutions for a given sample are non-unique, in that different domain solutions that satisfactorily fit the log(r/r_o) plot will produce non-distinguishable model results as long as an appropriate minimum number of domains are assigned. To determine the most appropriate minimum number of domains required to model a sample's cooling history, we modeled sample NSR-47 with four different parameter solutions with a constant E_a value (Fig. 11). Blue and red results are modeled with 8 and 9 domains, respectively, and yield comparable log (r/r_o) fits and produce indistinguishable cooling histories. Green results, modeled with seven domains, do not fit the log (r/r_o) plot between 45 and 70% ^{39}Ar released as well. As a result, the green model age spectrum deviates from the experimental age spectrum between ~45 and 70% cumulative ^{39}Ar release, and the cooling history deviates from the blue and red models at ages that correspond to the

84

45 and 70% cumulative [39]Ar release. Gold results, modeled using three domains, do not fit the log (r/r_o) plot. As a result, the model age spectrum fails to match the experimental age spectrum, and the calculated cooling history deviates significantly from the other models. Thus, it is apparent that a baseline number of domains is required to produce consistent cooling histories. In this example, NSR-47 requires at least eight domains to satisfactorily fit the log (r/r_o); fewer domains produce erroneous cooling histories. To ensure that we were calculating the best-fit cooling history for a sample, we opted to assign 8-10 domains per sample, with most samples modeled with 10 domains – the maximum number of domains permitted by the *Size Extractor/Arvert* software.
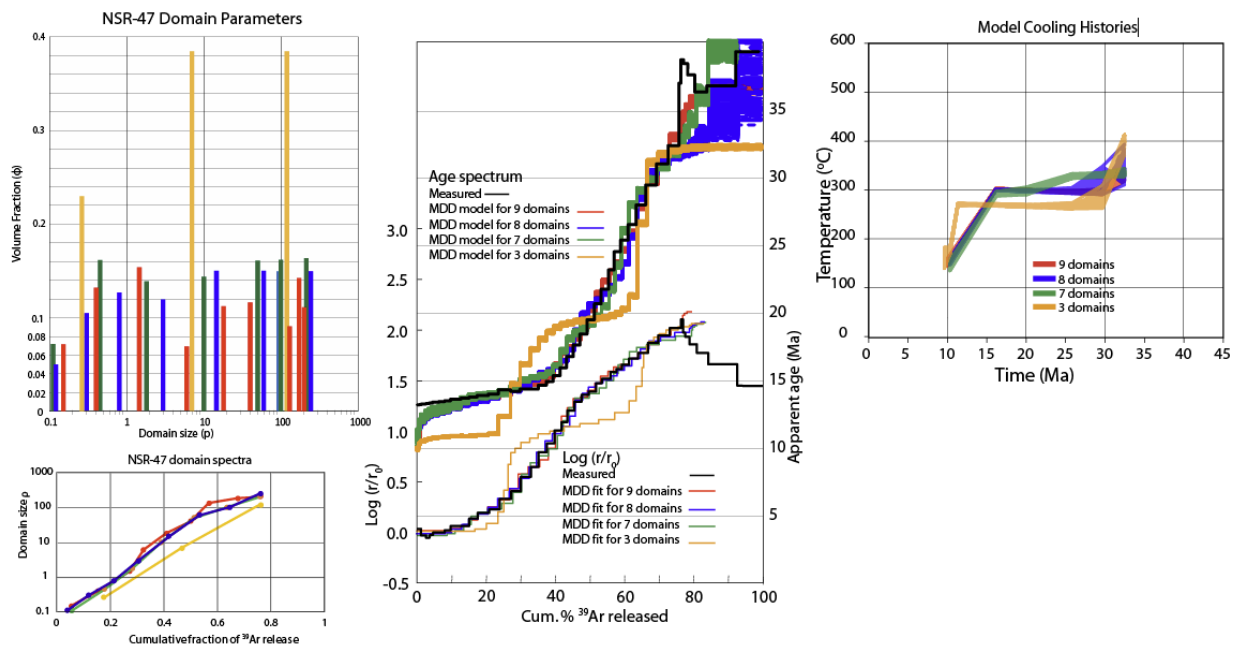

Figure 11: MDD model solutions for NSR-47 modeled with different domain parameters. Models run with 8 and 9 diffusion domains (red/blue) produce nearly identical model age spectra and cooling histories. Models run with 7 domains (green) struggle to fit the experimental age spectra and the resulting cooling history deviates from red/blue. Models run with 3 domains (gold) cannot match the experimental cooling history and the resulting cooling history does not resemble those of the other models.

.

85

6.4. Effect of activation energy and domain shape on model cooling histories:

Activation energies (E_a) of Ar diffusion were determined for both infinite slab and spherical geometries for the 28 samples modeled in this study. Because the assigned domain geometry constant, α, affects the domain radius, *r*, of the diffusion domain, different assigned domain shapes produce different Arrhenius plots with different E_a. In our dataset, assuming an infinite slab geometry gives E_a from 42 to 53 kcal/mol with a mean (±1 S.D) of 48.1±1.6 kcal/mol, and spherical geometry gives 43.6 to 54.9 kcal/mol with a mean of 49.2±2.5 kcal/mol. Typically, E_a for spheres is 0.6 to 5.5 kcal/mol higher than slabs, with an average of 1.8 kcal/mol higher. Both the slab and spherical domain E_a values in our datset are consistent with the E_a range of 46±6 kcal/mol (spheres) reported in the extensive compilation by Lovera et al. 1997 (Fig. 12). To maintain consistency within our dataset, we modeled all samples with an infinite slab geometry.

An important question remains as to whether the observed scatter of >10 kcal/mol in E_a values is real or an artifact of analytical errors and/or the vagaries in fitting a line to the first few temperature steps on an Arrhenius plot. Here, we explore whether our spatial array of cooling histories is more internally consistent and systematic if we honor the E_a obtained for each sample, even though these vary by > 10 kcal/mol, or if we assign the same mean E_a to all samples.
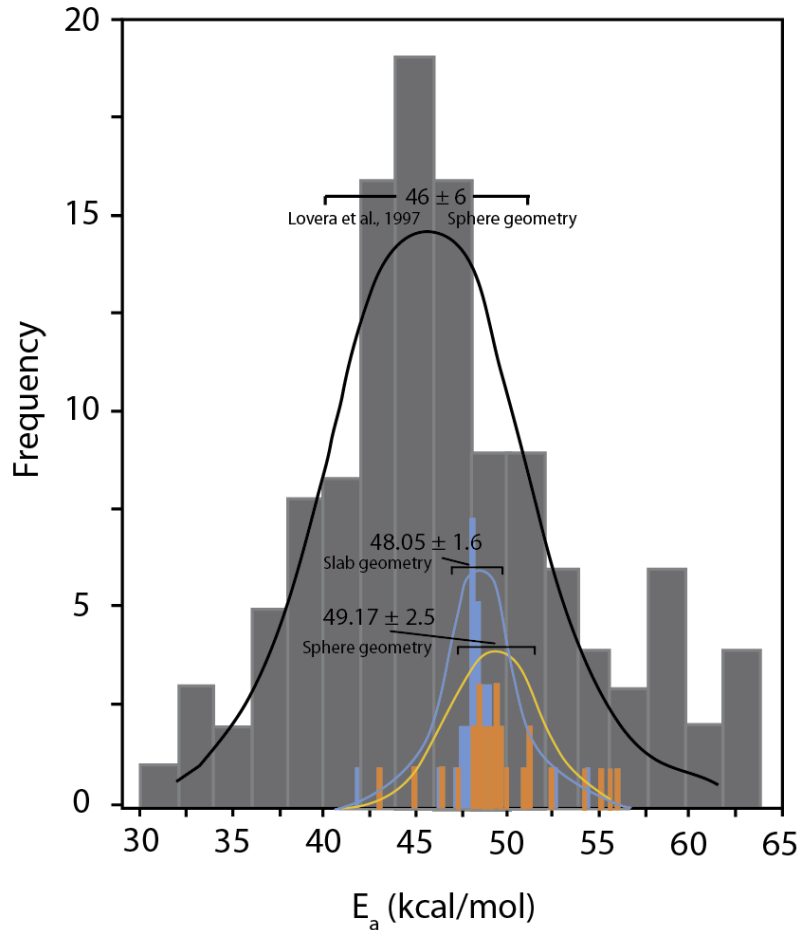
Figure 12: Histogram of E_a values of Ar diffusion from K-feldspar. Grey data are a compilation of E_a values for a spherical domain geometry from Lovera et al. (1997) with a mean and standard deviation of 46 ± 6 kcal/mol. In this study, Ea values were determined for both a spherical and slab domain geometry. Slab geometries have an average Ea value of 48.05 ± 1.6 kcal/mol and sphere geometries have an average Ea of 49.17 ± 2.5 kcal/mol.

We test this by comparing the cooling histories of nearby samples that yield significantly different E_a values but whose thermal histories should be virtually identical. We focus on four samples with outlier E_a values – two with E_a values well below the average E_a (NSR-30 with an E_a=42.9 kcal/mol and NSR-42 with an $E_a = 46.1$ kcal/mol) and two with E_a values above the average E_a (NSR-50 with an $E_a = 53.1$ kcal/mol and NSR-80 with an $E_a = 53.1$ kcal/mol) – and compare their modeled cooling history to nearby samples (<300m away)

with nearly identical age spectra and more typical E_a values of ~48 kcal/mol. We find that NSR-30 and NSR-42, both with below-average E_a values, yield consistently cooler MDD-derived temperatures for the same age in comparison to neighboring samples. Similarly, NSR-80 and NSR-50, both with above-average E_a values, yield consistently hotter MDD-derived temperatures for the same age in comparison to adjacent samples (Fig.13). We remodel the data of these outlier samples using an E_a value that closely matches the mean E_a value of the dataset instead of their specific Arrhenius-derived values, and find that the revised cooling histories closely match the cooling curves of adjacent samples and fall correctly into the spatial trends of the entire dataset. This finding suggests that the variability of E_a values in our dataset is likely an artifact of either analytical error or inaccurate modeling of the data and doesn't reflect natural variation in E_a of Ar diffusion in K-feldspar.
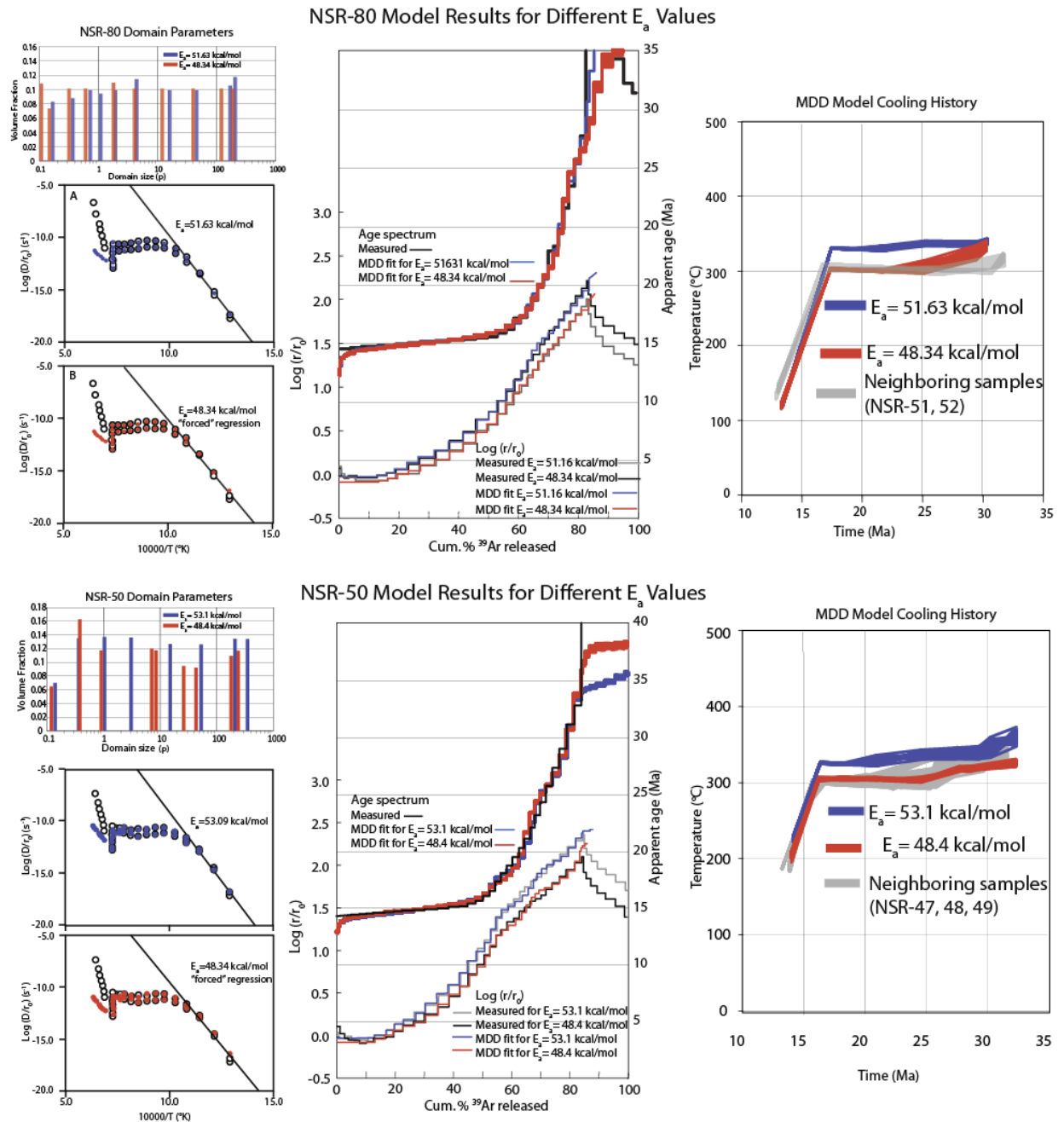
Figure 13: MDD model results for samples with outlier E_a values (NSR-80 and NSR-50). For each sample, blue results are modeled using their experiment-derived E_a and red results are modeled with an assigned E_a that falls within the average and standard deviation E_a of the data set. For each sample, the model cooling histories for an assigned average E_a value (red) better match the cooling histories of neighboring samples (shown in gray on the MDD model cooling history plot).

6.5. Summary of best practices to generate an internally consistent dataset of differential

   cooling histories:

The previous sections discuss the techniques and parameters used to construct a large MDD dataset, and how careful treatment of these parameters can increase the consistency of cooling histories within a dataset. To minimize uncertainty in data recovery and interpretation, we recommend that K-feldspar samples be collected from the same rock type, have a similar grain size, and be subjected to identical step heating schedules. When assigning domain parameters, we find that samples require a minimum of 8 diffusion domains to match the measured log (r/r_o); fewer domains provide less satisfactorily fits to the experimental data, resulting in erroneous cooling histories. We also find that domain parameter solutions are non-unique as long as the required minimum number of domains is met. All samples should be modeled using the average Ea value of the entire dataset. Further, all samples must be modeled with the same assumed domain geometry, as not to skew the average E_a of the dataset.

7. **PART II**: EXTRACTING T-t COOLING HISTORIES DIRECTLY FROM A K-FELDSPAR $^{40}Ar/^{39}Ar$ AGE SPECTRUM

Creating a large dataset of MDD cooling histories (as discussed in Part 1) is a repetitive and time-consuming process that can be disproportionate to the research need. Often, researchers need only an approximate cooling history to assess differential cooling histories and test geologic hypotheses. This section develops a schema for constructing semi-quantitative cooling histories directly from an experimental K-feldspar age spectrum, bypassing the laborious process of MDD modeling.

It is generally accepted that the ages on a K-feldspar spectrum record the cooling history through a temperature interval of approximately 350 to 150°C and that the shape of an age spectrum holds valuable information regarding the precise details of its cooling history. For example, steps of constant age from a significant portion of the cumulative ^{39}Ar released (i.e. flat or low-slope age gradients) indicate rapid geologic cooling. Conversely, steep spectrum slopes – where ages climb rapidly across relatively small percentages of the cumulative ^{39}Ar released – represent slow cooling or isothermal residence, and inflection points indicate a change in cooling rate. The ^{40}Ar$_{excess}$-corrected age of the initial gas released records when a sample cooled through the coldest part of its closure window (typically between ~150 and 220°C), and the last of replicate 1100°C steps records when a sample cooled through the upper bound of its closure window (typically ~350°C). Though these relationships are useful, they are qualitative, and the age spectrum does not provide a precise assessment of the complete T-t history.

We use our large data set of MDD cooling histories that record varying rates and timing of cooling to identify quantitative relationships between the shape of an age spectrum and its MDD-derived T-t curve. Specifically, we quantify relationships between, 1) spectrum slope and the modeled geologic cooling rate, 2) the spectrum slope of the first Ar released and the minimum effective cooling temperature (i.e., the cooling temperature recorded by the youngest age), and 3) the modeled effective cooling temperature (ECT) as a function of the fraction of the cumulative argon release, what we term a "temperature spectrum." We use these relationships to show that one can construct reasonably accurate geologic T-t histories directly from the K-feldspar ^{40}Ar/^{39}Ar age spectrum and that such semi-quantitative results compare favorably with those obtained by rigorous MDD modeling. We conclude this

section with a detailed suggested procedure or "cookbook" for extracting approximate T-t cooling histories directly from a K-feldspar incremental heating $^{40}Ar/^{39}Ar$ age spectrum.

7.1. Methods:

From each sample's age spectrum, we tabulated a) the spectrum slope (in units of Ma/Cumulative fraction Ar release) for the initial (~0-15%) ^{39}Ar released, b) the spectrum slope for various other linear portions of the age spectrum, c) both the $^{40}Ar_{excess}$-corrected minimum age of the experimental age spectrum and the minimum model age of the MDD modeled age spectrum, d) the age and cumulative fraction of gas released for major inflection points in the age spectrum, and c) the age of the last replicate 1100°C step of the experimental spectrum (Fig. 14a).

From each sample's MDD model cooling history, we tabulate a) the effective cooling temperature (ECT) corresponding to each incremental $^{40}Ar/^{39}Ar$ spectrum age, and b) the cooling rate over the age interval of a calculated spectrum slope (Figure 14b). We extract ECT values by fitting a smooth high-order polynomial function through the nodes of each sample's best fit MDD modeled cooling history and then solve for the ECT at a given age ± uncertainty. The assigned uncertainties for the extracted ECT values reflect the mean standard error (±2σ) of the sample's cooling curve and incorporates our age uncertainties. We determine the model cooling rate for each specific age interval (i.e., the slope of the cooling curve) by taking the first derivative of the polynomial fit to the model cooling history and solving for dT/dt at the desired ages ± uncertainty.

A summary of values from each sample's experimental/model age spectrum and MDD cooling history are shown in table 1. Each samples experimental age spectrum, model age

spectrum, and MDD cooling history is available in appendix A. With these values, we design

a series of plots to explore the relationship between age spectra features and their respective
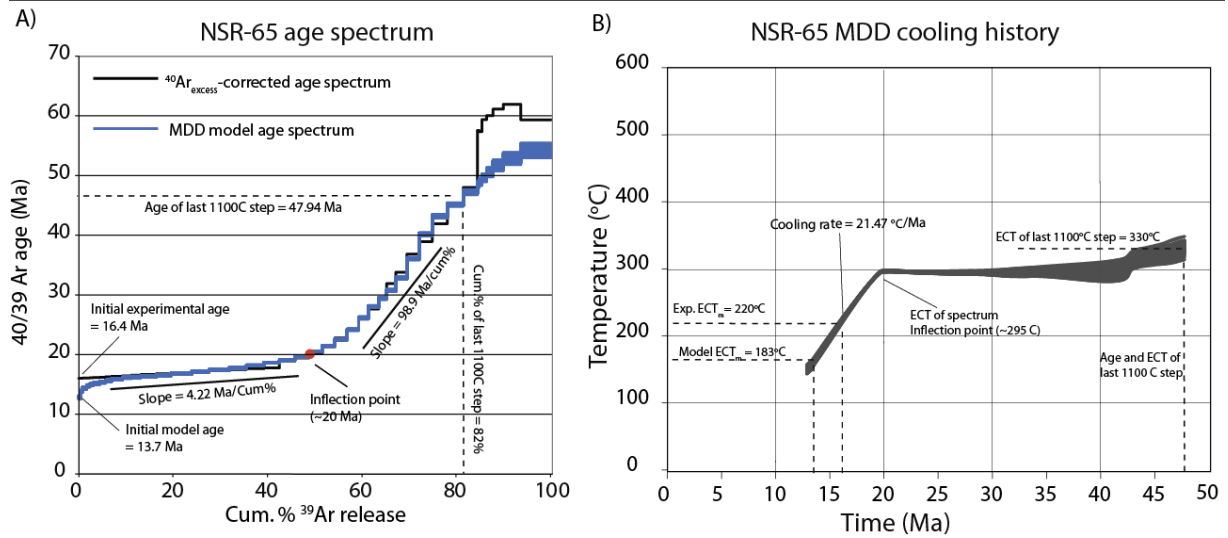
cooling histories (figure 15-19).

Figure 14: Experimental and MDD model $^{40}Ar/^{39}Ar$ age spectrum (A) and MDD cooling history showing how age, cumulative % ^{39}Ar released, and temperature data are extracted for each sample. A) Experimental and model $^{40}Ar/^{39}Ar$ age spectrum for NSR-65 showing the i) initial $^{40}Ar_{exess}$-corrected and model ages, ii) the slope of the age spectrum at two locations, iii) the age and cumulative percent ^{39}Ar released of the major inflection point, and iv) the age and cumulative percent ^{39}Ar released of the last 1100°C temperature step. B) Model cooling history for NSR-65 showing the ECT of the minimum experimental age, the ECT of the minimum model age, the ECT of the major inflection point, the ECT of the last 1100°C temperature step, and model cooling rate corresponding to the initial spectrum slope.

Table 31: Age spectra and cooling history attributes

Sample	Min. 40Ar excess corr age (Ma)	Min model age (Ma)	% deviation b/w exp and model minimum age	Low T excess Ar (%)	Final 1100C step age (Ma)	Final 1100C temp step Cum. fraction Ar	Low T spectrum slope (Ma/cum. fract. Ar)	High T spectrum slope (Ma/cum. fract. Ar)	Low T model cooling rate (C/Ma)	High T model cooling rate (C/Ma)	Exp ECTm ©	Model ECTm (C)	Diff Exp-Mod ECTm	ECT (final 1100C temp step)
NSR-26	14.05 ± 0.35	12.15 ± 0.3	17.96	34.28	54.309 ± 0.073	0.8303	4.298	142.34	22.81	2.16	233.8 ± 8.1	183.2 ± 8.1	50.60	361
NSR-27	13.98 ± 0.4	12.04 ± 0.52	16.66	18.66	40.29 ± 0.052	0.8314	3.67	73.89	22.35	1.63	247.1 ± 9.1	195.3 ± 18.4	53.00	341
NSR-29	13.81 ± 0.3	13.03 ± 0.42	6.03	29.01	31.76 ± 0.116	0.7790	3.132	47.35	53.12	3.48	236.3 ± 16.2	193.8 ± 21.9	42.50	347.84
NSR-30	13.93 ± 0.15	12.98 ± 0.39	7.76	10.65	41.077 ± 0.06	0.7470	3.77	63.54	32.91	0.00	232.1 ± 11.2	196.6 ± 19.1	35.60	344.57
NSR-35	14.41 ± 1	12.93 ± 0.79	6.24	59.04	27.993 ± 0.52	0.59	4.95	65.18	38.35	6.55	236.2 ± 37.2	205.9 ± 23.4	30.30	335
NSR-36	14.27 ± 0.25	13.4 ± 0.4	4.90	43.94	28.096 ± 0.113	0.75	3.26	58.59	55.63	2.41	233.5 ± 14.4	190.3 ± 18.1	43.20	360
NSR-42	14.42 ± 0.25	12.92 ± 0.58	9.72	26.64	33.81 ± 0.08	0.85	1.85	43.80	38.07	2.81	226.5 ± 9.3	176.1 ± 21.6	50.40	304
NSR-46	13.3 ± 0.15	12.68 ± 0.26	2.84	25.21	23.64 ± 0.114	0.77	2.86	43.47	58.52	2.26	205.7 ± 9.1	183.8 ± 15.6	21.90	327.8
NSR-47	13.29 ± 0.2	12.03 ± 0.27	12.40	26.03	32.592 ± 0.09	0.76	3.50	56.09	30.68	0.00	236.4 ± 8.8	190.9 ± 9.3	45.50	324.35
NSR-48	13.23 ± 0.2	13.12 ± 0.21	0.06	6.34	28.779 ± 0.063	0.78	5.39	37.23	64.80	1.29	204.2 ± 8.6	203.6 ± 15.4	0.60	340
NSR-50	14.28 ± 0.2	13.3 ± 0.3	10.96	15.06	32.793 ± 0.14	0.84	1.87	67.56	50.93	1.44	226.3 ± 9.1	184.7 ± 17.2	41.60	301
NSR-51	14.503 ± 0.15	13.18 ± 0.31	7.42	69.26	34.532 ± 0.064	0.80	1.78	110.15	46.14	0.00	257.2 ± 9.6	210.4 ± 15.5	46.80	304
NSR-52	14.66 ± 0.15	13.15 ± 0.19	10.10	39.60	35.824 ± 0.083	0.82	1.38	110.07	40.37	0.75	247.7 ± 8.7	188.7 ± 8.7	59.00	314
NSR-57	14.69 ± 0.3	13.7 ± 0.6	6.91	21.80	28.611 ± 0.105	0.83	2.30	65.42	49.47	2.22	252.6 ± 16.2	208.9 ± 9.1	43.70	333
NSR-58	14.85 ± 0.25	13.64 ± 0.4	5.79	40.53	37.687 ± 0.111	0.83	2.56	152.78	46.05	0.46	239.6 ± 11.3	203.2 ± 24.5	36.40	310
NSR-59	15.46 ± 0.1	13.8 ± 0.4	8.72	24.37	35.867 ± 0.097	0.85	1.63	103.10	38.96	0.78	252.7 ± 4.1	202.8 ± 17.3	49.90	335
NSR-80	14.838 ± 0.2	12.31 ± 0.36	6.53	36.54	32.622 ± 0.114	0.75	1.67	89.34	47.24	1.74	270.9 ± 14.3	227.6 ± 16.1	43.30	338
NSR-63	15.74 ± 0.4	14.88 ± 0.36	6.86	26.34	45.05 ± 0.112	0.75	5.40	82.16	28.13	0.99	234 ± 5.9	200.4 ± 17	33.60	320
NSR-65	16.94 ± 0.20	13.71 ± 0.35	23.56	13.67	47.94 ± 0.0075	0.82	4.22	98.90	21.47	0.72	231 ± 3.4	183.7 ± 16.1	47.30	330
NSR-56	21.03 ± 0.2	20.01 ± 0.5	4.57	6.49	45.048 ± 0.211	0.89	4.15	46.55	22.96	2.11	210 ± 10.2	20.1 ± 18	189.90	370
NSR-44	17.436 ± 0.1	16.44 ± 0.38	3.47	5.34	37.338 ± 0.086	0.89	4.83	71.86	34.02	1.26	232.1 ± 3.8	211.9 ± 17.5	20.20	295
16-117	23.53 ± 0.8	19.55 ± 1.6	11.63	16.7	45.86 ± 0.11	0.82	58.774	27.73	1.33	5.80	178.9 ± 0.7	176.7 ± 13.2	2.20	320
NSR-91	35.5 ± 1.5	37.1 ± 1.25	6.61	10.65	73.354 ± 0.069	0.59	57.688	168.14	8.81	N/A	179.4 ± 10.5	159.8 ± 14.3	19.60	305
UP-31	27.24 ± 0.5	25.7 ± 2.5	19.47	1.95	52.628 ± 0.116	0.85	63.65	41.77	14.52	15.69	186.2 ± 0.5	168.8 ± 18.7	17.40	355
NSR-84	15.42 ± 0.5	15.23 ± 0.27	3.77	12.27	41.251 ± 0.043	0.72	9.9855	65.68	33.88	2.38	215.2 ± 1.9	194.6 ± 9.9	20.60	345
EM-NSR-06	18 ± 0.4	17.65 ± 0.25	2.39	11.22	47.044 ± 0.055	0.87	11.36	47.91	29.25	1.55	226.6 ± 12.1	213.2 ± 16.2	13.40	355
UP-65	41.6 ± 2.5	41.15 ± 2.5	3.94	13.48	91.833 ± 0.088	0.68	98	120.30	6.13	4.13	171.8 ± 8.9	161.8 ± 10.1	10.00	342
NSR-12	25.29 ± 0.4	25.19 ± 0.35	0.32	4.10	42.53 ± 0.142	0.84	23.185	20.00	20.79	27.22	203.4 ± 9.5	199.3 ± 15.9	4.1	362

7.2. Relationship between spectrum slope and model cooling rate

Age spectrum slopes (m_s) range from ~1 to 155 Ma/cumulative fraction ^{39}Ar released. These are calculated by dividing the age difference across a linear segment of the age spectrum by the fraction of ^{39}Ar released over that segment. Calculated low-temperature m_s values measured over the first 10-30% of the cumulative ^{39}Ar released range from 1 to 98 Ma/fraction ^{39}Ar released (mostly less than 10), and m_s values at higher percentages of ^{39}Ar released (e.g., 40-80%) range from ~20 to 155 Ma/fraction ^{39}Ar released. Model cooling rates (Γ) that correspond to the age intervals over which a slope was measured range from 0-65°C/Ma and are, not surprisingly, inversely correlated with m_s. Uncertainties in model cooling rates derive from the scatter in acceptable cooling rates over the range of ages within a slope interval.

Several of the modeled thermal histories predict intervals of slight warming at rates of ~1°C/Ma. We assume monotonic cooling for all of our samples and interpret these intervals of slight warming to be the result of the randomization algorithms of the modeling approach (i.e., Monte Carlo/CRS best fits) and not geologic heating, but recognize that more complex thermal histories with periods of heating are also possible. Here, we assign a cooling rate of 0°C/Ma to the apparent intervals of slight geologic heating.

Hypothetically, if an entire age spectrum records cooling through a ~200°C temperature range (from ~350°C to ~150°C), simply dividing the total cooling (200°C) by the average spectrum slope yields a single cooling rate, expressed by $\Gamma_{hyp} = 200/m_s$. We here attempt to quantify the relationship between Γ and m_s more rigorously using the measured slopes from various parts of age spectra and the associated modeled cooling rates.

The general strong correlation between the m_s and Γ is illustrated in Figure 15. Low m_s values (<5 Ma/cumulative fraction [39]Ar released) correspond to Γ >30°C/Ma, intermediate m_s values (5-25 Ma/cumulative fraction [39]Ar released) correspond to Γ of 10-30°C/Ma, and high m_s values (>25 Ma/ cumulative fraction [39]Ar released) correspond to Γ <10°C/Ma. The data form a broad hyperbolic curve but with considerable scatter, best fit by the polynomial

$$\Gamma = -6.1\ x10^{-5}(m_s)^3 + 1.7\ x10^{-2}(m_s)^2 - 1.5\ (m_s)\ +\ 40.1$$

with an $R^2 = 0.9$ and a standard error of 5.4 °C/Ma.

The measured Γ vs. m_s curve significantly deviates from the Γ_{hyp} curve for spectrum slopes <30 Ma/cumulative fraction [30]Ar release (Fig. 14). For the lowest spectrum slopes (<7 Ma/cumulative fraction [30]Ar release), Γ_{hyp} cooling rates greatly exceed the calculated model cooling rates, and for spectrum slopes between 7 and 30 Ma/cumulative fraction [30]Ar released, the Γ_{hyp} curve is lower than the measured model cooling rates. We place higher confidence in our model Γ vs. m_s curve than the Γ_{hyp} curve and therefore use the former to assign approximate geologic cooling rates to any relatively linear portion of an age spectrum.

Cooling rate v. spectrum slope

$\Gamma_{hyp} = 200/m_{shyp}$

$\Gamma_{meas} = 6\times10^{-5}(m_s)^3 + 0.017(m_s)^{32} - 0.032(m_s)^2 - 1.47(m_s) + 40.10$

$R^2 = 0.90$

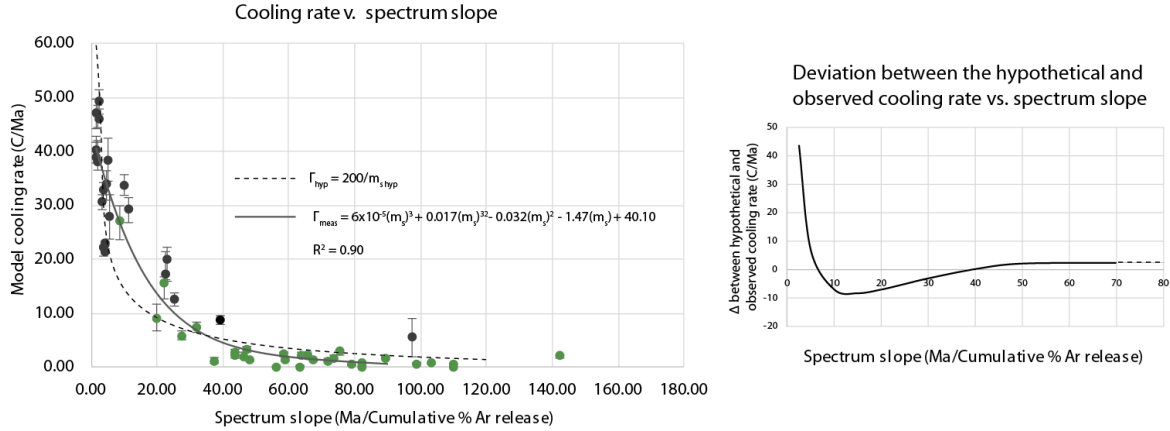**Deviation between the hypothetical and observed cooling rate vs. spectrum slope**

Figure 15: Relationship between model cooling rate (Γ) and spectrum slope (m_s). Left) Plot of model cooling rate vs. spectrum slope. Black data are cooling rates derived from spectrum slopes of the first 10-30% of the cumulative [39]Ar released from a given spectrum and green data are cooling rates derived from spectrum slopes between ~40-80% cumulative [39]Ar released from a give age spectrum. Also plotted is the hypothetical cooling rate vs. spectrum slope curve (dashed line). Right) Plot showing the deviation between the hypothetical cooling rate vs. spectrum slope curve and the observed cooling rate vs. spectrum slope curve.

7.3. Relationship between the initial spectrum slope and the minimum ECT

The ECT of the youngest spectrum age, ECT_m, is the low-temperature limit of the sample's closure window. From each sample's MDD model cooling history, we extract the ECT_m from both the minimum model age and the experimental [40]Ar_{excess}-corrected age. Across the entire dataset, ECT_m values for the minimum experimental [40]Ar_{excess}-corrected ages span nearly 100°C, from ~160°C to ~260°C, and ECT_m values for minimum model ages span from ~140°C to ~200°C.

Both the experimental and model ECT_m values systematically decrease with increasing initial spectrum slopes – i.e., the steeper the initial spectrum slope, the lower the ECT_m. These data arrays can be fit by the following equations

$$Experimental\ ECTm\ =\ -19.6\ln(m_s) - 250.8\ (R^2 = 0.75 \text{ and St. Err.} = 14.8\ °C)$$

and

$$Model\ ECTm\ =\ -8.4\ln(m_s) + 194.0\ (R^2 = 0.45\ \text{and St. Err.} = 12.1\ °C)$$

(Fig. 16). These curves diverge as the initial slope decreases, yet there is considerable

overlap at steeper slopes. Using these relationships, we can assign an approximate ECT_m to

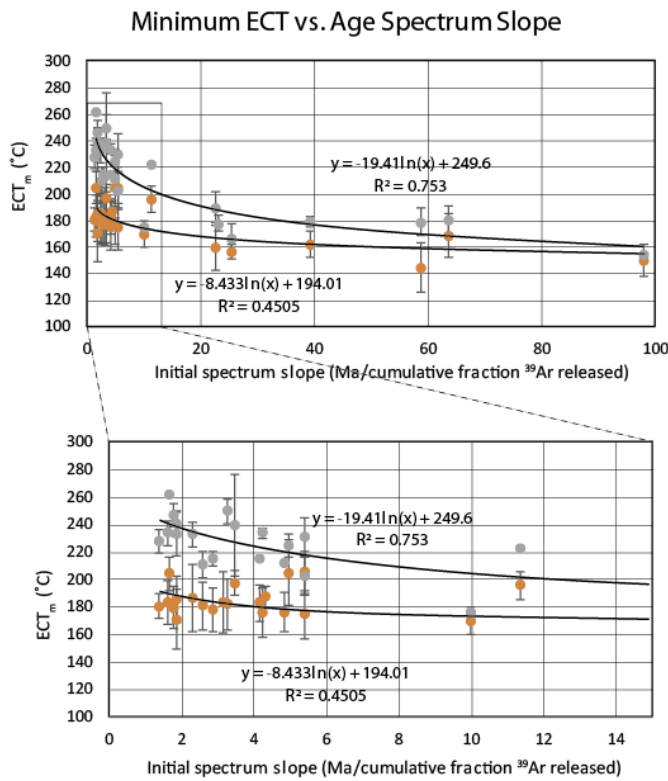any model or experimental age spectrum if we can measure the initial spectrum slope.

Figure 16: Plot showing the initial spectrum slope *(m_s)* and experimental and model ECT_m values. Grey data represent experimental ECT_m values and orange data represent model ECT_m values. Note that model ECT_m values are consistently cooler than experimental ECT_m values.

Model ECT_m values are distinctly cooler than their corresponding experimental ECT_m values,

with the largest ECT_m difference corresponding to samples with low initial spectrum slopes.

This difference is a reflection of the clear deviation between the minimum model spectrum

age and the minimum $^{40}Ar_{excess}$-corrected age – with the model spectrum consistently

stepping down to younger ages for the first few steps than we observe in the experimental spectrum. The consistently older ages from the linear $^{40}Ar_{excess}$ correction on the experimental spectrum yield temperatures from a point that is earlier, and thus hotter, on the modeled cooling curve but still compatible with the same cooling history. This age difference between the low-temperature steps of the model and $^{40}Ar_{excess}$- corrected experimental spectrum likely indicates that we are not fully correcting for $^{40}Ar_{excess}$ at low-temperature steps. In figure 17, we plot the calculated fractional percentage of $^{40}Ar_{excess}$ of the total argon released during the low-temperature steps (effectively, the increased area beneath the measured spectrum compared to the area beneath our linear $^{40}Ar_{excess}$ corrected projection of low-temperature ages) against the percent deviation between the $^{40}Ar_{excess}$-corrected minimum age and the MDD model minimum age (Fig. 17a), and the percentage of $^{40}Ar_{excess}$ at low-temperature steps against the difference between the experimental and model ECT_m (Fig. 17b). Both plots show a positive correlation, indicating that as the percentage of $^{40}Ar_{excess}$ at low-temperature steps increases, the $^{40}Ar_{excess}$-corrected ages and their associated ECT_m values increasingly deviate from their model equivalents. This suggests that the $^{40}Ar_{excess}$-corrected ages consistently overestimate the initial apparent age of a sample and that our MDD model minimum ages likely best represent the true minimum age that would be extracted from a given sample if no excess argon were present. However, with the goal of deriving T-t information directly from an experimental $^{40}Ar_{excess}$-corrected age spectrum (without undertaking MDD modeling), we will predominately use the experimental ECT_m curve shown in figure 16 to predict the ECT_m for a given age spectrum, yet recognize that this ECT_m value likely overestimates the true ECT_m for samples with significant excess argon in the low T steps.

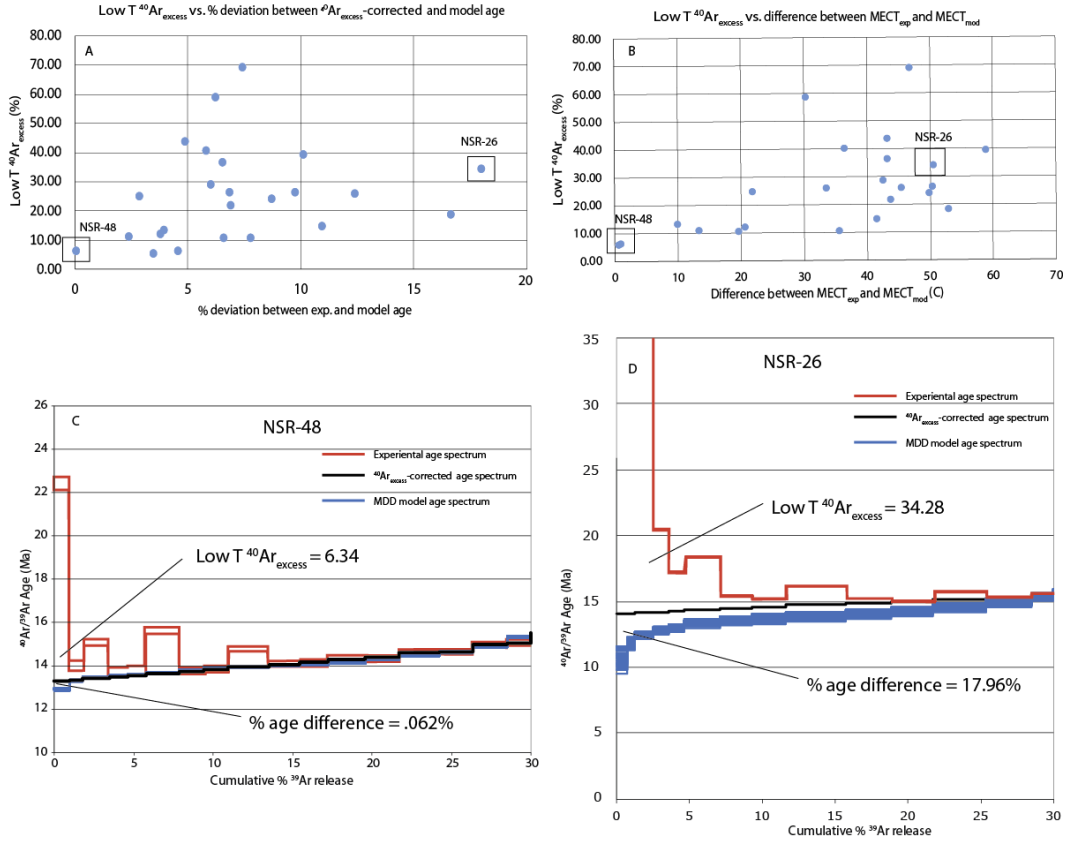Figure 17: The relationship between the amount of $^{40}Ar_{excess}$ measured at low temperature steps of a step heating experiment and the difference between the minimum experimental and minimum model ages (A) and experimental and model ECT_m values (B). Plots (C) and (D) show the experimental, $^{40}Ar_{excess}$-corrected and MDD model age spectrum for NSR-48 and NSR-26 respectively. NSR-48 exhibits a relatively small percentage of $^{40}Ar_{excess}$ across the first ~15% cumulative ^{39}Ar released and the minimum $^{40}Ar_{excess}$-corrected age and minimum MDD model age are similar. NSR-26 exhibits a much larger percentage of $^{40}Ar_{excess}$ across the first ~15-20% cumulative ^{39}Ar released and the minimum $^{40}Ar_{excess}$-corrected age and minimum MDD model age deviate considerably.

7.4. The relationship between the ECT and % cumulative Ar released: Derivation of a

Temperature Spectrum

Perhaps the most important relationship to be mined from our dataset is that between a sample's model ECT and the fraction of the cumulative ^{39}Ar released during a typical step-heating experiment. The first fraction of argon released corresponds to the minimum ECT obtainable from the sample (typically 160-220°C) and the final gas released (i.e., the last 1100°C step) represents that associated with the highest ECT (~325-375°C), but it would be

100

valuable to know how intermediate fractional stages of the argon released relate to specific intermediate ECTs and whether these relationships vary significantly among samples. If such a relationship could be demonstrated, it might be possible to construct a T-t curve directly from the age spectrum.

For each sample, we extracted the experimental ECT values for each incremental age of the step-heating experiment, and plotted these ECT values against the % cumulative ^{39}Ar released at that given age. We call the resultant plot a "temperature spectrum", analogous to an age spectrum, but illustrating instead how a sample's model ECTs, varies as a function of the fractional ^{39}Ar released. Figure 18a shows all the temperature spectra from all the individual samples that we modeled. Temperature spectra generally show that ECT values monotonically increase as a function of fractional ^{39}Ar released, although the relationship is sample dependent (Fig. 18a). Figure 18b shows the mean temperature spectrum, with each datum representing the mean and 2nd standard deviation ECT of the entire dataset at the corresponding percentage of cumulative ^{39}Ar released (i.e., 10%, 20%, etc.). The mean temperature spectrum forms a slightly convex-up curve from an average ECT$_m$ of 223 ± 52°C to an average ECT of 317 ±37°C at the 1100°C temperature step. This mean temperature spectrum essentially serves as a "cheat sheet" for constructing an approximate T-t path for a K-feldspar ^{40}Ar/^{39}Ar age spectrum. For any given cumulative percent ^{39}Ar released, we can assign a geologic cooling temperature (albeit with a large uncertainty) to the ^{40}Ar/^{39}Ar spectrum age at that given cumulative percent ^{39}Ar released (Figure 18c). By plotting the spectrum ages at 0%, 10%, 20%, etc. against the mean ECT at that cumulative percent ^{39}Ar released, we can construct an approximate T-t history for that age spectrum (Figure 18d).
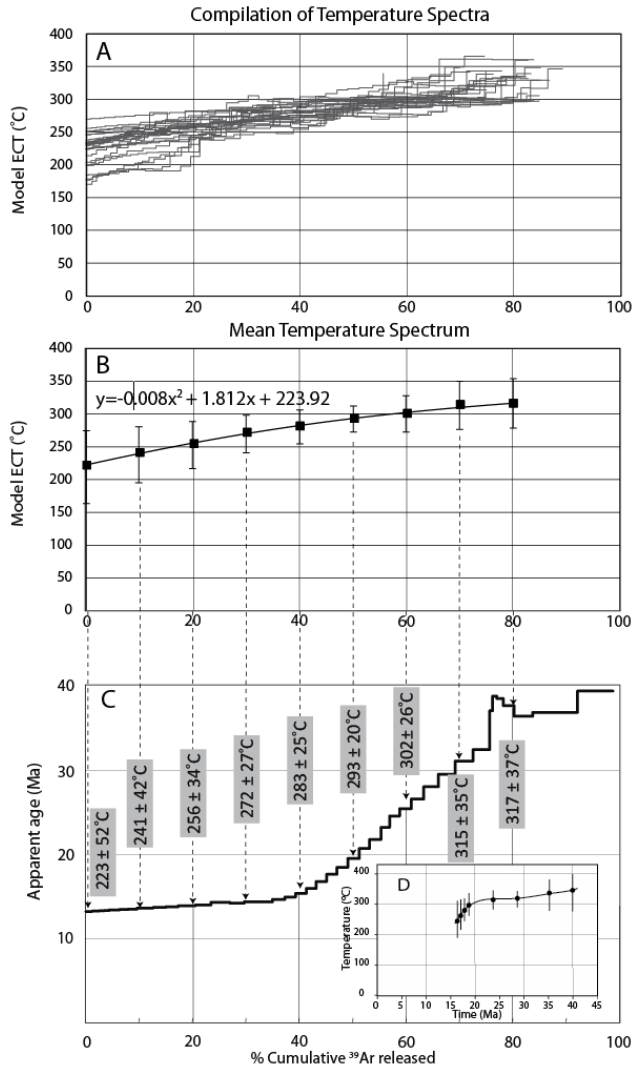
Figure 18: The temperature spectrum and how it can be used to construct T-t histories. (A) Compilation of temperature spectra for the entire dataset derived from $^{40}Ar_{excess}$-corrected age spectra. (B) The mean temperature spectrum for the dataset. Error bars are 2σ. C) Example age spectrum illustrating how the ECT values from the mean temperature spectrum can be assigned to specific spectrum ages. D) An approximate T-t path combining ECTs from the mean temperature spectrum (B) and ages from the age spectrum (C).

While figure 18a illustrates the temperature spectra for the entire dataset, and Figure 18b nicely summarizes the average temperature spectrum for all samples, the temperature spectra for our dataset take three different forms (Fig. 19). Furthermore, these forms appear to relate to the general nature of the sample's cooling history. Samples with Form 1 temperature spectra show the smallest range of ECTs obtainable from the samples ranging from ~225-330°C, and have a constant shallow slope across the range of cumulative percent ^{39}Ar released. Samples with Form 2 temperature spectra have a larger closure temperature window than Form 1 samples, spanning from 180 to 340°C, and have a steep ECT gradient

102

over the first ~30% cumulative ^{39}Ar released and then shallows and broadly matches Form 1 temperature spectra across the higher fractions of ^{39}Ar released. Samples with Form 3 temperature spectra span the broadest range of ECTs from ~190 to 360°C and have a uniform, relatively steep gradient across the entire range of cumulative ^{39}Ar released.

If we can predict the form of a sample's temperature spectrum based on either its experimental age spectrum and/or its model parameters, we can construct a more precise cooling history for that sample from the appropriate temperature spectrum "form." One possibility is that these different temperature spectra shapes are controlled primarily by the domain size distribution (discussed in part 1). It is conceivable that a sample with a large volume fraction of ^{39}Ar retained within small domains (each with a relatively low closure temperature) may exhibit a temperature spectrum with lower ECT values across a large portion of the ^{39}Ar released, compared to a sample with a large volume fraction of ^{39}Ar retained within large domains with higher closure temperatures. However, we find that the various types of domain size distribution (i.e., Type I, II, III) show no correlation with the various temperature spectra shapes, just as the domain distributions showed little correlation with the shapes of age spectra (Fig. 9).

Instead, we find that the shape of a sample's temperature spectrum correlates closely with the general shape of a sample's age spectrum (Figure 19), and consequently is strongly correlated with overall cooling history. Form 1 temperature spectra correspond to samples with low initial spectrum slopes followed by high spectrum slopes until the last 1100°C step, indicative of slow cooling through the high-temperature portion of the closure window followed by rapid cooling through the low-temperature portion of the closure window. Form 2 temperature spectra correspond to samples with high spectrum slopes across the entire

range of cumulative percent [39]Ar released, indicative of continuous slow cooling through the entire closure window. Form 3 temperature spectra correspond to samples with high initial spectrum slopes and low spectrum slopes at higher cumulative percentages of [39]Ar released, indicative of rapid cooling through the high-temperature portion of the closure window followed by slow cooling through the lower temperature portion.

The relationship between the cooling path and the various temperature spectra forms is consistent with Dodson's closure theory (Equation 3). For samples that cooled slowly, Dodson's equation predicts lower Tmin and Tmax closure temperatures. We acknowledge that the samples in our data set illustrate only a limited number of possible age spectrum shapes and T-t paths.

With this link between the general shape of an age spectrum and the form of the temperature spectrum, we can now choose the appropriate temperature spectrum form to construct more precise cooling histories directly from the experimental age spectrum.
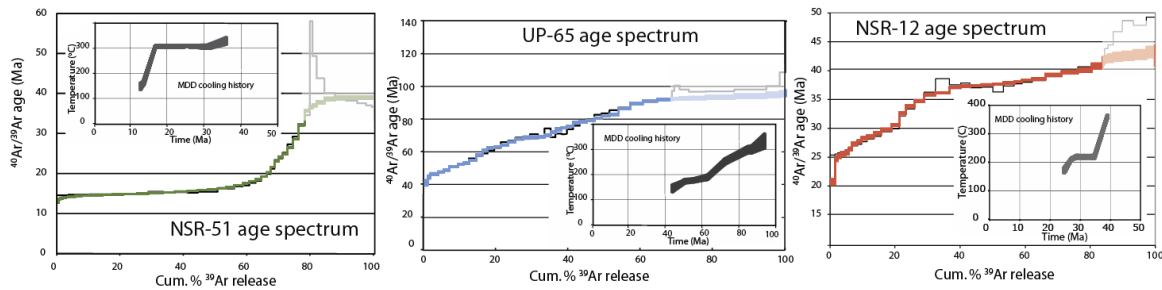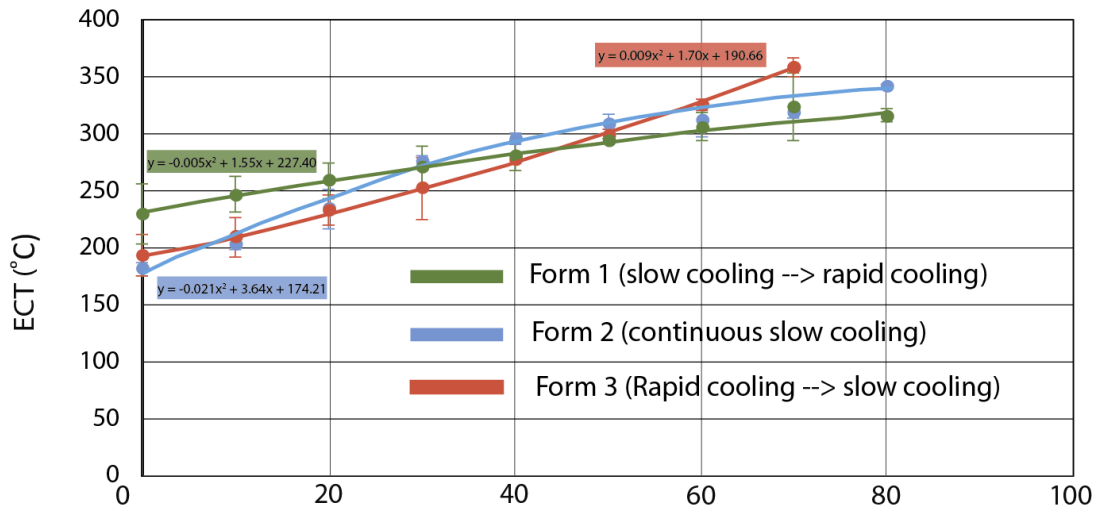
Figure 19: The various Forms (1, 2, and 3) of the temperature spectrum and their associated age spectrum shapes and T-t paths. The various temperature spectra curves were obtained by averaging samples ($\pm 2^{nd}$ S.D.) that displayed the various temperature spectra forms – 22 samples for Form 1, 4 samples for Form 2, and 2 samples for Form 3. The Form 1 temperature spectrum (green) correspond to samples that underwent slow cooling followed by rapid cooling. Form 2 temperature spectrum (blue) corresponds to samples that underwent continuous slow cooling, and the Form 3 temperature spectrum (red) correspond to samples that underwent rapid cooling followed by slow cooling (discussed in text).

7.5. A schema for extracting cooling histories directly from a $^{40}Ar/^{39}Ar$ K-feldspar age spectrum

Armed with the relationships between 1) spectrum slope and geologic cooling rate (Fig. 15), 2) the initial spectrum slope and the ECT_m (Fig. 16), and 3) the ECT and the cumulative percentage of ^{39}Ar released – i.e., the temperature spectrum (Figure 19), we have ample information to construct a cooling history directly from an experimental age spectrum that should closely mimic that obtained by MDD modeling. Here, we present a 4-step schema for

doing that, and use this schema to construct cooling histories for two samples, UP-43 and UP-54, which we compare to their independently-derived MDD cooling histories (Fig. 20).

Step 1: *Inspect the general shape of the age spectrum and select the appropriate temperature spectrum shape*

For a given $^{40}Ar_{excess}$-corrected age spectrum, identify regions with low and/or high spectrum slopes, and select the most appropriate temperature spectrum "form" that fits the shape of the age spectrum (Form 1, 2, or 3; Fig. 19). In Figure 20, sample UP-43 has an age spectrum with a low- to moderate initial slope followed by a sharp upward inflection until the last 1100°C step that most closely resembles those that produce a Form 1 temperature spectrum. UP-54 has an age spectrum with high spectrum slopes for the first ~40% cumulative Ar released, followed by a concave-down inflection and a low spectrum slope for final ~25% cumulative Ar released before the final 1100°C step – an age spectrum shape that most closely resembles those that produce a Form 3 temperature spectra.

Step 2: Create an approximate cooling history using the appropriate temperature spectrum template

Use the selected temperature spectrum from *step 1* to assign ECT values to the spectrum ages at various percentages of ^{39}Ar released, and plot the results in temperature-time space, creating a "first pass" cooling history (as shown in Fig. 18). ECT values for any cumulative fraction ^{39}Ar released can be extracted from the temperature spectrum by using the appropriate polynomial functions from Fig. 19. In Figure 19, purple cooling histories for UP-43 and UP-54 are derived directly from the

temperature spectrum template assigned in step 1. For many research needs, this "first pass" cooling history may meet the demands of the geologic problem and no further effort may be required.

Step 3: Revise the ECT$_m$ of the temperature spectrum-derived cooling history

Use the initial spectrum slope (m_s) to revise the ECT$_m$ of the youngest spectrum age (Fig. 16). For example, the purple cooling history for UP-43 has a "first pass" ECT$_m$ of ~225°C. However, using figure 16, we see that the ECT$_m$ corresponding to an initial spectrum slope of ~21 Ma/cumulative fraction ^{39}Ar released is ~190°C, significantly colder than the approximate ECT$_m$ derived from the temperature spectrum.

Step 4: *Refine the cooling history by assigning cooling rates to various age spectrum slopes.*

Measure the slopes of various linear segments of the experimental age spectrum and note the ages of inflection points between these segments. Using Figure 15, assign geologic cooling rates to linear segments of the age spectrum, and use these cooling rates to adjust the approximate cooling history from *step 2 and 3*. To illustrate this, we measure three different spectrum slopes over the first ~60% ^{39}Ar released of sample UP-43, labeled (2), (4), and (6), and note the ages of the inflection points between these slope intervals, labeled (3) and (5) (Fig 19a). Using Figure 15, we determine the cooling rates associated with these spectrum slopes – ~14°C/Ma between 28.6 and 33 Ma (2), ~2.5°C/Ma between 33 and 49 Ma (4), and ~24°C/Ma between 39 and 42 Ma (6), and then use these cooling rates to construct a more

detailed cooling history shown by the black cooling curve in Figure 20a. This cooling

rate-corrected T-t path exhibits a distinct "step" between ~33 and 42 Ma, highlighted

by rapid cooling between 42 and 39 Ma, followed by slow cooling between 39 and 33

Ma, then returning to rapid cooling a (~14°C/Ma) from 33 to 29 Ma.

The cooling histories for UP-54 and UP-43 created using steps 1-4 above closely match their

respective MDD model cooling histories (Fig. 20). The temperature spectrum-derived "first

pass" cooling histories (shown in purple) created via *step 2* mimic the general shape of the

MDD cooling history, but do not capture the smaller inflections in the MDD cooling history.

However, after revising the ECT_m (*step 3*) and assigning specific cooling rates to certain

intervals of the cooling history (*step 4*), our T-t paths more closely match the MDD cooling

histories. The major deviations between the cooling histories derived from the age spectra

and the MDD cooling histories are where the model age spectrum deviates from the

experimental age spectrum, suggesting that the MDD cooling history may not accurately

capture the "true" cooling history for that portion of the experimental age spectrum.

Figure 20 shows that the spectrum-derived T-t method and MDD modeling T-t method yield

similar, but not identical, cooling histories. Because the cooling histories are not identical, we

ask: which technique yields the most geologically reasonable cooling histories? We test this

by applying both methods to six samples from a NW-SE transect in the eastern footwall of
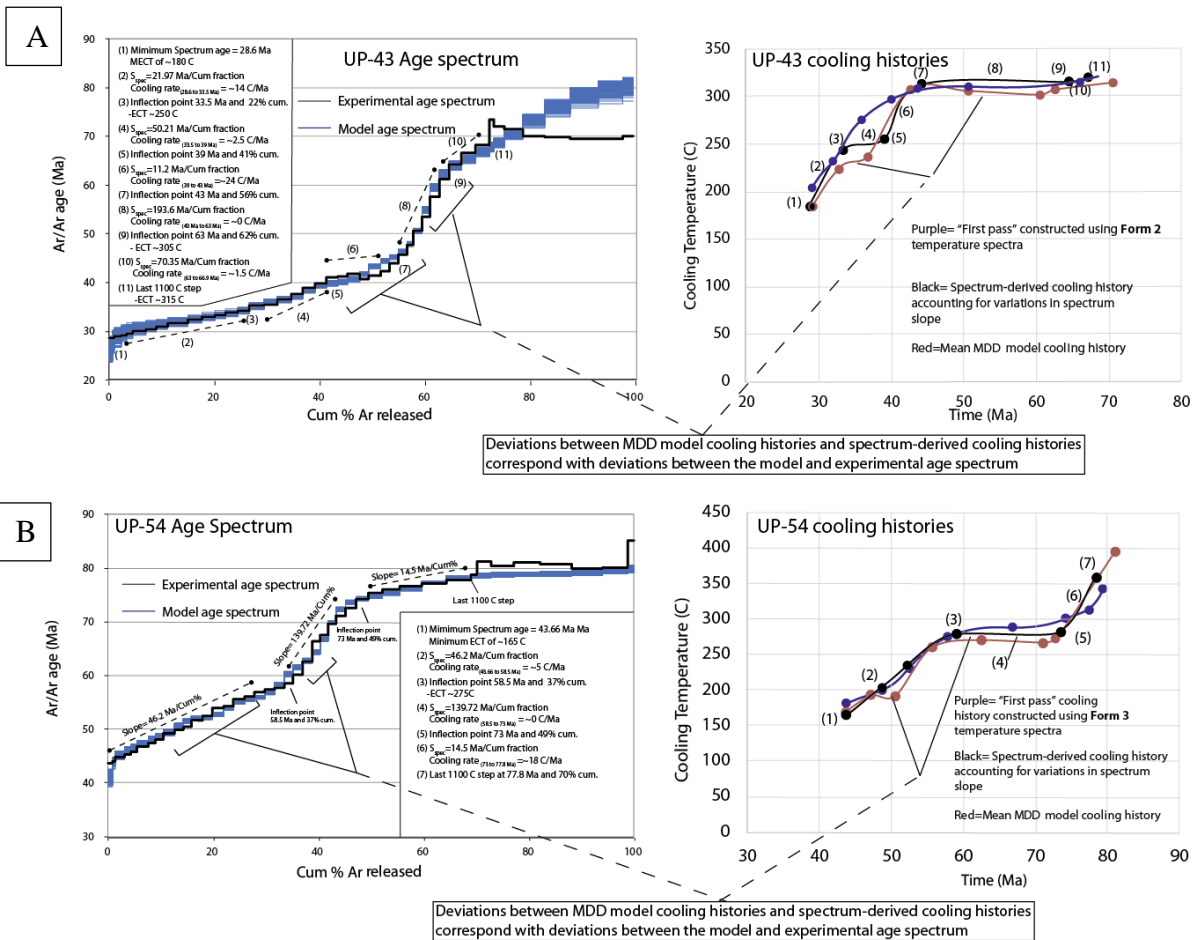
the NSR (Fig. 21).

Figure 20: Cooling histories for samples UP-43 and UP-54 derived directly from the age spectrum (purple and black) and their corresponding MDD model cooling histories (red). Purple cooling histories are created from the appropriate temperature spectra (Form 2 for UP-43 and Form 3 for UP-54). Black cooling histories are modifications to the "first pass" purple cooling curves that account for variations in spectrum slope (i.e. cooling rate). The black numbers adjacent to the black curves correspond to specific spectrum slope and ages shown on the accompanying age spectrum. MDD model cooling histories are shown in red. Note that deviations between the MDD model and spectrum-derived cooling histories generally occur where the MDD model age spectrum deviates from the experimental age spectrum.

All samples within this transect are from the same stratigraphic horizon of Cpm. If the NSR footwall was exhumed by top-east slip along the NSRD (Fig. 21b), $^{40}Ar/^{39}Ar$ ages and their corresponding T-t paths should systematically young to the east. As expected, we observe that $^{40}Ar_{excess}$-corrected ages and spectrum-derived T-t paths young to the east (Fig. 21c,d). However, MDD model T-t paths for this transect do not show a consistent eastward younging trend (Fig. 21e), likely due to poor MDD model fit in portions of the experimental age

109

spectrum with abundant $^{40}Ar_{excess}$. The clear eastward younging trend in spectrum-derived T-t paths compared to the scatter in MDD model T-t paths suggests that perhaps the spectrum-derived T-t method yields more geologically reasonable cooling histories.
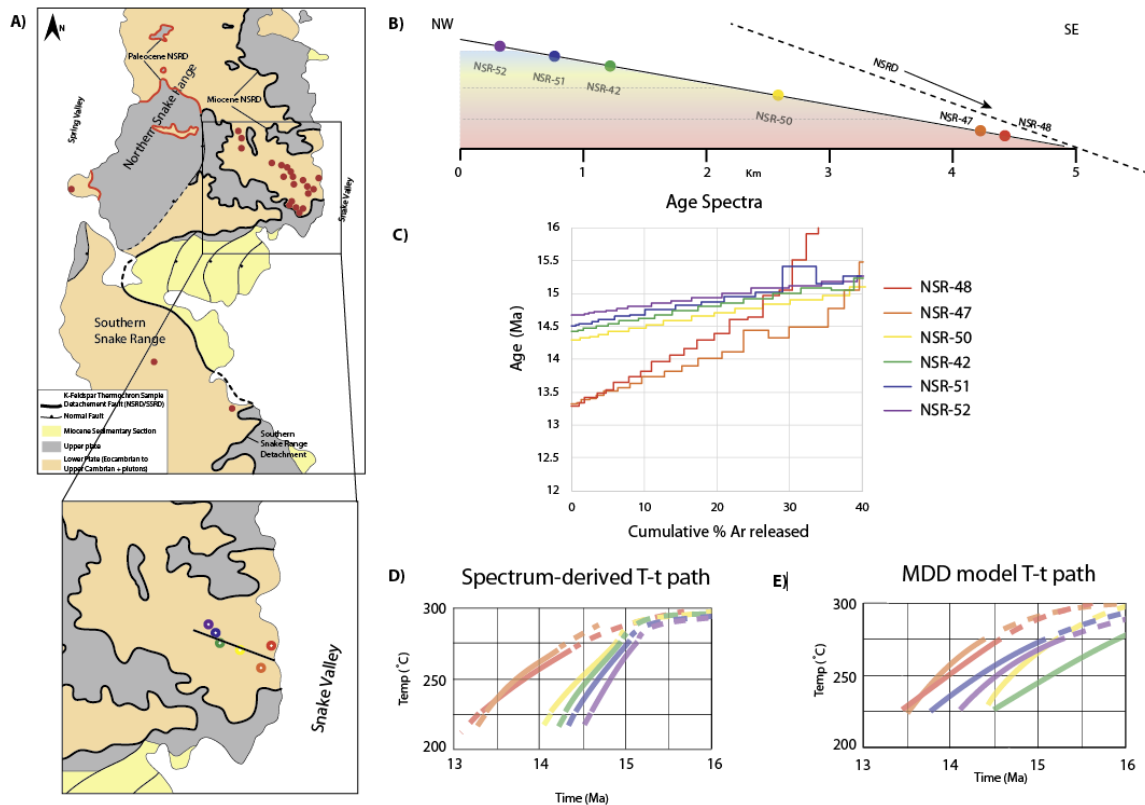

Figure 21: Comparison of spectrum-derived and MDD model T-t paths from a NW-SE transect at the NSR footwall. A) Simplified map and inset showing the location of the 6 samples along the NW-SE transect. B) Schematic cross section of the NW-SE transect showing top-east slip along the NSRD. The color gradient in the NSRD footwall illustrates a horizontal geothermal gradient. C) $^{40}Ar_{excess}$-corrected age spectra for samples in NW-SE transect. $^{40}Ar/^{39}Ar$ ages systematically decrease to the east, consistent with cooling in the footwall of a top-east normal fault. D) Spectrum-derived T-t paths showing that cooling histories systematically young to the east. E) MDD model T-t paths for samples of the NW-SE transect. The MDD model T-t paths fail to show the eastward younging cooling trend observed in the experimental age spectra (C) and the spectrum-derived T-t paths (D).

Discussion of the spectrum-derived T-t method:

This study is the first to our knowledge to quantify the relationships between the attributes of a K-feldspar incremental heating $^{40}Ar/^{39}Ar$ age spectrum (e.g., age ranges, slopes, intercepts, inflections, cumulative fraction released) and the MDD cooling history of the sample (temperatures and cooling rates), and use these relationships to develop an alternative, and potentially more reliable, method to determine a sample's T-t path. We recognize the samples used to develop this methodology are somewhat restricted—all are from a similar rock type (detrital K-feldspar grains that underwent metamorphism at >350°C), and were processed and analyzed in the same way. They experienced a limited range of cooling histories: a) slow-cooling followed by rapid cooling, b) rapid cooling followed by slow cooling, or c) continuous slow cooling within the K-feldspar closure window. We do not know how well the method can be used with other rock types, $^{40}Ar/^{39}Ar$ K-feldspar spectra or cooling histories.

It is also unclear how the analytical procedure of a step-heating experiment may change the shape of an age spectrum. For this study, we conducted consistent and detailed step-heating experiments for each sample with multiple replicate steps to produce high-resolution age spectra in which 65-85% of the Ar was released before incongruent melting above 1100°C. Other analytical procedures will produce different age spectra with different slopes and inflection paints that may lead to differences in the estimated cooling histories using our schema. Nevertheless, the methodology proposed here may be broadly applicable to K-feldspar age spectra and provides a novel way to quickly extract a cooling history from a K-feldspar age spectrum.

An important and obvious application of this methodology is that it provides the tools for extracting semi-quantitative T-t histories from previously published ^{40}Ar/^{39}Ar K-feldspar data. There are many published K-feldspar age spectra without accompanying T-t histories, as they were never modeled and may not have been analyzed in a way that was appropriate for MDD modeling. We can now assign approximate T-t histories to such published spectra and use these T-t histories to draw new thermal and/or tectonic interpretations. Additionally, the spectrum-derived T-t method is significantly faster than computing MDD cooling histories and is therefore desirable for studies that wish to compile and compare a large dataset of geologic cooling histories. Moreover, MDD modeling has a relatively steep learning curve that may discourage use of the method. The spectrum-derived T-t method provides a straightforward, semi-quantitative means of extracting a large dataset of cooling histories in a fraction of the time.

A preliminary comparison of spectrum-derived and MDD model T-t paths from a NW-SE transect of the NSR footwall shows that spectrum-derived T-t paths are more consistent with cooling in the footwall of a major top-east normal fault (Fig. 21d,e). This result suggests that perhaps spectrum-derived T-t paths are more robust than MDD model T-t paths, and thus can lead to better interpretations of regional cooling and/or uplift. One potential reason the spectrum-derived T-t paths are more geologically reasonable than the MDD T-t paths along this transect is that the spectrum-derived method essentially "averages out" error due to poor MDD model fit across our entire dataset, thus minimizing erroneous cooling histories. Future work will test this hypothesis by comparing spectrum-derived and MDD model T-t paths for other geologically well-constrained transects at the NSR.

8. CONCLUSIONS (COMBINED PART I AND II)

Multiple-diffusion domain (MDD) modeling of a large (n=28) geologically well-constrained K-feldspar $^{40}Ar/^{39}Ar$ thermochronology dataset from the Northern Snake Range, NV and surrounding environs provide new insights into MDD parameter space and the consistency of MDD cooling histories. We determine that domain size distributions (i.e. size and volume fraction of total Ar) vary considerably throughout the dataset. Domain sizes span 4-5 orders of magnitude within a single sample from $\rho \sim 0.02$ to $\rho \sim 200$ and the distribution of Ar among domains is dependent on grain-size – with fine grain K-feldspars (<300µm) holding ~45% of Ar within small domains (ρ<2) and coarser grained samples (>500 µm) holding ~20% of Ar within small domains. All samples require ≥8 diffusion domains to adequately model the diffusion results from the step-heating experiment – any fewer domains will yield erroneous cooling histories. The activation energy (E_a) of Ar diffusion from K-feldspar samples range from 42 to 54 kcal/mol with a mean (±σ) of 48.4 ± 1.6 kcal/mol. We find that large deviations from the mean E_a are likely due to analytical error and/or ambiguities in calculating E_a from diffusion results. To increase the internal consistency of MDD cooling histories within a given dataset, we recommend that all MDD models use the average E_a value of the dataset when calculating cooling histories.

Using these best-practices, we create an internally consistent dataset of MDD cooling histories at the northern Snake Range and environs and use this dataset to quantify the relationships between the attributes of a K-feldspar incremental heating $^{40}Ar/^{39}Ar$ age spectrum (e.g., age ranges, slopes, intercepts, inflections, cumulative fraction released) and the MDD cooling history of the sample (temperatures and cooling rates). There are

correlations between a) the slope of an age spectrum and the MDD cooling rate over the ages of that spectrum slope interval, b) the initial slope of an age spectrum (between ~0-20% ^{39}Ar released) and the minimum cooling temperature recorded by that sample, and c) the cumulative percentage of ^{39}Ar released and the effective cooling temperature of a sample. These relationships between the age spectrum and MDD derived cooling history are sufficiently systematic and quantifiable that we develop a schema for extracting T-t histories directly from K-Feldspar age spectra, bypassing the laborious MDD modeling process. This method, named the spectrum-derived T-t method, produces T-t histories that are similar to those produced by MDD modeling for the dataset presented herein, and may, in fact, yield more geologically meaningful cooling trends across the entire dataset. Results and techniques from this study will be applied to a forthcoming companion paper exploring the thermal architecture, geometric evolution, and exhumation and cooling history of the Snake Range and environs.

9. REFERENCES:

Batt, G. E., Baldwin, S. L., Cottam, M. A., Fitzgerald, P. G., Brandon, M. T., & Spell, T. L. (2004). Cenozoic plate boundary evolution in the South Island of New Zealand: New thermochronological constraints. *Tectonics*, *23*(4).

Benowitz, J. A., Layer, P. W., & Vanlaningham, S. (2014). Persistent long-term (c. 24 Ma) exhumation in the Eastern Alaska Range constrained by stacked thermochronology. *Geological Society, London, Special Publications*, *378*(1), 225-243.

Burgess, R., Kelley, S. P., Parsons, I., Walker, F. D. L., & Worden, R. H. (1992). ^{40}Ar/^{39}Ar analysis of perthite microtextures and fluid inclusions in alkali feldspars from the Klokken syenite, South Greenland. *Earth and Planetary Science Letters*, *109*(1-2), 147-167.

Cassata, W. S., & Renne, P. R. (2013). Systematic variations of argon diffusion in feldspars and implications for thermochronometry. *Geochimica et Cosmochimica Acta*, *112*, 251-287.

Dodson, M. H. (1973). Closure temperature in cooling geochronological and petrological systems. *Contributions to Mineralogy and Petrology*, *40*(3), 259-274.

Harrison, T. M. (1983). Some observations on the interpretation of 40Ar/39Ar age spectra. *Chemical geology*, *41*, 319-338.

Harrison, T. M., & Bé, K. (1983). 40Ar/39Ar age spectrum analysis of detrital microclines from the southern San Joaquin Basin, California: an approach to determining the thermal evolution of sedimentary basins. *Earth and Planetary Science Letters*, *64*(2), 244-256.

Harrison, T. M., Morgan, P., & Blackwell, D. D. (1986). Constraints on the age of heating at the Fenton Hill site, Valles Caldera, New Mexico. *Journal of Geophysical Research: Solid Earth*, *91*(B2), 1899-1908.

Harrison, M.T., Grove, M,. Lovera,O.M. Zeitler, P.K. (2005). Continuous thermal histories from closure profiles. Reviews in Mineralogy & Geochemistry. 58, 389-409.

Harrison, T. M., & Lovera, O. M. (2014). The multi-diffusion domain model: past, present and future. *Geological Society, London, Special Publications*, *378*(1), 91-106.

Harrison, T. M., Lovera, O. M., & Heizler, M. T. (1991). $^{40}Ar/^{39}Ar$ results for alkali feldspars containing diffusion domains with differring activation evergy. *Geochimica et Cosmochimica Acta*, *55*(5), 1435-1448.

Heizler, M. T., & Harrison, T. M. (1988). Multiple trapped argon isotope components revealed by 40Ar39Ar isochron analysis. *Geochimica et Cosmochimica Acta*, *52*(5), 1295-1303.

Lee, J. (1995). Rapid uplift and rotation of mylonitic rocks from beneath a detachment fault: Insights from potassium feldspar 40Ar/39Ar thermochronology, northern Snake Range, Nevada. *Tectonics*, *14*(1), 54-77.

Lovera, O. M., Heizler, M. T., & Harrison, T. M. (1993). Argon diffusion domains in K-feldspar II: Kinetic properties of MH-10. *Contributions to Mineralogy and Petrology*, *113*(3), 381-393.

Lovera, O. M., Richter, F. M., & Harrison, T. M. (1989). The 40Ar/39Ar thermochronometry for slowly cooled samples having a distribution of diffusion domain sizes. *Journal of Geophysical Research: Solid Earth*, *94*(B12), 17917-17935.

Lovera, O. M., Richter, F. M., & Harrison, T. M. (1991). Diffusion domains determined by 39Ar released during step heating. *Journal of Geophysical Research: Solid Earth*, *96*(B2), 2057-2069.

McDannell, K. T., Schneider, D. A., Zeitler, P. K., O'Sullivan, P. B., & Issler, D. R. (2019). Reconstructing deep-time histories from integrated thermochronology: An example from southern Baffin Island, Canada. *Terra Nova*, *31*(3), 189-204.

McDougall, I. & Harrison, T. M. (1983). *Geochronology and Thermochronology by the 40Ar/39Ar Method*. Oxford University Press.

Parsons, I., Brown, W. L., & Smith, J. V. (1999). 40 Ar/39 Ar thermochronology using alkali feldspars: real thermal history or mathematical mirage of microtexture?. *Contributions to Mineralogy and Petrology*, *136*(1-2), 92-110. Villa, 2014

Parsons, I., Rex, D. C., Guise, P., & Halliday, A. N. (1988). Argon-loss by alkali feldspars. *Geochimica et Cosmochimica Acta*, *52*(5), 1097-1112.

Reddy, S. M., Potts, G. J., & Kelley, S. P. (2001). 40 Ar/39 Ar ages in deformed potassium feldspar: evidence of microstructural control on Ar isotope systematics. *Contributions to Mineralogy and Petrology*, *141*(2), 186-200.

Richter, F. M., Lovera, O. M., Harrison, T. M., & Copeland, P. (1991). Tibetan tectonics from 40Ar/39Ar analysis of a single K-feldspar sample. *Earth and Planetary Science Letters*, *105*(1-3), 266-278.

Villa, I. M. (2014). Diffusion of Ar in K-feldspar: Present and absent. *Geological Society, London, Special Publications*, *378*(1), 107-116.

Lovera, O. M., Grove, M., Harrison, T. M., & Mahon, K. I. (1997). Systematic analysis of K-feldspar 40Ar39Ar step heating results: I. Significance of activation energy determinations. *Geochimica et Cosmochimica Acta*, *61*(15), 3171-3192.

Zeitler, P. K. (1987). Argon diffusion in partially outgassed alkali feldspars: insights from ^{40}Ar/^{39}Ar analysis. *Chemical Geology: Isotope Geoscience section*, *65*(2), 167-181.

Zeitler, PK (2004). Arvert 4.0.01. Inversion of ^{40}Ar/^{39}Ar age spectra. User's Manual (http://www/ees/lehigh.edu/EESdocs/geochron/downloads/arvert401guide-US.pdf).